RADIATIVE EFFECTS OF DUST AEROSOLS, NATURAL CIRRUS CLOUDS

AND CONTRAILS: BROADBAND OPTICAL PROPERTIES AND

SENSITIVITY STUDIES

A Dissertation

by

BINGQI YI

Submitted to the Office of Graduate Studies of
Texas A&M University
in partial fulfillment of the requirements for the degree of

DOCTOR OF PHILOSOPHY

Chair of Committee,	Ping Yang
Co-Chair of Committee,	Kenneth P. Bowman
Committee Members,	Gerald R. North
	Faming Liang
Head of Department,	Ping Yang

August 2013

Major Subject: Atmospheric Sciences

ABSTRACT

This dissertation aims to study the broadband optical properties and radiative effects of dust aerosols and ice clouds. It covers three main topics: the uncertainty of dust optical properties and radiative effects from the dust particle shape and refractive index, the influence of ice particle surface roughening on the global cloud radiative effect, and the simulations of the global contrail radiative forcing.

In the first part of this dissertation, the effects of dust non-spherical shape on radiative transfer simulations are investigated. We utilize a spectral database of the single-scattering properties of tri-axial ellipsoidal dust-like aerosols and determined a suitable dust shape model. The radiance and flux differences between the spherical and ellipsoidal models are quantified, and the non-spherical effect on the net flux and heating rate is obtained over the solar spectrum. The results indicate the particle shape effect is related to the dust optical depth and surface albedo. Under certain conditions, the dust particle shape effect contributes to 30% of the net flux at the top of the atmosphere.

The second part discusses how the ice surface roughening can exert influence on the global cloud radiative effect. A new broadband parameterization for ice cloud bulk scattering properties is developed using severely roughened ice particles. The effect of ice particle surface roughness is derived through simulations with the Fu-Liou and RRTMG radiative transfer codes and the Community Atmospheric Model. The global averaged net cloud radiative effect due to surface roughness is around 1.46 Wm^{-2}. Non-negligible increase in longwave cloud radiative effect is also found.

The third part is about the simulation of global contrail radiative forcing and its sensitivity studies using both offline and online modeling frameworks. Global contrail distributions from the literature and Contrail Cirrus Prediction Tool are used. The 2006 global annual averaged contrail net radiative forcing from the offline model is estimated to be 11.3 mW m^{-2}, with the regional contrail radiative forcing being more than ten times stronger. Sensitivity tests show that contrail effective size, contrail layer height, the model cloud overlap assumption, and contrail optical properties are among the most important factors.

DEDICATION

To my parents, Ronghui Yi and Jingui Li

ACKNOWLEDGEMENTS

Last but not the least, thanks to my parents and family for their persistent love, support and encouragement. I couldn't have finished my degree without them, to whom this dissertation is dedicated.

TABLE OF CONTENTS

LIST OF FIGURES

LIST OF TABLES

CHAPTER I

INTRODUCTION

1.1 Aerosols and clouds and their impacts on climate

Aerosols and clouds are important components in the earth's atmosphere. They not only exert significant influence on the climate individually (i.e. their direct radiative effects), but also modulate the energy balance of the earth by complicated aerosol-cloud interactions (i.e. the indirect radiative effects of aerosols). Clouds also have important feedbacks on climate and climate change. In the last few decades, thousands and thousands of research activities, ranging from observational perspectives (i.e. ground-base and air-borne instruments) to numerical modeling (i.e. regional and global simulations), have been implemented to study the physical nature of aerosols and clouds and their related processes.

Among all the important physical processes, the radiative effects of aerosols and clouds are the focal points of interests. More specifically, the single-scattering properties of dust aerosols and ice clouds that determine the scattering and absorption of shortwave and longwave radiation are the main subjects of this study. Although estimates of direct radiative effects of dust aerosols and ice clouds are determined and quantified (Forster et al. 2007), significant uncertainties still remain because there are factors that have long been ignored or simplified. These errors can be carried over to the parameterization schemes used in numerical models and produce unpredictable results. The hidden uncertainties will be uncovered by way of detailed analysis and sensitivity studies.

1.2 Current understandings of optical properties

The intrinsic factors that can influence the optical properties of aerosols and clouds include: chemical composition, particle size, particle shape and particle surface features. Chemical composition determines the refractive indices of the particles, and thus affects the optical properties of them. Different sources of origin of aerosols may have different compositions and show different optical properties. For example, Saharan dust and Asian dust shows diverse absorbing characteristics (Sokolik et al. 2001). In addition, aerosol composition may further be changed during their transportation processes, i.e. dust aerosols transported through heavily polluted areas are found to be coated with sulfate or soot which dramatically change their physical properties. Liquid clouds and ice clouds may also change their optical properties, such as contrails can be contaminated by soot emission from aircraft exhaust; convective clouds can be contaminated by industrial pollution.

Although dust aerosols and ice clouds are very different in their chemical compositions, they have one thing in common that they have complex particle morphologies. Ice cloud particles have relatively well-defined shapes, which include droxtals, hexagonal columns, plates, bullet rosettes, etc, while the shapes of dust particles are diverse which could be further changing with time, space and under different conditions. The particle shape effects are known to be crucial for the satellite retrieval of aerosol and cloud properties (i.e. Feng et al. 2009), but still are poorly quantified in modeling work.

What's more, observations, however, further show that the regularly-shaped ice crystals tend to have roughened particle surface features which could be ubiquitous within ice clouds (Ulanowski et al. 2006; 2012). Both the shape and surface roughness effects pose significant uncertainties to the determination of dust and ice particle optical properties and thus the estimation of their radiative effects. However, the corresponding quantifications of these uncertain factors are again lacking.

1.3 Present status of optical property parameterization schemes

In radiative transfer models and general circulation models, parameterization schemes are used to derive the aerosol and cloud optical properties in order to simplify the calculation and to save computational time. Parameterization is defined as the representation of the complicated physical processes with simplified parameters instead of resolving every detail. Using parameterizations has several advantages, and sometimes is a must, but it also induces uncertainties because of the assumptions and simplifications made within the development of parameterization schemes. Specifically for the parameterizations of optical properties of dust aerosols and ice clouds, they have various issues respectively.

1.3.1 Dust aerosol optical properties within broadband models

Among all the factors (the composition, particle morphology, number concentration, particle size distribution, and spatial and temporal distributions of dust aerosols) that could influence the scattering properties of dust aerosols, the aerosol

particle shape receives the least attention. Although in situ and laboratory measurements have long proven that most if not all dust aerosols are non-spherical in shape, the majority of up-to-date numerical models still use a dust aerosol optical property parameterization scheme that is based on spherical particle model assumption. One major reason is that there is no such suitable non-spherical particle model to replace the spherical one. There exist real difficulties in constructing a set of universal dust optical property database for applications in the whole global area in general circulation models, including the lack of available observations and measurements and the limitation of theoretical and physical methods to deal with light-scattering problems of non-spherical particles in various sizes and shapes.

A second reason is that people are not fully aware of whether dust particle shapes exert significant influence on the dust optical properties and radiative effect and how large exactly the non-spherical effect is. Controversial results from different groups of researchers further complicate this problem. Despite some results (Mishchenko et al. 1997; West et al. 1997) show apparent differences in the phase matrix between spherical and non-spherical dust models, several results (Mishchenko et al. 1995; Fu et al. 2009) display small effects of these differences in optical properties on the simulation of radiative flux. Thus, spherical particle approximation is regarded as a suitable and adequate substitute to be used in broadband radiative transfer models. However, some other progress (Kahnert et al. 2005; 2007) reports that the non-spherical effect of dust aerosols can be comparable to the effect of refractive index. What's more, using

spherical particle model may potentially induce unpredictable errors as pointed out by Mishchenko et al. (2003).

By the time of this study, there have been ample advances in theory and measurement that allow for a more systematic and comprehensive analysis and the quantification of the effect of various factors that influence dust optical properties and radiative effects. It would be beneficial to revisit the non-spherical dust particle model and the corresponding optical properties with the new advances incorporated.

1.3.2 Natural cirrus cloud optical property parameterizations

Various kinds of ice cloud optical property parameterizations have been developed and used in models. Earlier schemes reply on cloud temperature and do not care about the ice particle shapes by using spherical particle shape approximation (Platt and Harshvardhan 1998). But, Lorenz-Mie theory derived optical properties turn out to be not adequate in representation of light scattering problem of ice clouds. Smooth-faceted pristine hexagonal column is then selected as an appropriate particle model for ice clouds in a lot of parameterization schemes (Takano and Liou 1989; Fu and Liou 1993; Fu 1996). More complicated ice particle models, which include sophisticated ice shapes like droxtal, bullet rosette, and aggregates, are introduced recently (Mitchell et al. 1996; 2006; Hong et al. 2009). As the ice cloud particle model becomes more and more complicated, uncertainties in ice particle shapes are gradually reduced, but the surface roughness feature of ice crystals is still not considered.

The ice particle surface roughness is caused by the evaporation, sublimation, or riming processes, and is observed in the in situ measurement of ice clouds. Some research studies about ice surface roughness indicate significant effects on ice optical properties and simulated radiative flux (Fu 2007; Yang et al. 2012). But unfortunately, the ice particle surface roughness effect is not yet fully evaluated. There is a need to quantify this effect and possibly implement it into the future ice cloud parameterization schemes to reduce uncertainty.

1.3.3 Contrail optical properties

Contrails are the line-shape ice clouds formed behind the cruising aircraft from the aircraft exhaust. Compared with natural cirrus clouds, the optical properties of contrails have more uncertainties because the understandings of contrails are far less than those of the natural cirrus clouds. Not every model has considered contrails, or has considered contrail as a difference cloud other than natural cirrus. As a result, contrails are regarded as natural cirrus in most models, and they share the same optical properties as natural ice clouds. There are some studies develop contrail optical property parameterization based on spherical and non-spherical ice particles and compare their differences (Marquart et al. 2003; Rap et al. 2010a). The difficulty in developing a contrail optical property parameterization scheme lies in the lack of availability of contrail observation and an appropriate contrail particle model. Without an accurate and appropriate contrail parameterization, the contrail radiative forcing is not well determined.

1.4 Existing problems and challenges

Based on the above discussions, several uncertainties and challenges exist that hamper the development of optical property parameterizations for aerosols and clouds. These issues need to be addressed before further improvements can be made on the dust aerosol and ice cloud optical properties.

1.4.1 Quantify the effect of dust particle nonsphericity on radiance and flux calculations

As previously identified, it is not yet certain whether dust nonsphericity will greatly influence the calculation of radiance and flux. Preliminary results show that the phase function of spherical model is very different from that of the non-spherical model. We intend to find answers to the following questions:

- How do we calculate the bulk scattering properties of the dust aerosol using the non-spherical model? What is the best way to determine the dust particle shape distributions?

- What is the effect of dust nonsphericity on radiance and flux calculation? How important is it compared to the other factors, like refractive indices and particle size distribution?

- What is the effect of dust nonsphericity on broadband flux simulation? Is it important?

1.4.2 Evaluation of ice particle surface roughening on the global cloud radiative effect

Literature review shows that none of the present radiative transfer models and global circulation models implement an ice optical property parameterization scheme that takes ice particle surface roughness into account. Recent advances in observational and theoretical findings allow for further studies of this problem. Specific questions to be addressed include, but are not limited to:

- How do the findings from recent observational and theoretical advances influence the broadband ice optical property parameterization used in models?

- How do the changes in ice optical property which is due to the ice surface roughness effect can further influence the ice cloud radiative forcing simulation in radiative transfer models and GCMs? What's the scale of the forcing?

- Is there a need to include the representation of ice particle surface roughness in the future ice optical property parameterization?

1.4.3 Determination of contrail radiative forcing sensitivity to various factors

Contrail radiative forcing is regarded as the most important effect of aviation on climate. However, there are so many factors in the estimation of contrail radiative forcing that one systematic analysis is needed within a comprehensive framework. This work proposes to investigate the largest uncertainty and provide a best estimate of contrail forcing. The questions to be answered is as follow:

- What is the best contrail optical property parameterization scheme available with the employment of the most up-to-date advances in theoretical and observational studies?

- What is the dependence of contrail radiative forcing on various factors, for example, microphysical properties of contrail and modeling assumptions? Which factor is the most important?

- What is the seasonal variation of contrail radiative forcing? Are there any regional characteristics?

- What is the difference between contrail radiative forcing estimations derived from offline single column radiative transfer models and from online coupled GCMs?

1.5 Descriptions of chapters

This dissertation has three main chapters discussing the optical properties and radiative effects of dust aerosols, natural cirrus clouds and contrails, respectively. In Chapter II, the uncertainties related to the dust aerosol particle shape and refractive index have been uncovered and quantified. In Chapter III, we discuss about the influence of ice particle surface roughening on the global cloud radiative effect. In Chapter IV, new contrail optical property parameterization scheme is developed and global contrail radiative forcing is estimated. Further sensitivity tests reveal the dominant contrail properties that significantly affect radiation. Finally, a summary is concluded in Chapter V.

CHAPTER II

RADIATIVE TRANSFER SIMULATION OF DUST-LIKE AEROSOLS: UNCERTAINTIES FROM PARTICLE SHAPE AND REFRACTIVE INDEX[*]

2.1 Introduction

The impact of mineral dust aerosols on climate is an important atmospheric research subject, because aerosols are known to play a significant role in the climate system energy budget (Haywood and Bougher 2000). Dust aerosols directly absorb and scatter radiation, leading to considerable changes in the atmospheric temperature profile (Slingo et al. 2006), and can act as cloud condensation nuclei to indirectly influence the radiation budget and water cycle in the earth-atmosphere system (Albrecht 1989; Twomey 1977). At present, neither the direct nor indirect effects of dust aerosols are well understood, although significant effort has been focused on the subject.

Modeling the effect of dust aerosols on radiative transfer simulation contributes to a better understanding of the climate (d'Almeida et al. 1991) and improves the inversion techniques used in aerosol remote sensing (Kalashnikova and Sokolik 2002). For example, Feng et al. (2009) found substantial inconsistencies, which stem from the differences between the phase functions of spheroidal and spherical particles, in the look-up tables used for retrieving dust aerosol properties.

---

[*] Reprinted with permission from "Radiative transfer simulation of dust-like aerosols: Uncertainties from particle shape and refractive index" by Yi, B., C. N. Hsu, P. Yang, and S.-C. Tsay, 2011. *Journal of Aerosol Science*, 42, 10, 631-644, Copyright 2011 by Elsevier Limited.

To quantify the dust radiative effect has been the object of several studies (Myhre and Stordal 2001; Sokolik et al. 2001), and many questions remain concerning the uncertainties and the error sources. The refractive index uncertainties are generally accepted as the dominant error source (Myhre and Stordal 2001), but substantial controversy exists regarding the effects of particle shape. Observation and simulation studies (Kalashnikova and Sokolik 2004; Mishchenko et al. 1997; Muñoz et al. 2001; West et al. 1997) have proven dust aerosols to be largely non-spherical and to have scattering phase functions distinctive from those of spheres. Despite the apparent differences in the phase function, Mishchenko et al. (1995) argued the spherical model could be used as a suitable approximation for non-spherical dust in radiative flux simulation. The argument was based on the fact that spheres and spheroids have very similar single-scattering albedo and asymmetry factors. Fu et al. (2009) found the errors in reflectivity and absorptivity resulting from spherical particle approximation to be small and concluded that Mie-theory-based single-scattering properties were suitable for radiative flux calculations. Dubovik et al. (2006) used an ensemble of randomly oriented spheroidal particles to model the single-scattering properties of desert dust aerosols and discussed the effect of particle shape on the retrieval of dust aerosol properties. Other studies (Kahnert and Kylling 2004; Kahnert et al. 2005; Kahnert et al. 2007) re-evaluated the particle shape effect in radiance and flux simulation and concluded that the uncertainty associated with dust non-spherical effect could be as important as its counterpart relevant to the refractive index. To be more specific, using spherical particles in the models can lead to unpredictable errors in the radiative flux simulation,

which depend on the particle size, the surface albedo, and the aerosol optical depth. For example, Mishchenko et al. (2003) found that the aerosol optical depth retrieval could be substantially influenced by the aerosol non-spherical effect, and thus introduced significant errors in radiative flux simulation. Uncertainty in aerosol optical depth can also result from the conversion of aerosol mass to aerosol optical depth in numerical models, in particular those aerosol transport models that do not simulate the aerosol size distribution. Furthermore, constrained by the limited number of available observations, the previous sensitivity studies were confined to only one or two discrete wavelengths.

This study is intended to improve the current understanding of the effect of dust non-sphericity on radiative transfer simulations. Section 2.2 describes the single-scattering property database, the method used to obtain the bulk scattering properties, the introduction of the radiative transfer model, and the cases designed for the present sensitivity study. The results and discussions of the errors in radiance and flux simulation in conjunction with several uncertainties are presented in section 2.3. The conclusions are drawn and summarized in section 2.4.

2.2 Data and method

2.2.1 Single-scattering properties

For this study, the single-scattering properties such as the single-scattering albedo, scattering phase matrix, asymmetry factor, and extinction efficiency of dust-like aerosols are taken from a database developed by Meng et al. (2010). A randomly oriented ellipsoidal particle model with three semi-axis lengths (a, b, and c) was used to

create the database; a and b are the semi-major and semi-minor axes and c is the polar radius. Two corresponding aspect ratios are defined as $\varepsilon_{a/c} = a/c$ and $\varepsilon_{b/c} = b/c$ within the range between 0 and 1. A combination of four methods, the Lorenz-Mie theory code (Bohren and Hoffman 1983), the Amsterdam discrete dipole approximation code (Yurkin and Hoekstra 2009), the T-matrix method code (Mishchenko and Travis 1998), and an improved geometric optics method (Bi et al. 2009; Yang and Liou 1996), was used to calculate the single-scattering properties of dust-like particles with various refractive indices, aspect ratios, and sizes. A brief introduction of the database is provided in the appendix (see Appendix A). Technical details regarding the database can be found in Meng et al. (2010).

To obtain the bulk scattering properties of mineral dust aerosols, the particle size and shape distributions are needed. As a reference, we used the laboratory measured phase matrix and size distribution of feldspar at the 441.6 nm wavelength from the Amsterdam Light Scattering Database (Volten et al. 2001). The particle effective radius is 1.0 µm and the effective variance is 1.0. In some of the sensitivity case studies, we used the following lognormal size distribution to replace the observed size distribution:

$$\frac{dn(r)}{dr} = \frac{N_0}{\sqrt{2\pi}r\sigma \cdot \ln 10} \cdot \exp(-\frac{[\log(r/r_0)]^2}{2 \cdot \sigma^2}), \tag{2.1}$$

where r_0 is the median radius, σ is the standard deviation, and N_0 is the number density. The refractive index is not directly given in the measurement but is estimated to be within the range of 1.5~1.6 + i0.001~0.00001, and, in our study, is assumed to be 1.56 + i0.0005. From the dust-like aerosol optical property database, the shape

13

distribution of ellipsoidal particles was chosen to generate the best-fit of the phase function to the laboratory measurements for feldspar particles by using the optical properties of ellipsoidal particles with ten different aspect ratios.

The bulk scattering properties can be calculated using the following formulas:

$$\overline{P_{11}} = \frac{\sum_{k=1}^{n_k=10} W_k \int_{r_1}^{r_2} n(r) P_{11}(\varepsilon_k, r) Q_{sca}(\varepsilon_k, r) A(\varepsilon_k, r) dr}{\sum_{k=1}^{n_k=10} W_k \int_{r_1}^{r_2} n(r) Q_{sca}(\varepsilon_k, r) A(\varepsilon_k, r) dr}, \tag{2.2}$$

$$\overline{Q_{ext}} = \frac{\sum_{k=1}^{n_k=10} W_k \int_{r_1}^{r_2} n(r) Q_{ext}(\varepsilon_k, r) A(\varepsilon_k, r) dr}{\sum_{k=1}^{n_k=10} W_k \int_{r_1}^{r_2} n(r) A(\varepsilon_k, r) dr}, \tag{2.3}$$

$$\overline{Q_{sca}} = \frac{\sum_{k=1}^{n_k=10} W_k \int_{r_1}^{r_2} n(r) Q_{sca}(\varepsilon_k, r) A(\varepsilon_k, r) dr}{\sum_{k=1}^{n_k=10} W_k \int_{r_1}^{r_2} n(r) A(\varepsilon_k, r) dr}, \tag{2.4}$$

$$\overline{\omega} = \frac{\overline{Q_{sca}}}{\overline{Q_{ext}}}, \tag{2.5}$$

where n is the size distribution, Q_{ext} is the extinction efficiency, Q_{sca} is the scattering efficiency, A is the projected area of the individual particle, r is the radius of the volume equivalent sphere, ε_k denotes the shape of an individual particle, P_{11} is the phase function (the first element of the scattering phase matrix) of an individual particle at a given size and aspect ratio, W_k is the weight of a particular particle shape, $\overline{P_{11}}$ is the bulk phase function, $\overline{Q_{ext}}$ is the bulk extinction efficiency, $\overline{Q_{sca}}$ is the bulk scattering efficiency, and $\overline{\omega}$ is the bulk single-scattering albedo. The weight W_k is determined by the Monte Carlo method to minimize d, defined as the difference between the logarithm

of the bulk ellipsoid phase function ($\overline{P_{11,j}}$) and the observed phase function of feldspar ($P_{11,feldspar,j}$) as follows:

$$d = \sqrt{\sum_{j}^{N}[\log(\overline{P_{11,j}}) - \log(P_{11,feldspar,j})]^2} , \qquad (2.6)$$

where N equals 37 and is the total number of scattering angles used in numerical computation.

Fig. 2.1 shows the comparison between the phase functions from laboratory measurements and from simulations using the spherical and ellipsoidal models at the 441.6 nm wavelength and with an assumed refractive index of $1.56 + i0.0005$.

Fig. 2.2 shows the weights of ten aspect ratios determined by the Monte-Carlo method that contribute to the best-fit phase function compared with the measurement. The mean aspect ratios of the bulk ellipsoid mixture are $\overline{\varepsilon_{a/c}} = 0.409$ and $\overline{\varepsilon_{b/c}} = 0.641$. The phase functions from both the spherical and ellipsoidal models agree reasonably well with the laboratory observations in the forward scattering directions (0°~70°). The spherical model underestimates the phase function at scattering angles between 70° and 140° and has a strong backscattering peak; the phase function of the ellipsoidal model closely agrees with the observations across the entire scattering angle domain.
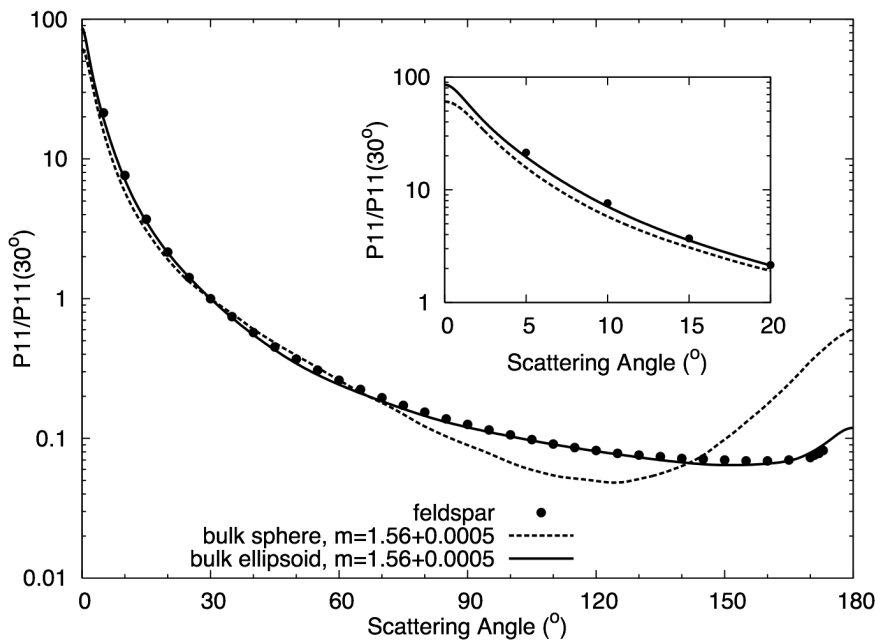
Fig. 2.1 Bulk scattering phase functions for a feldspar sample, spherical, and ellipsoidal dust particles.
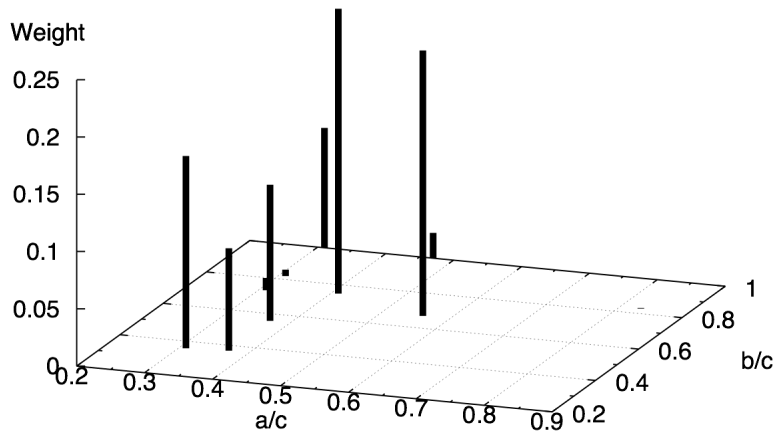
Fig. 2.2 Weights of ten aspect ratios that contribute to the best-fit model simulated phase function compared with the measurement determined from the Monte-Carlo method.

16

2.2.2 Radiative transfer model and simulations

For the simulations, the latest version of the libRadtran (Mayer and Kylling 2005) package with a 32-stream DISORT (Stamnes et al. 1988) radiative transfer solver is used. A standard tropical atmospheric profile with 49 layers (Anderson et al. 1986) is employed. Dust is assumed to be uniformly distributed throughout the layers between 1~5 km with a cumulative optical depth of 0.5. The surface albedo is assumed to be 0.1. Radiance and flux calculations are performed with a solar zenith angle of 45° at the 441.6 nm wavelength.

To assess the non-spherical particle shape effect on radiance and flux simulations as compared to the other factors, the test cases for the present sensitivity studies are listed in Table 2.1. The reference case (case 0) uses the laboratory observed phase function for feldspar particles. Because the measurement only provides the phase function at the scattering angles between 5° and 173° without information about the single-scattering albedo, we use the best-fit phase function of the bulk ellipsoids to extrapolate the phase function to obtain the values at the scattering angles in the regions of 0°~5° and 173°~180°, similar to Nousiainen et al. (2006). Furthermore, the single-scattering albedo is chosen to be the same as for the best-fit bulk ellipsoidal model. Case 1 is designed to determine the relative error in radiance and flux between the simulations using the observed and best-fit phase functions. In cases 2 and 3, some artificial uncertainties are added to the real and imaginary parts of the refractive index in order to quantify the errors associated with the uncertainties in the refractive index. The particle size distribution errors are estimated in cases 4a and 4b where the observational size

17

distribution is replaced with a lognormal distribution containing uncertainties in the effective particle radius (case 4a) and effective variance (case 4b). In case 5, a 20% uncertainty is added to the surface albedo in order to study its effect on the radiative transfer simulation. In case 6, the vertical profile of the dust optical depth is changed to have a non-uniform peak at 3km, but with the same cumulative optical depth of 0.5. The phase function is replaced with the Henyey-Greenstein function in case 7, and case 8 investigates the effect of uncertainty in aerosol optical depth.

Table 2.1 Description of the sensitivity test cases.

Case	Description
0	Reference case
1	Best-fit case
2	With uncertainty in the imaginary part of refractive index: $m = 1.56 + i0.0007$
3	With uncertainty in the real part of refractive index: $m = 1.60 + i0.0005$
4a	With uncertainty in size distribution: lognormal distribution with 10% increase in effective radius
4b	With uncertainty in size distribution: lognormal distribution with 10% increase in effective variance
5	With uncertainty in estimation of the surface albedo: 20% overestimate (0.12)
6	With uncertainty in the vertical distribution of dust optical depth: peak at 3 km with a same cumulative optical depth of 0.5
7	Error due to using the Henyey-Greenstein function
8	With uncertainty in aerosol optical depth: cumulative optical depth = 1

Table 2.2 lists the single-scattering properties for the reference and the sensitivity cases at the wavelength of 441.6 nm. Similar to some former studies (Kahnert 2004; Nousianen and Vermeulen 2003), we find that the single-scattering albedo slightly changes for different particle shapes. But, these changes are not necessarily negligible for absorption. The asymmetry factors for the ellipsoidal model are consistently larger than those of the spherical model but are still quite close to the sensitivity cases.

Table 2.2 Single-scattering properties at the wavelength of 441.6 nm for different experiment test cases

Case	Single scattering albedo (SSA)		Asymmetry factor (g)		ΔSSA	Δg
	Sphere	**Ellipsoid**	**Sphere**	**Ellipsoid**		
1	0.9880	0.9838	0.6835	0.7154	-0.0042	0.0319
2	0.9827	0.9797	0.6851	0.7181	-0.0030	0.0330
3	0.9878	0.9826	0.6678	0.7052	-0.0052	0.0374
4a	0.9872	0.9826	0.6863	0.7168	-0.0046	0.0305
4b	0.9884	0.9843	0.6817	0.7147	-0.0041	0.0330

2.3 Results and discussions

2.3.1 Radiance and flux simulation at the 441.6 nm wavelength

Fig. 2.3 shows the polar plots for downwelling and upwelling diffuse spectral radiances in the reference case at both the bottom (BOA) and the top of the atmosphere

(TOA). The solar zenith and azimuthal angles are 45° and 0°, respectively, the cumulative dust aerosol optical depth (AOD) is 0.5, and the surface albedo is 0.1. Because of the strong forward scattering peak in the dust aerosol phase function, the values of the radiance are large around the direction of incoming solar radiation at the BOA.
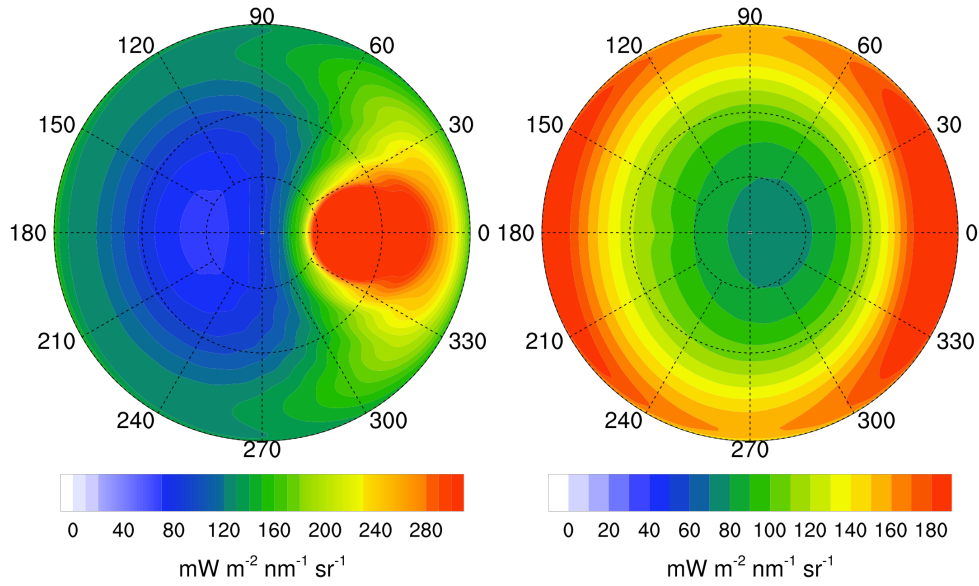
Fig. 2.3 Downwelling diffuse spectral radiance at the BOA (left panel) and upwelling diffuse spectral radiance at the TOA (right panel) in the reference case.

The relative error compared to the reference case for the upwelling spectral radiance at the TOA and the downwelling spectral radiance at the BOA for the spherical and ellipsoidal models is defined as:

$$Err = (I_* - I_{ref})/I_{ref} \cdot 100\%,\qquad(2.7)$$

where I_* indicates the test case radiance (at the BOA or the TOA, either for the spherical or ellipsoidal model) and I_{ref} is the radiance associated with the reference case. Thus, the effects from particle shape and the other factors can be clearly quantified and easily compared.

The ellipsoidal model in case 1 (Fig. 2.4, the best-fit case) yields the smallest errors at both the TOA and the BOA which shows that the numerical fit in Fig. 2.1 is quite accurate. However, the corresponding spherical model has significant errors, particularly in the forward scattering direction at the BOA and in the backward scattering direction at the TOA. The errors are mainly resulted from the phase function associated with the spherical model. When the refractive index has a small uncertainty in the imaginary part (Fig. 2.5, case 2), the errors for both the spherical and ellipsoidal models increase. The errors resulting from the flawed refractive index appear small when compared with the errors associated with the particle shape. The results are similar in case 3 (not shown) when the real part of refractive index has small uncertainties. The variations of the size distribution (case 4a and 4b) do not introduce significant errors, indicating that a 10% difference in the effective radius or the effective variance has little affect on the results. If the surface albedo is overestimated by 20% (case 5), the relative errors increase, particularly at the TOA, but the ellipsoidal model performs better and reduces the errors more than the spherical model. Varying the vertical profile of dust optical depth while keeping the same cumulative optical depth (case 6) produces quite small differences compared to the best-fit case. Case 7 uses the Henyey-Greenstein
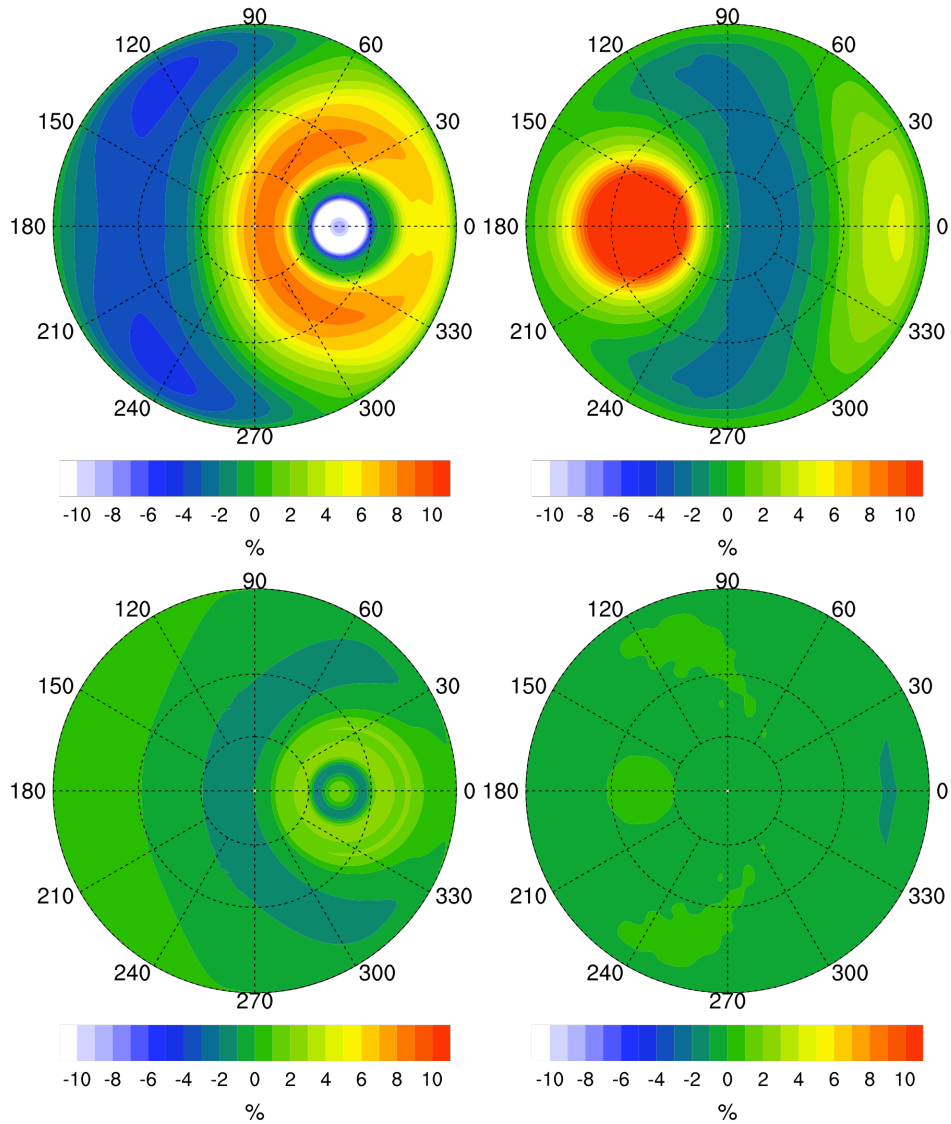
Fig. 2.4 Relative errors compared to the reference case for the upwelling and downwelling spectral radiances at the TOA (right column panels) and the BOA (left column panels) for the spherical model (upper panels) and the ellipsoidal model (lower panels) in the best-fit test case.
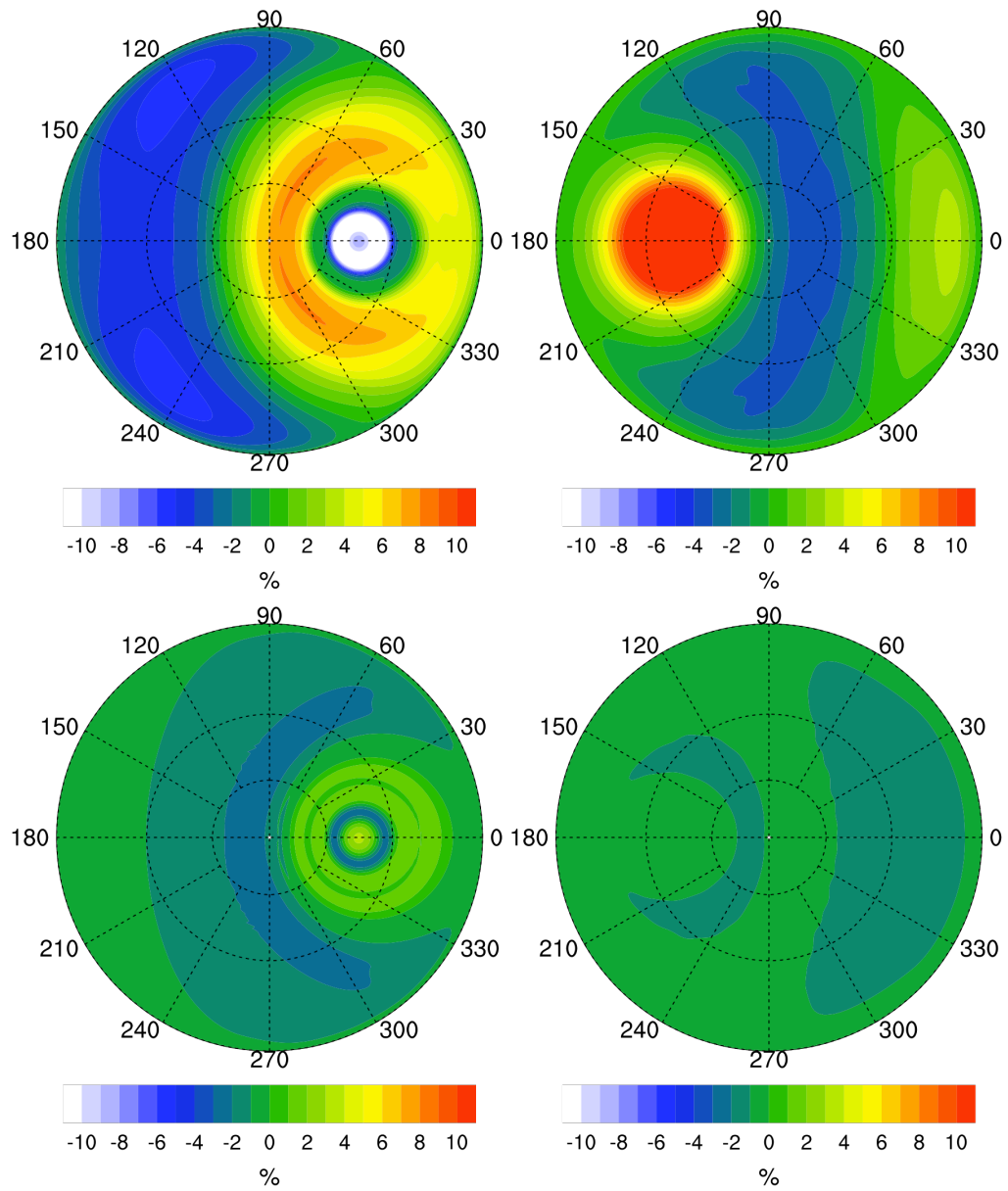
Fig. 2.5 Same as Fig. 2.4, but for test case 2.

function based on the asymmetry factor instead of the exact phase functions. The relative errors are of equal magnitude in both the spherical and ellipsoidal models and are larger than all the above test cases. The results indicate the Henyey-Greenstein function may not be a suitable replacement of the phase function in radiance simulations. Case 8 shows the effect of uncertainty in aerosol optical depth by doubling the dust optical depth. Not surprisingly, this yields the largest error among all the cases. For the ellipsoidal model, the typical relative errors are 10% to 30% at the BOA and 8% to 20% at the TOA, and can be up to 40% and 25% for the BOA and the TOA at a certain viewing angles, respectively. Therefore, the ellipsoidal model appears to be a better choice than the spherical model for the simulation of the angular distribution of radiative energy. The effect of the non-spherical dust particle shape may be of equal or even greater importance than other factors such as the refractive index.

The flux simulation results for all the cases are summarized in Table 2.3. Dust forcings and the their errors relative to the best-fit case are given to quantify the differences in flux simulation in the various test cases. An additional "No dust" case containing no dust aerosols is selected for comparison. Thus, the dust forcing ΔF is calculated as:

$$\Delta F = F_{dust} - F_{no\ dust},$$ (2.8)

where F_{dust} is the net flux in the cases with dust aerosols included and $F_{no\ dust}$ is the net flux in the dust-free case. The dust forcing on atmospheric absorption is defined as:

$$\Delta F_{abs} = \Delta F_{TOA} - \Delta F_{BOA},$$ (2.9)

where ΔF_{TOA} and ΔF_{BOA} are the dust forcings at the TOA and the BOA, respectively.

The error in dust forcing is defined as:

$$\Delta F_{diff} = \Delta F - \Delta F_1, \tag{2.10}$$

where ΔF_1 is the dust forcing for the best-fit case (case 1) using the spherical/ellipsoidal model.

From Table 2.3, we are able to evaluate the effect of various factors separately on flux simulation. In cases 2 and 3 with the uncertainties in the real and imaginary parts of the complex refractive index, the ellipsoidal model tends to be less sensitive to an uncertainty in refractive index by introducing smaller changes in flux simulation. In addition, case 2 shows increased dust forcing on atmospheric absorption, especially when using the spherical model. According to Myhre and Stordal (2001), dust radiative forcing is strongly sensitive to the size distribution when the optical properties derived from Mie theory are used. However, we find the particle size distribution and the increases in the effective radius and effective variance has little effect on radiative forcing simulation. The different settings and approximations give rise to the differences between the present results and the former study. With a 20% increase in surface albedo, the results from case 5 show that the errors in flux at the TOA and the BOA are comparable to those in case 2, while the atmospheric absorption is not quite affected. It should be noted that the clear-sky flux and aerosol-sky flux to derive the dust forcings in case 5 are calculated with the same surface albedo (0.12) instead of 0.1. Almost no difference is found in flux simulation when the vertical dust optical depth profile is

Table 2.3 Simulated dust forcing and the error at the TOA and the BOA and for atmospheric absorption compared with the best-fit case at the wavelength of 441.6 nm. The simulated net flux/dust forcing for the reference case: TOA: 878.55/-61.92; BOA: 852.69/-80.75.

Case		Dust forcing (mW m^{-2} nm^{-1})		Error (mW m^{-2} nm^{-1})	
		Sphere	Ellipsoid	Sphere	Ellipsoid
1	TOA	-70.35	-61.12	N/A	N/A
	BOA	-84.55	-79.93	N/A	N/A
	ATM	14.20	18.81	N/A	N/A
2	TOA	-67.78	-58.90	2.57	2.22
	BOA	-87.86	-82.21	-3.31	-2.28
	ATM	20.08	23.31	5.88	4.50
3	TOA	-73.89	-62.94	-3.54	-1.82
	BOA	-88.36	-83.05	-3.81	-3.12
	ATM	14.47	20.11	0.27	1.30
4a	TOA	-69.42	-60.39	0.93	0.73
	BOA	-84.49	-80.49	0.06	-0.56
	ATM	15.07	20.10	0.87	1.29
4b	TOA	-70.74	-61.33	-0.39	-0.21
	BOA	-84.51	-79.56	0.04	0.37
	ATM	13.77	18.23	-0.43	-0.58
5	TOA	-67.17	-58.09	3.18	3.03
	BOA	-81.59	-77.20	2.96	2.73
	ATM	14.42	19.11	0.22	0.30
6	TOA	-70.34	-61.10	0.01	0.02
	BOA	-84.55	-79.94	0.0	-0.01
	ATM	14.21	18.84	0.01	0.03
7	TOA	-68.99	-59.98	1.36	1.14
	BOA	-83.33	-78.95	1.22	0.98
	ATM	14.34	18.97	0.14	0.16
8	TOA	-131.48	-114.86	-61.13	-53.74
	BOA	-160.64	-153.38	-76.09	-73.45
	ATM	29.16	38.52	14.96	19.71

changed from uniform to non-uniform (case 6). These results are similar to those of Myhre and Stordal (2001) who found the solar radiative forcing to be relatively insensitive to aerosol altitude in comparison with the case of thermal radiative forcing. Significant errors occur in radiance simulation when the Henyey-Greenstein function is used instead of the exact phase functions, but the Henyey-Greenstein function is an adequate approximation in the flux simulation (case 7) because the error caused by using the Henyey-Greenstein function is still not larger than cases 2 and 3 when conservative uncertainties in refractive index are assumed. Case 8 proves that the uncertainty in aerosol optical depth can further influence the effect of particle shape.

2.3.2 Broadband flux simulation over the solar spectrum

By applying similar settings and parameters as previously, we can estimate the integrated effect of dust particle shape on flux simulation over the whole solar spectrum. Additionally, variations in spectral surface albedo, optical depth, and refractive index have been considered in estimating the magnitudes of the errors caused by these factors under various conditions. Note that we used the same particle shape distribution identified at the wavelength of 441.6 nm in the broadband simulation. This is due to the limited number of observational results of the scattering phase function. It is therefore unclear whether this fixed shape distribution performs equally well at the wavelengths other than 441.6 nm.

Different from the wavelength-independent surface albedo used above, the spectral surface albedo derived from the ASTER spectral library version 2.0 (Baldridge

et al. 2009) has been used. To compare their different effects, two distinctive sets of surface albedo have been chosen, including one over sandy land and one over water.

The cumulative dust optical depth at the 0.55 μm wavelength ($\tau_{0.55}$) is assumed to be 0.5 or 1. The optical depth at other wavelengths is obtained by:

$$\tau = \frac{\overline{Q_{ext}}}{\overline{Q_{ext,0.55}}} \cdot \tau_{0.55}, \qquad\qquad (2.11)$$

where $\overline{Q_{ext}}$ and $\overline{Q_{ext,0.55}}$ are the extinction efficiencies at a given wavelength and at 0.55 μm, respectively.

The refractive indices for dust-like aerosols in the solar spectrum are taken from the database compiled by Levoni et al. (1997) and are shown in Fig. 2.6. The calculation is for the solar spectrum ranging from 0.3 to 4.5 μm. In this spectral region, the real part of the refractive index decreases whereas the imaginary part increases with wavelength, indicating the dust absorption increases. To quantify their effects, two sensitivity experiments with a 5% decrease in the real and imaginary parts of the refractive index have been conducted. The imaginary parts of complex refractive indices from Levoni et al. (1997) are actually higher than some more recent studies (McConnel et al. 2010) and the value of 0.0005 that we adopted for 441.6 nm. These values were chosen in order to be consistent with the scattering property database by Meng et al. (2010), but, it should be noted that the particle shape effects could be affected by using such strongly absorbing aerosol particles.
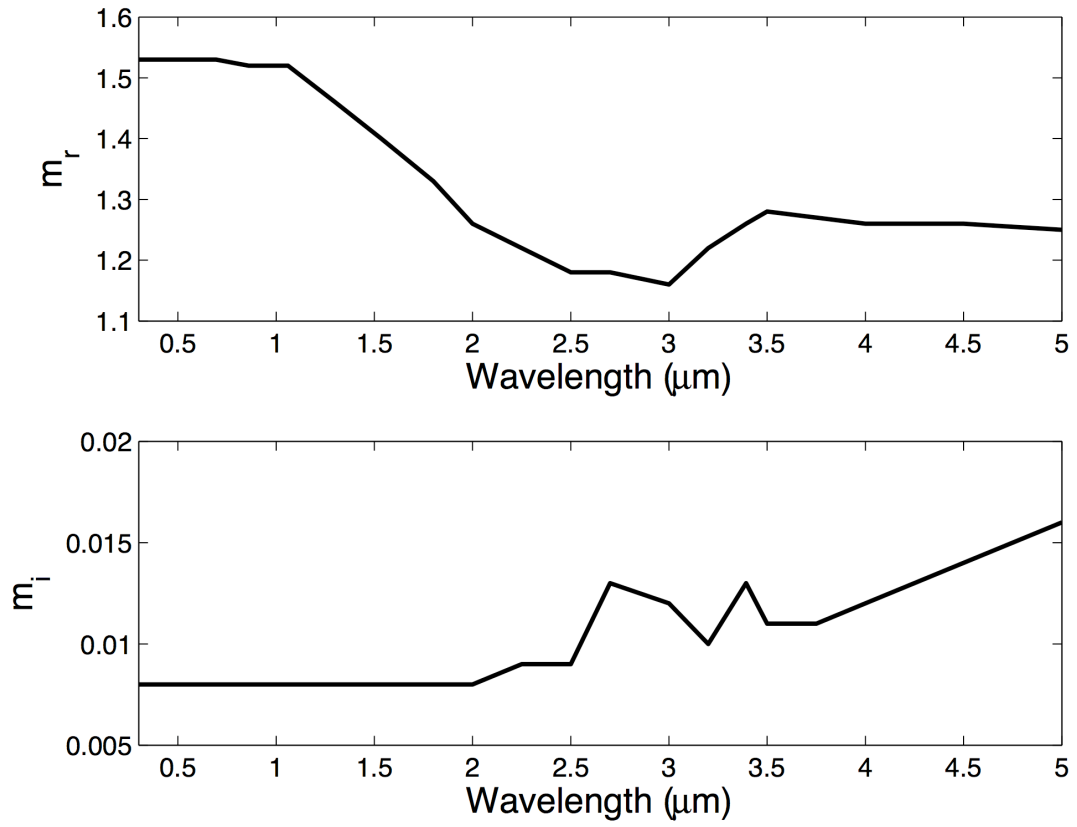
Fig. 2.6 The dust-like aerosol refractive index: real part (upper panel) and imaginary part (lower panel) following Levoni et al (1997).
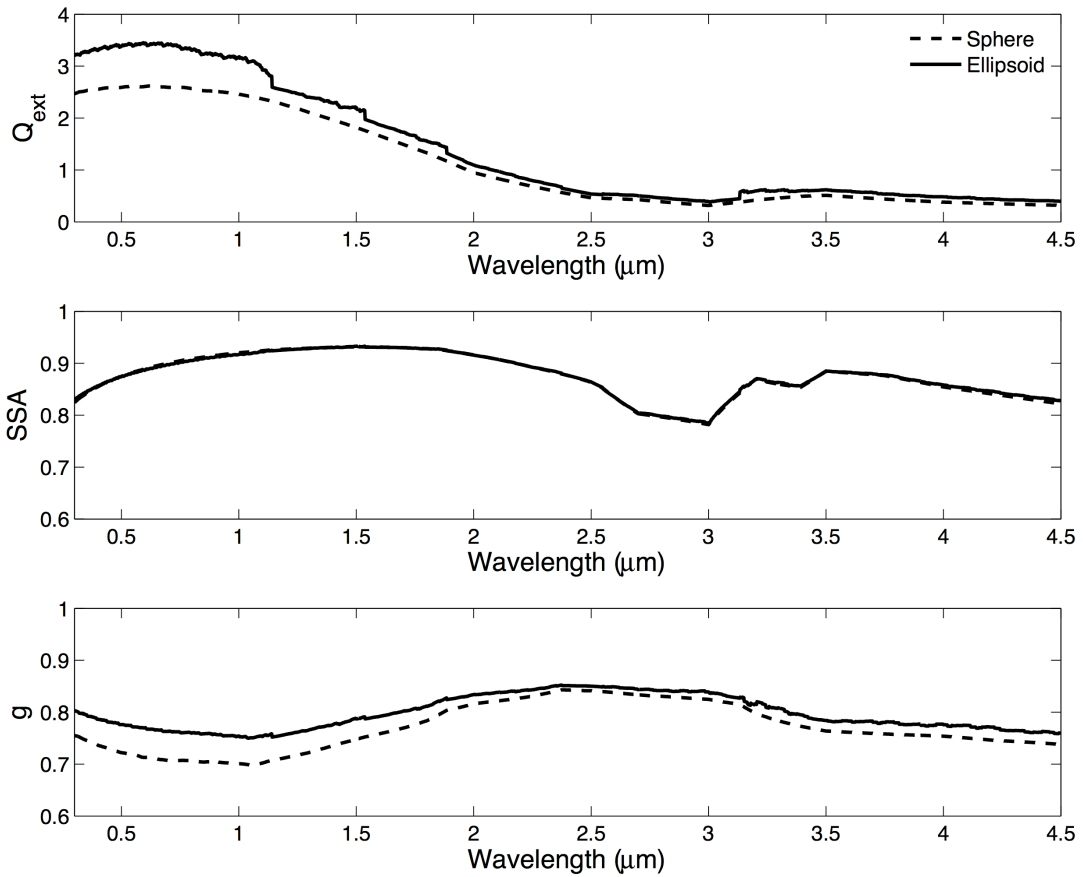
Fig. 2.7 Bulk scattering properties for spherical and non-spherical models in the spectral region from 0.3 μm to 4.5 μm: extinction efficiency (upper panel), single-scattering albedo (middle panel), and asymmetry factor (lower panel).

30

Shown in Fig. 2.7 are the bulk scattering properties of the spherical and non-spherical model of particles in the spectral region from 0.3 μm to 4.5 μm. Although significant differences in the scattering properties are found between the spherical and non-spherical models, similarities are observed in the trends of the variation of the scattering properties as a function of wavelength in the two cases. The extinction efficiency has a peak around 0.7 μm and decreases almost monotonically to 3.0 μm, and shows a second small peak at 3.5 μm. The single-scattering albedo, instead, peaks around 1.5 μm and again is lowest at 3.0 μm. The asymmetry factor has a maximum in the middle of this spectral region (2.5 μm) and minimums at the two ends (1.0 μm and 4.5 μm). Except for the single-scattering albedo, which has a minor difference due to particle shape, the differences in the other scattering properties show apparent spectral variability. The spherical and non-spherical difference in extinction efficiency is the largest in the visible wavelengths and generally decreases with increasing wavelengths. Differences in the asymmetry factors between spheres and ellipsoids are the smallest around 2.5 μm, whereas at the other wavelengths, the asymmetry factors are larger for ellipsoids than spheres.

An example of the simulated net flux over a sandy surface with cumulative dust optical depth of 0.5 is given in Fig. 2.8. The upper panels of Fig. 2.8 show the dust forcings induced by spherical and ellipsoidal dust aerosols. It is found that spherical dust forcings tend to be stronger than ellipsoidal dust forcings in the solar spectrum, and the dust forcings at the BOA are much larger than their counterparts at the TOA. Not
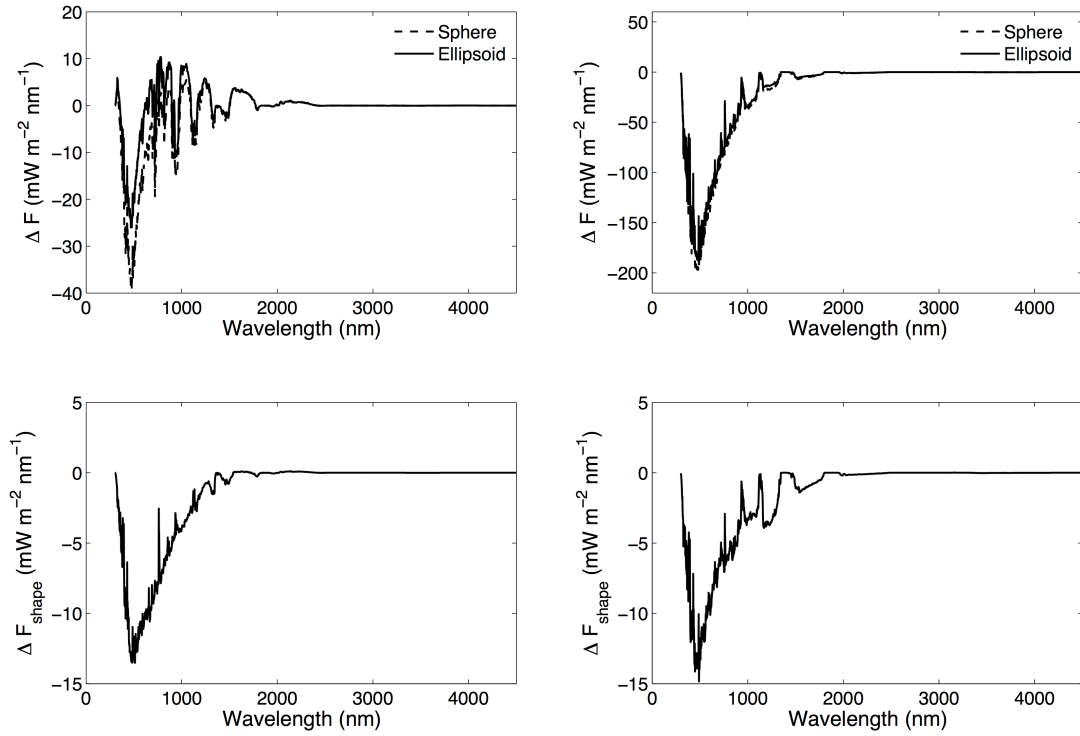
Fig. 2.8 Simulated spectral dust forcings (upper panels) and the particle shape effects (lower panels) in the solar spectrum at the TOA (left panels) and the BOA (right panels) with the spherical and ellipsoidal models over a sandy surface with a cumulative dust optical depth of 0.5.
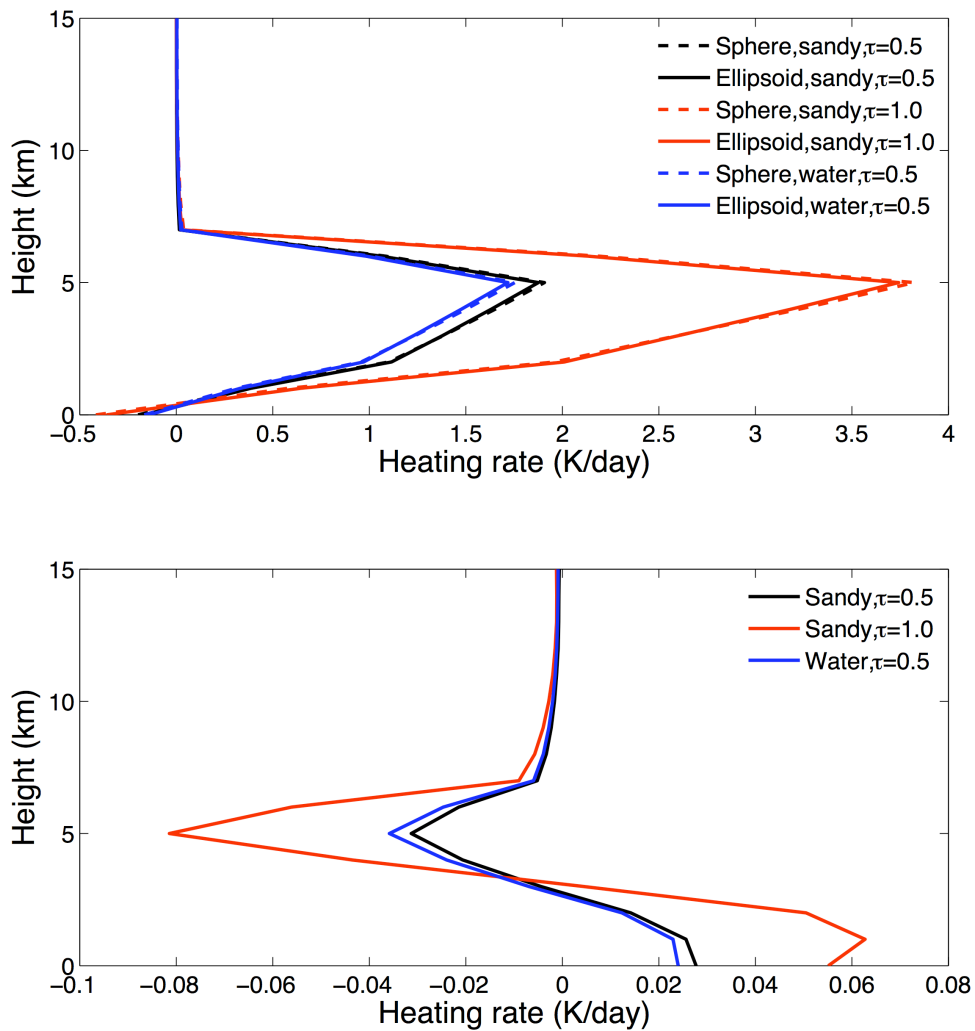
Fig. 2.9 Dust vertical instantaneous heating rate profile of the spherical model and the ellipsoidal model (upper panel) and the particle shape effect (lower panel) with various surface types and dust thickness conditions.

surprisingly, the dust forcing has the largest peak around the visible wavelengths where the incoming solar radiation is the strongest. The particle shape effect on flux simulation can be obtained by comparing the difference in dust forcing at the TOA and the BOA between the spherical and ellipsoidal models (Fig. 2.8, lower panels, spherical case minus ellipsoidal case). Similarly, the largest shape effect, more than 14 mW m^{-2} nm^{-1}, is also in the visible wavelength spectrum. The shape effect is comparable at the BOA and the TOA, with the integrated shape effect in the solar spectrum of 6.3 Wm^{-2} at the BOA and 6.1 Wm^{-2} at the TOA. The particle shape effect on the atmospheric absorption is quite limited in the short-wave spectral region. One of the reasons for the flux differences between the spherical and ellipsoidal models is that ellipsoid has a larger asymmetry factor (thus, less backward scattering) which gives rise to weaker dust forcing at the TOA and the BOA. Another reason could be resulted from the contribution of the optical depth. From Fig. 2.7 (upper panel) and Eqs. (2.11), we could find that the optical depths for ellipsoids are usually smaller than those for spheres in this spectral region when we assume that the optical depths at 0.55 μm are the same for spherical and ellipsoidal model.

Fig. 2.9 shows various effects associated with particle shape in terms of the instantaneous vertical heating rate profile from 0 to 15 km with different surface types and different cumulative dust optical depths. From the figure, it is evident that dust aerosols mainly contribute to atmospheric heating in the dust layer. The strongest heating rate occurs near the top of the dust layer at an altitude of 5 km. However, minor cooling effects at the surface are also simulated. The non-spherical particle shape effect

has a contradictory contribution to the vertical heating rate profile above or below the center of dust layers (which are uniformly distributed between 1~5 km and centered at 3 km). Below 3 km, the particle shape effect warms both the lower atmosphere and the surface. Above 3 km, the non-spherical feature of dust aerosols cools the atmosphere with the strongest cooling at about 5 km altitude near the top of the dust layers. With the same cumulative dust optical depth, the sandy surface and water surface do not exhibit much difference in heating rates. However, the particle shape effect significantly increases when the cumulative dust optical depth is large.

A detailed list of results of dust forcings at the TOA and the BOA using the spherical and ellipsoidal models under different conditions are given in Table 2.4. In each case study, the values shown in the second line are the results from the sensitivity experiment that has a 5% decrease in the real part of refractive index, and the values in the third line are from the sensitivity test that has a 5% decrease in the imaginary part of refractive index. If the same amount of dust is prescribed, the particle shape effect is usually larger over water surfaces than sandy surfaces. A larger dust optical depth gives rise to a larger shape effect. Over water surfaces, the differences in dust forcing at the TOA, as a result of particle shape, are very large (up to 30%) for the cases with cumulative optical depth of 0.5 and 1.0. The same decrease percentages in the real and imaginary parts of the refractive indices result in very different dust forcing responses. A 5% variation in the imaginary part of the refractive index is far less effective than a 5% change in the real part. From the results shown in Table 2.4, we conclude that particle

35

shape and the refractive indices are among the largest uncertainties in the dust radiative

transfer simulation.

Table 2.4 Integrated net flux of dust forcing at the TOA, the BOA and the dust forcing of atmospheric absorption using spherical/ellipsoidal model under various conditions. For the results in each case study (i.e., each of rows 3-6 in the table), the numbers in the second line denote the results from the sensitivity test with 5% decrease in the real part of the refractive index, and the numbers in the third line denote the results from the sensitivity test with 5% decrease in the imaginary part of the refractive index.

Conditions		Integrated Net Flux (W/m^2)					
Surface type	Optical depth	TOA		BOA		ATM	
		Sphere	Ellipsoid	Sphere	Ellipsoid	Sphere	Ellipsoid
Sandy	0.5	-7.2	-1.1	-77.3	-71.0	70.1	69.9
		-2.9	1.5	-71.5	-65.7	68.6	67.2
		-8.2	-2.0	-76.1	-69.8	67.9	67.8
Sandy	1.0	-14.4	-3.5	-147.6	-136.6	133.2	133.1
		-6.9	1.1	-137.7	-127.4	130.8	128.5
		-16.4	-5.2	-145.5	-134.5	129.1	129.3
Water	0.5	-35.4	-26.7	-99.2	-90.1	63.8	63.4
		-28.6	-22.3	-90.9	-83.1	62.3	60.8
		-36.1	-27.3	-97.9	-88.8	61.8	61.5
Water	1.0	-62.9	-48.2	-186.3	-170.9	123.4	122.7
		-51.6	-40.8	-172.4	-158.9	120.8	118.1
		-64.3	-49.3	-184.0	-168.6	119.7	119.3

Finally, a sensitivity test was carried out to check whether the Monte Carlo

approach (see section 2.2.1) for determining the shape distribution results in robust

radiative fluxes. As a simple investigation of how the different shape distributions will

further influence the broadband flux simulation, we choose the ten best particle shape

distributions determined by the Monte Carlo method and calculate the broadband fluxes respectively. The phase functions thus derived all show good agreements with observation, but relatively large diversities exist between the scattering angle 0°~5° and 173°~180°. In the case with sandy surface and aerosol optical depth of 0.5, the standard deviations in simulated broadband net fluxes of dust forcing at the TOA and the BOA are 1.25 W/m^2 and 1.20 W/m^2, as compared with the corresponding differences in flux between spherical and ellipsoidal model (6.1 W/m^2 at the TOA and 6.3 W/m^2 at the BOA). The results indicate that the Monte Carlo approach is rather robust because the standard deviations are much smaller than the corresponding shape effects.

2.4 Conclusions

In this study, we revisited the effect of dust particle shape on the simulations of atmospheric radiance and flux. We used a newly developed optical property database calculated with a tri-axial ellipsoidal model in conjunction with laboratory measurements for feldspar particles. With the proper particle size and shape distributions, the phase function of the ellipsoidal model could match the laboratory observations quite well. Although the corresponding spherical model had large errors in the phase function, the other single-scattering properties were very close to the laboratory measurements. Based on the optical properties obtained, several sensitivity test cases were designed to investigate and quantify the role of different factors in radiance and flux simulations at a single wavelength of 441.6 nm with a fixed solar zenith angle of 45°. For radiance simulation, the spherical model caused significant

errors, and the particle shape errors were comparable to the errors caused by uncertainties in refractive index and the surface albedo. Replacing the phase function with the Henyey-Greenstein function also led to erroneous simulations of angular energy distribution. For flux simulation, the particle shape effect was prominent and contributed to approximately 15% errors at the TOA, 5% errors at the BOA, and 25% errors in the dust forcing on atmospheric absorption for all test cases. When uncertainties were present in size distribution and vertical distribution of dust aerosols, relatively small errors were introduced. Although replacement of the phase function with the Henyey-Greenstein function based on the asymmetry factor induced significant error in radiance simulation, the Henyey-Greenstein function is an adequate approximation for flux simulation. Uncertainty in aerosol optical depth is also proved to be an important factor.

As a first attempt, to the best of the authors' knowledge, we tried to quantify the dust particle shape effect on flux simulation over a wide solar spectrum spanning from 0.3 to 4.5 µm. Assuming the solar zenith and azimuthal angles to be 45° and 0°, respectively, and the cumulative dust AOD to be 0.5 at 0.55 µm wavelength in conjunction with spectral sandy surface albedo, the largest effect was approximately 14 mW m^{-2} nm^{-1} at the 0.4 µm wavelength, and the integrated effect was 6.1 W m^{-2} and 6.3 W m^{-2} at the TOA and the BOA, respectively. In terms of instantaneous heating rate in the atmosphere, dust aerosols tend to heat the dust layers. Distinctive non-spherical particle shape effects were noticed above (cooling effect) and below (warming effect) the center of the dust layers. The intensity of the heating or cooling effect would vary depending on the amount of dust prescribed. In the case of a dust storm, the dust optical

depth would be much higher than 0.5, thus the dust particle shape effect could be significantly increased. Detailed analysis of the dust forcing in various sensitivity test cases showed the particle shape effect could be as important as the refractive index uncertainty. The particle shape effect is particularly large over water surfaces and can contribute to a 30% difference in dust forcing at the TOA.

3.1 Introduction

Ice clouds significantly influence the radiation budget of the climate system (Liou 1986; Lynch et al. 2002; Baran 2009 and references therein), and also influence the large-scale circulations in the atmosphere (Hartmann et al. 1992). The quantification of the radiative effects of ice clouds has been the objective of numerous studies from both satellite/ground-based observations and numerical modeling (e.g. Platt et al. 1998; Comstock et al. 2002; Yang et al. 2007; Lee et al. 2009; Baran 2012 and references therein). However, due to various uncertainties, ice clouds still remain one of the least known components in the atmospheric system. The uncertainties are caused by many factors, from microphysical properties, such as the range of particle size distributions (PSD) with their associated crystal shapes (habits), to optical properties such as extinction coefficient, phase matrix, single-scattering albedo and asymmetry factor. Modeling studies by Slingo and Slingo (1988; 1991) show significant sensitivity of climate models to cloud radiative effect. Thus, it is imperative to accurately represent both ice cloud microphysical and optical properties in atmospheric numerical models.

---

[*] Reprinted with permission from "Influence of ice particle surface roughening on the global cloud radiative effect" by Yi, B., P. Yang, B. A. Baum, T. L'Ecuyer, L. Oreopoulos, E. J. Mlawer, A. J. Heymsfield, and K.-N. Liou, 2013. *Journal of the Atmospheric Sciences*, in press, Copyright 2013 by American Meteorological Society.

Many ice cloud optical property parameterization schemes have been suggested for use in atmospheric models. Early schemes parameterized optical properties as functions of temperature based only on limited observations (e.g., Platt and Harshvardhan 1988). By assuming ice particles to have spherical shape which is the same as liquid clouds (Slingo 1989), the optical properties of ice clouds were derived from the Lorenz-Mie theory. It soon became apparent that the Lorenz-Mie solution was inadequate for representing the scattering and absorbing properties of non-spherical ice particles because ice cloud particle shapes are complex. Takano and Liou (1989) used smooth-faceted hexagonal columns as the ice crystal model of choice and developed a parameterization scheme based on this habit. Ebert and Curry (1992) also employed the hexagonal column model and parameterized ice cloud optical properties as functions of ice water path and the effective particle radius. Fu and Liou (1993) developed a parameterization for use in their own radiative transfer code, which has subsequently been updated (Fu 1996; Fu et al. 1998). In the Community Earth System Model (CESM), which uses the general circulation model version of the radiation code RRTM (known and hereafter referred to as RRTMG), the ice cloud optical property parameterization (Mitchell et al. 1996; 2006) is based on a combination of the anomalous diffraction theory (ADT) approximation and a database by Yang et al. (2000). Hong et al. (2009) developed a new parameterization for ice cloud bulk optical properties as a function of effective particle size for use in climate models based on six ice habits and observed ice particle size distributions from several field campaigns, again assuming smooth particle surfaces. It is important to note that the evolution in

parameterization scheme development has been toward the use of more ice particle habits and more realistic ice particle size distributions, but with limited consideration of surface roughness. One of the exceptions is Edwards et al. (2007) whose parameterization scheme using an ice aggregate model accounts for roughened surfaces and was implemented in the HadAM3 GCM.

A focus of recent research has been on uncertainty reduction in ice cloud properties as more field campaign data become available (Heymsfield et al. 2010; 2013) from both hemispheres. Additionally, theoretical advances help to simulate ice particle optical properties more accurately by including more sophisticated ice particle shapes and considering ice surface roughness (Yang et al. 2000; Yang et al. 2003; Zhang et al. 2004; Yang et al. 2008; Zhang et al. 2009). How the findings from these observational and theoretical advances influence ice cloud radiative effect is the focal point of this study, specifically the influence of ice particle surface roughness on radiative transfer and climate simulations.

Ice particles are most likely not pristine, and may include air bubbles, internal fractures, and other inhomogeneities. In situ observations indicate that ice particles tend to have rough surfaces due to the evaporation, sublimation or riming processes (Cross 1969; Ono 1969; Davy and Branton 1970; Ulanowski et al. 2006; 2012). It is still unknown how ubiquitous the surface roughness feature is among ice cloud particles. Previous studies have shown the importance of ice particle surface roughness effects and the need for them to be accounted for in the computation of ice cloud radiative effect (Macke 1993; Yang and Liou 1998). Fu (2007) considers the ice surface roughness

effect on the asymmetry factor and treats it by neglecting the contribution from delta transmission, obtaining an approximate 20 Wm^{-2} impact in the reflected solar flux. A recent study by Yang et al. (2012) shows 10-15 Wm^{-2} differences in upward and downward solar fluxes due to an assumed reduction in the asymmetry factor induced by ice particle roughness. The primary shortcoming of the previous studies is an over-simplified representation of ice particle surface roughness. Another shortcoming is the application of single column radiative transfer codes to a limited number of individual cases, thereby limiting the representativeness of the results. These earlier studies helped however establish the need to update the effects of ice crystal roughness on optical property parameterizations and to revisit the radiative forcing estimates. Both issues are pursued comprehensively in this paper. We describe the data and methodology used in this study in section 3.2. Section 3.3 shows the simulated ice roughness effects by single column radiative transfer models (RTMs) and an AGCM. A summary and conclusions are given in section 3.4.

3.2 Data and methodology

3.2.1 Ice particle single-scattering property database

In this study, the single-scattering properties for nine ice particle habits from the ultraviolet to the far-IR are provided in a library recently developed by Yang et al. (2013). The library is developed using the most up-to-date ice refractive index values (Warren and Brandt 2008) currently available. The habits are those most often found in clouds and include droxtals, plates, solid and hollow columns, solid and hollow bullet

rosettes, an aggregate of solid columns, and a small/large aggregate of plates. The calculations implement a new treatment of forward scattering (Bi et al. 2009) that considers the ray-spreading effect more accurately. With this new treatment, the delta-transmission term is no longer necessary. What makes the library optimal for use here is the availability of three ice particle surface roughness conditions for each habit: completely smooth, moderately roughened, and severely roughened, following the approximate approach discussed in Yang et al. (2008). The method of particle surface roughness treatment can be found in the appendix. The severely roughened ice particles compare best with global Cloud Aerosol Lidar with Orthogonal Polarization (CALIOP) backscattering data (Baum et al. 2011) and also with PARASOL (Polarization and Anisotropy of Reflectances for Atmospheric Sciences coupled with Observations from a Lidar) polarized reflection data (C.-Labonnote et al. 2001; Cole et al. 2013). Our approach in this paper is to perform calculations for the completely smooth and the severely roughened cases (referred to as "CS case" and "SR case", respectively), and quantify resulting flux differences as the surface roughness effect.

3.2.2 Microphysical data and ice habit mixture

A total of 14,408 particle size distributions (PSDs) derived from eleven field campaigns carried out in different locations are used in this study. Heymsfield et al. (2013) describe the data in more detail. The microphysical data were reprocessed where necessary to mitigate the ice particle shattering effect on the PSDs. A general habit mixture scheme is adopted that uses all nine habits (Baum et al. 2011). The same ice

habit mixture scheme is adopted in remote sensing studies of ice cloud using CALIOP (Baum et al. 2011) and PARASOL (Cole et al. 2013). These microphysical data are used for the calculation of the bulk scattering properties for the individual shortwave (SW) and longwave (LW) bands of the RTMs.

3.2.3 Calculation of the ice cloud bulk scattering properties

The method to calculate the ice cloud bulk scattering properties follows previous studies (Baum et al. 2005; Baum et al. 2011). The effective particle diameter (Foot 1988; Yang et al. 2000; Mitchell 2002) is defined as:

$$D_{eff} = \frac{3}{2} \frac{\sum_{h=1}^{M}\left[\int_{D_{min}}^{D_{max}} V_h(D)f_h(D)n(D)dD\right]}{\sum_{h=1}^{M}\left[\int_{D_{min}}^{D_{max}} A_h(D)f_h(D)n(D)dD\right]}, \tag{3.1}$$

where D is particle maximum dimension; D_{min} and D_{max} are the minimum and maximum ice particle dimensions; V_h and A_h are the volume and area of an ice particle with habit h; M is the number of habits; f_h is the habit fraction of habit h that depends on the ice particle size; and n is the number concentration.

Band-averaged bulk optical properties of ice clouds are calculated by integration over both particle size and appropriate wavelength band limits. For this study, the mass extinction coefficient, the single-scattering albedo, and asymmetry factor over a band are provided by:

$$k_{ext} = \frac{\int_{\lambda_{min}}^{\lambda_{max}} \int_{D_{min}}^{D_{max}} \sum_{h=1}^{M} [Q_{ext,h}(D,\lambda)A_h(D)f_h(D)]S(\lambda)n(D)dDd\lambda}{\int_{\lambda_{min}}^{\lambda_{max}} \int_{D_{min}}^{D_{max}} \sum_{h=1}^{M} [V_h(D)f_h(D)]S(\lambda)n(D)dDd\lambda},$$ (3.2)

$$\overline{\sigma}_{sca} = \frac{\int_{\lambda_{min}}^{\lambda_{max}} \int_{D_{min}}^{D_{max}} \sum_{h=1}^{M} [\sigma_{sca,h}(D,\lambda)f_h(D)]S(\lambda)n(D)dDd\lambda}{\int_{\lambda_{min}}^{\lambda_{max}} \int_{D_{min}}^{D_{max}} \sum_{h=1}^{M} [f_h(D)]S(\lambda)n(D)dDd\lambda},$$ (3.3)

$$\overline{\sigma}_{ext} = \frac{\int_{\lambda_{min}}^{\lambda_{max}} \int_{D_{min}}^{D_{max}} \sum_{h=1}^{M} [\sigma_{ext,h}(D,\lambda)f_h(D)]S(\lambda)n(D)dDd\lambda}{\int_{\lambda_{min}}^{\lambda_{max}} \int_{D_{min}}^{D_{max}} \sum_{h=1}^{M} [f_h(D)]S(\lambda)n(D)dDd\lambda},$$ (3.4)

$$\overline{\omega}(\lambda) = \frac{\overline{\sigma}_{sca}(\lambda)}{\overline{\sigma}_{ext}(\lambda)},$$ (3.5)

$$g = \frac{\int_{\lambda_{min}}^{\lambda_{max}} \int_{D_{min}}^{D_{max}} \sum_{h=1}^{M} [g_h(D,\lambda)\sigma_{sca,h}(D,\lambda)f_h(D)]S(\lambda)n(D)dDd\lambda}{\int_{\lambda_{min}}^{\lambda_{max}} \int_{D_{min}}^{D_{max}} \sum_{h=1}^{M} [\sigma_{sca,h}(D,\lambda)f_h(D)]S(\lambda)n(D)dDd\lambda},$$ (3.6)

where λ_{max} and λ_{min} are the upper and lower wavelength limits of a given SW/LW band; $\sigma_{sca,h}$ is the scattering cross section for habit h; $\sigma_{ext,h}$ is the extinction cross section for habit h; $Q_{ext,h}$ is the extinction efficiency; and $S(\lambda)$ is the solar spectrum (Chance and Kurucz 2010) for SW bands. For LW bands, the solar spectrum is replaced with the Planck function assuming a cloud temperature of 233 K. Note that these assumptions are adopted for practical reasons because the number of distinct in-atmosphere solar spectra and cloud temperatures is too large to consider all possible combinations. We find that the band-averaged optical properties are largely insensitive to these assumptions. Two

cases of ice particle surface roughness (CS and SR) are considered separately. The influence of meteorological conditions (i.e. temperature and humidity) on ice particle surface roughness is not included in this study because the nature of these physical mechanisms is not sufficiently known.

3.2.4 The RTMs and AGCM

The bulk single–scattering properties are parameterized subsequently as functions of the effective particle diameter and implemented in the Fu-Liou and the RRTMG RTM codes, and the Community Atmosphere Model (CAM5.1) AGCM. The Fu-Liou RTM has 6 solar bands and 12 IR bands; the RRTMG package (Iacono et al. 2008) has 14 solar bands and 16 IR bands. The spectral bands in the Fu-Liou and RRTMG RTMs are given in Table 3.1. Both use the correlated-k distribution method to treat absorption by atmospheric gases.

In the next section, results are presented for our new ice cloud models to demonstrate the flux differences caused solely by assumptions about particle roughness.

3.3 Results and discussion

3.3.1 Broadband RTM results

The differences in ice cloud optical properties between the CS and SR cases are shown in Fig. 3.1. The CS results show that the mass extinction coefficient decreases sharply with an increase in the effective particle diameter (D_{eff}) from 10 to 60 μm, and

Table 3.1 Spectral bands in the RRTMG and Fu-Liou RTMs.

RRTMG				Fu-Liou			
SW		LW		SW		LW	
Band	Unit: μm	Band	Unit: cm^{-1}	Band	Unit: μm	Band	Unit: cm^{-1}
16	3.08-3.85	1	10-350	1	0.2-0.7	1	0-280
17	2.5-3.08	2	350-500	2	0.7-1.3	2	280-400
18	2.15-2.5	3	500-630	3	1.3-1.9	3	400-540
19	1.94-2.15	4	630-700	4	1.9-2.5	4	540-670
20	1.63-1.94	5	700-820	5	2.5-3.5	5	670-800
21	1.3-1.63	6	820-980	6	3.5-4.0	6	800-980
22	1.24-1.3	7	980-1080			7	980-1100
23	0.78-1.24	8	1080-1180			8	1100-1250
24	0.63-0.78	9	1180-1390			9	1250-1400
25	0.44-0.63	10	1390-1480			10	1400-1700
26	0.34-0.44	11	1480-1800			11	1700-1900
27	0.26-0.34	12	1800-2080			12	1900-2200
28	0.2-0.26	13	2080-2250				
29	3.85-12.2	14	2250-2380				
		15	2380-2600				
		16	2600-3250				
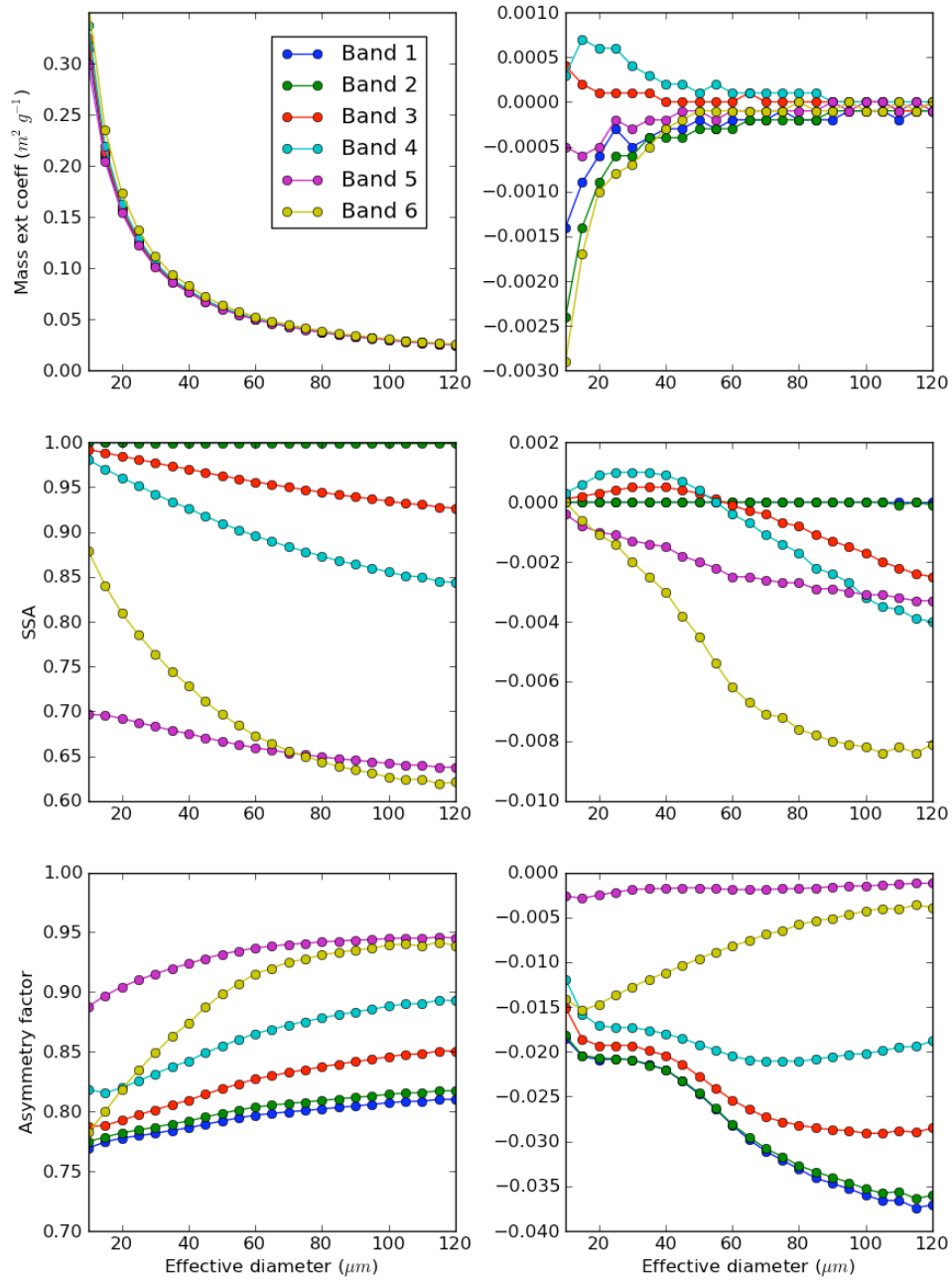
Fig. 3.1 Mass extinction coefficient (top panels), single-scattering albedo (middle panels), and asymmetry factor (bottom panels) as a function of effective diameter for the Fu-Liou model solar bands for severely roughened ice particles (left column). The right column shows the corresponding differences between the severely roughened and the smooth ice particles. The six bands shown correspond to the Fu-Liou RTM SW bands in Table 3.1.

remains under 0.05 m^2g^{-1} for large ice particles. The various bands of both RTMs differ little with regard to the mass extinction coefficient of SR particles. As the central wavelength of the spectral band increases, the single-scattering albedo gradually decreases from 1 to smaller values, and thus becomes more sensitive to D_{eff}. The bands with shorter wavelengths have smaller asymmetry factors compared with those with longer wavelengths. Not surprisingly, there exist minimal differences between the SR and CS values for the mass extinction coefficient and the single-scattering albedo, while the asymmetry factor shows a much larger affect from roughening. Moreover, the SR ice particles have consistently lower asymmetry factors than the CS particles for the same D_{eff}. The differences between the SR and the CS cases generally increase with D_{eff} with the exception of bands 5 and 6. Compared with the near-IR bands, the shorter wavelength bands (bands 1–4) show much larger differences in asymmetry factor between the SR and CS cases. This is consistent with previous studies showing that the effect of ice particle surface roughness is mostly realized as a reduction in the asymmetry factor, i.e. the CS particles scatter more in the forward direction than the SR particles. For the mass extinction coefficient, bands 2 and 6 exhibit the largest SR-CS difference when D_{eff} is small. Band 6 also exhibits the largest SR-CS difference in the single-scattering albedo when D_{eff} is large.

A test case is designed to illustrate the sensitivity of cloud radiative effect to ice particle surface roughness in the two RTMs using a common standard mid-latitude summer atmospheric profile for clear and cloudy sky simulations. The cloud radiative effect (CRE) is defined as the difference in the net (SW, LW, and total=SW+LW) flux at

50

the top of the atmosphere (TOA) and surface (SFC) between the cloudy sky and the clear

sky:

$$CRF = F_{all\ sky} - F_{clear} = N(F_{cloudy} - F_{clear}),\qquad(3.7)$$

$$F_{all\ sky} = N * F_{cloudy} + (1 - N) * F_{clear},\qquad(3.8)$$

where F_{cloudy} and F_{clear} are the net fluxes (downward minus upward) for cloudy

(overcast) sky and clear sky, respectively. N is cloud fraction, assumed to be 1 here. For

this test case, an ice cloud layer is located between 12-13 km, the solar zenith angle is set

to 60°, and the surface is assumed to be black for both the SW and LW, i.e., surface

albedo and emissivity are zero and one respectively at all wavelengths. The CRE is

calculated for SR and CS cases with both the Fu-Liou and RRTMG RTMs as the ice

cloud optical thickness ranges from 0.01 to 100 and the D_{eff} ranges from 10 to 120 μm.

Fig. 3.2 shows an example of simulated CRE at the TOA and SFC from the Fu-Liou

RTM as a function of D_{eff} and the ice cloud optical thickness using the SR ice particle

model. Similar results were obtained for RRTMG but are not shown here. The CRE is

highly sensitive to the changes in ice cloud optical thickness, while the dependence on

D_{eff} is weak. These results are in agreement with the study by Hong et al. (2009).

The simulated ice particle surface roughness effect on CRE (i.e., the difference

between the SR and CS CRE) for the Fu-Liou and RRTMG RTMs is shown in Figs. 3.3

and 3.4, respectively. The Fu-Liou and RRTMG results share many common features.

First, both RTMs show substantial and dominant roughness effects in the SW, while

minimal influence in the LW. Second, the most pronounced roughness effects occur
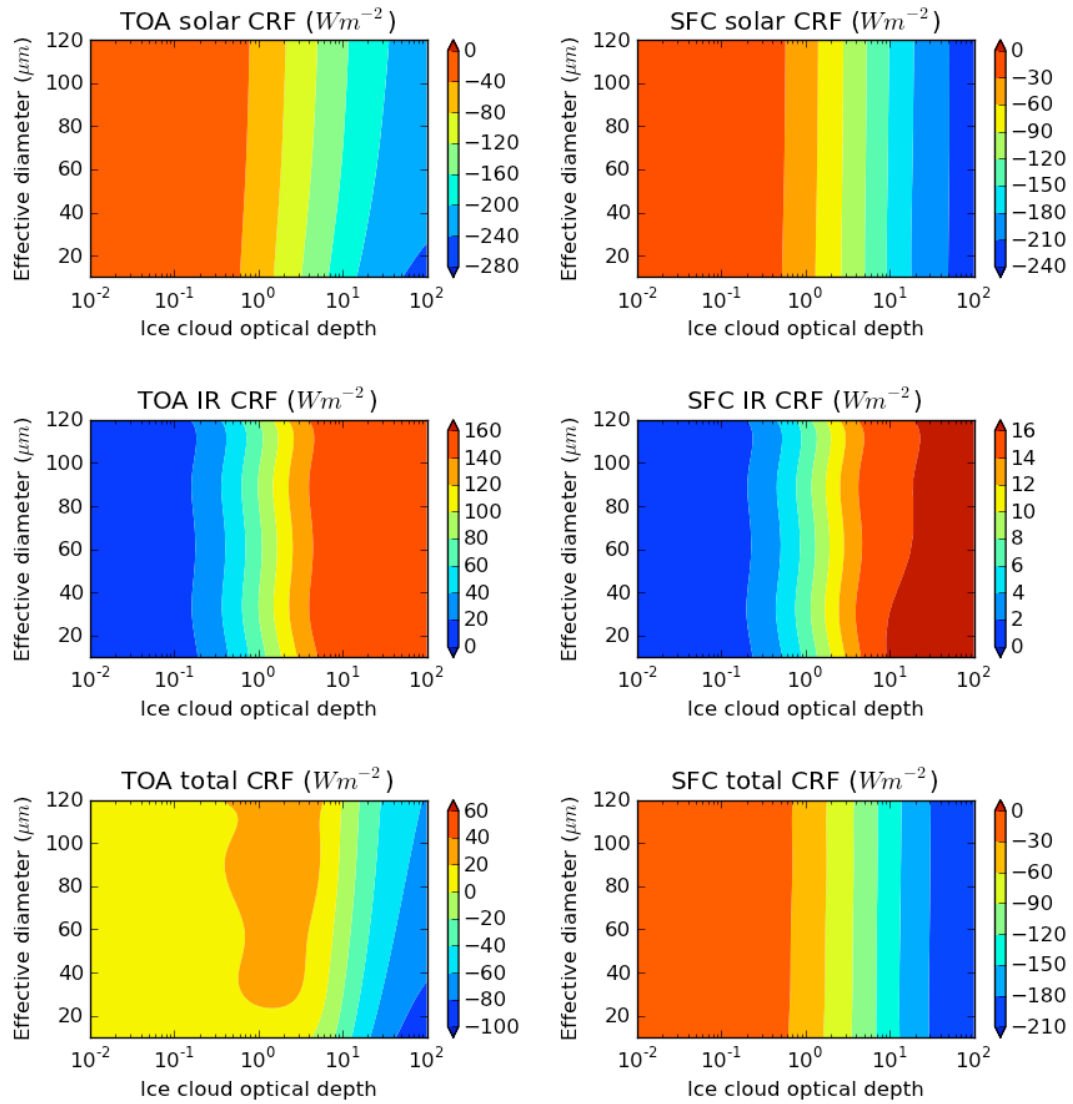
Fig. 3.2 CRE at SZA=60° as a function of ice effective diameter and cloud optical depth as simulated by the Fu-Liou RTM for severely roughened (SR) ice particles. Left columns are for the TOA and right columns for the SFC. Top panels are for SW, middle panels for LW; and bottom panels are for the total (SW+LW) CRE.
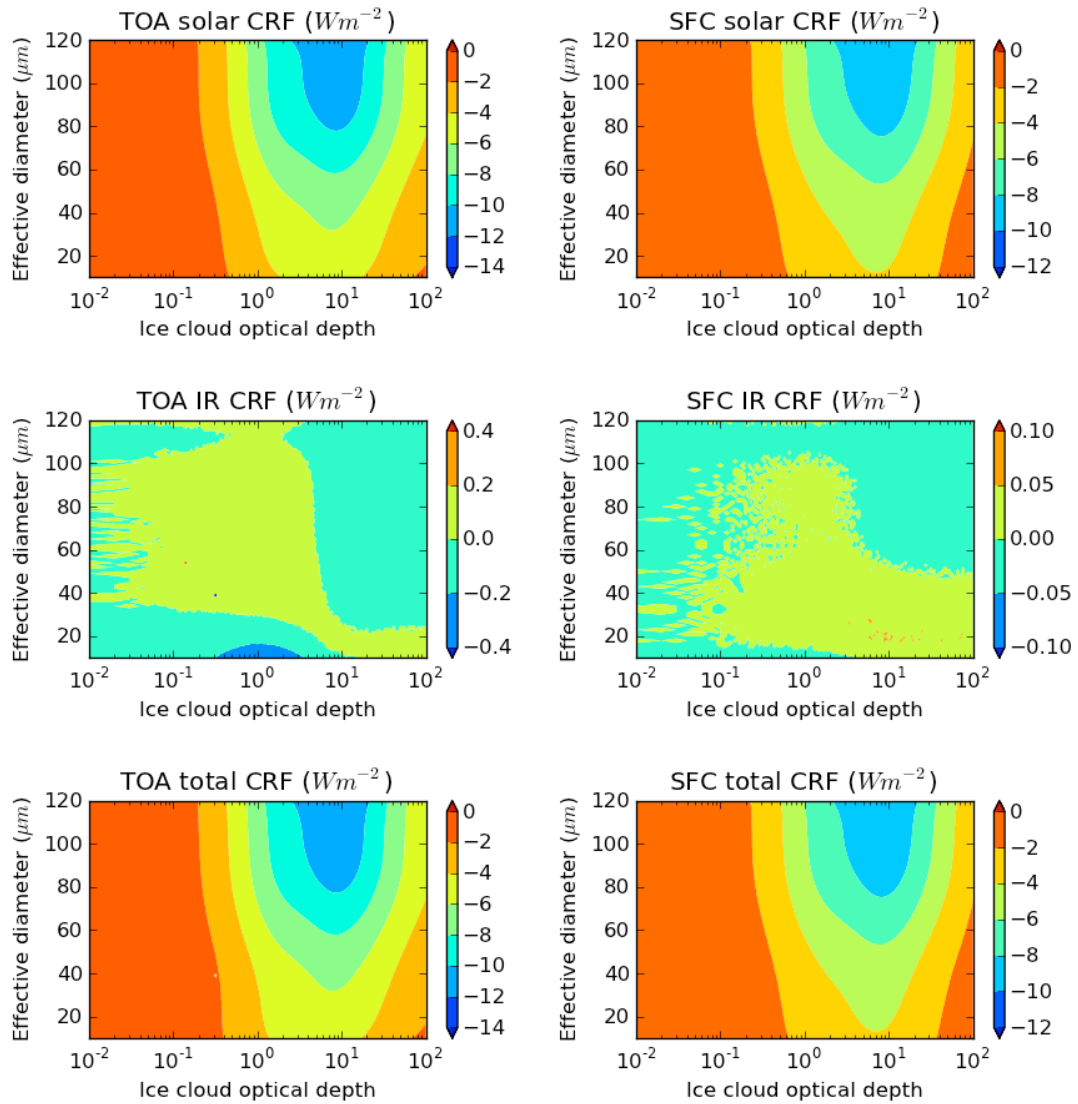
Fig. 3.3 Ice particle surface roughness effect on CRE at SZA=60° as a function of ice particle effective diameter and cloud optical depth for the Fu-Liou RTM. Left columns are for the TOA, and right columns for the SFC. Top panels are for SW, middle panels for LW, and the bottom panels for the total (SW+LW) CRE.
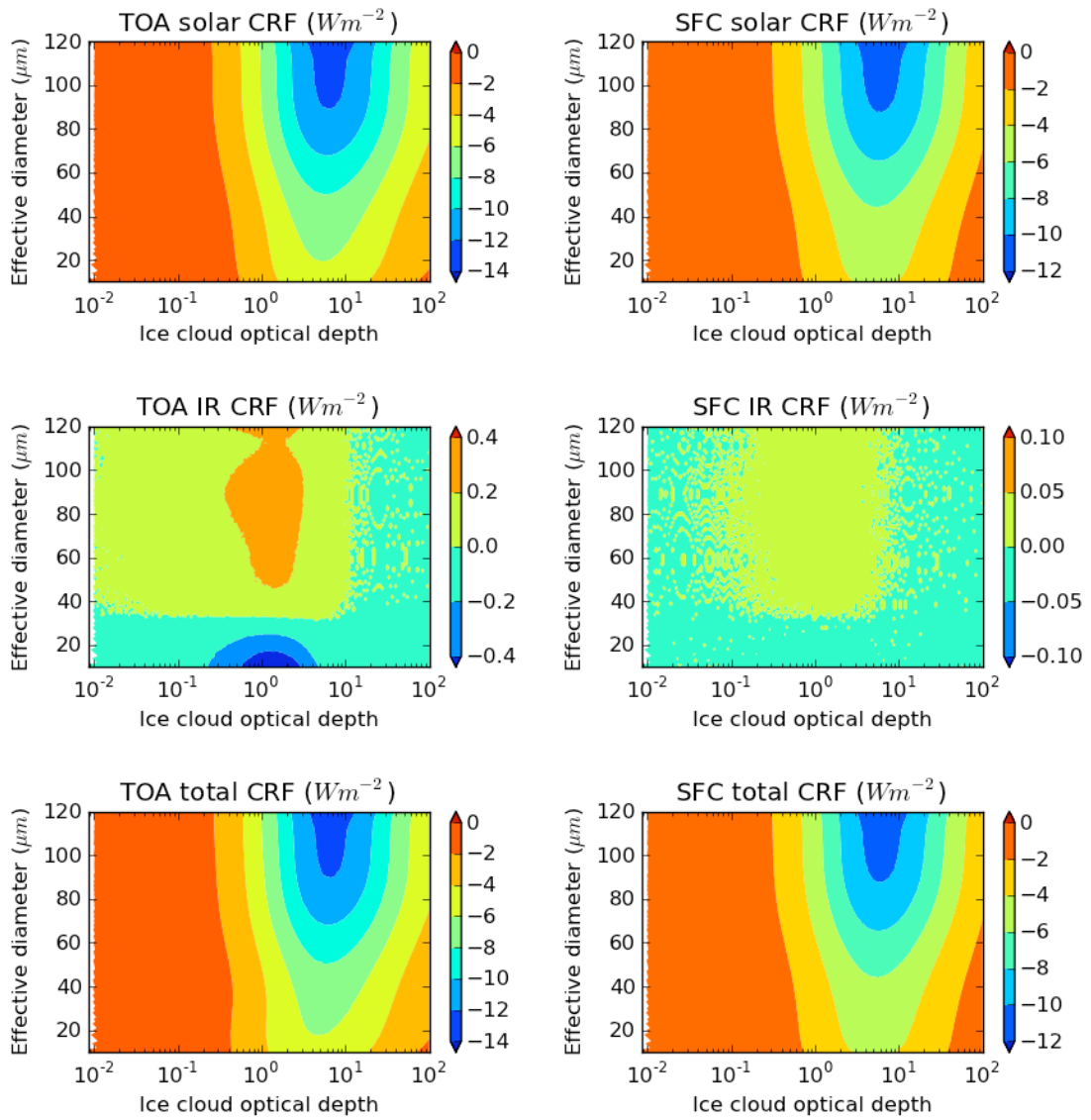
Fig. 3.4 As in Fig. 3.3, but for the RRTMG RTM.

when the optical thickness ranges between 3 and 12 for all values of the D_{eff}. Beyond this higher value of the optical thickness, the roughness effect decreases for a given particle size. Third, the patterns of the roughness–induced CRE variation with D_{eff} and optical thickness from the two RTMs are quite similar. However, the Fu-Liou RTM tends to have lower roughness–induced SW CRE by around 2 Wm^{-2}. Moreover, for RRTMG the highest value of the roughness–induced CRE center is skewed toward a smaller ice optical thickness than for the Fu-Liou RTM. These differences could be due to the different band structures of the two RTMs.

3.3.2 AGCM modeling results

We now examine the influence of particle roughness on the CRE in the CAM5.1 AGCM. Use of an AGCM in this analysis demonstrates the impact of surface roughness for a broad range of atmospheric profiles that occur through the interaction of the RTM in the AGCM with other model components. More importantly, the AGCM model has the potential to illustrate the dynamical/thermodynamical feedbacks that result from changing only the ice cloud bulk scattering properties. We replace the default ice cloud scattering properties in the version of RRTMG used in the CAM5.1 model with our new CS and SR parameterizations. The CAM5.1 model is run for ten years at 1.9°x2.5° horizontal resolution and with 31 vertical levels. The model is forced with cyclic observed sea surface temperature climatology and greenhouse gases to minimize the influence of changing surface and atmospheric conditions and mitigate the influence of

any particular weather events in a given year. The results of cloud radiative effect climatology are derived from the 10-year run.

The optical properties of the new SR and CS ice particle models are compared with those of the default CAM5 (Mitchell et al. 1996; Mitchell et al. 2006) in Fig. 3.5. We find considerable differences between the three cases. The differences between the CAM5 default scheme and our parameterizations are probably not only due to ice particle surface roughness, but due to other factors as well, e.g., ice particle habits and size distributions assumed in generating the bulk scattering properties. The asymmetry factor shows the largest differences; both the new CS or SR models display substantial differences from the default model currently adopted in CAM5.1. The single-scattering albedo of the near–IR bands tends to decrease for larger effective diameters.

Fig. 3.6 shows the CAM5.1 simulated ten-year mean annual total cloud radiative effect as well as the surface roughness effect (again, the difference between the SR and CS cases) on total cloud radiative effect at the TOA. Only the results that are significant at a 95% confidence level are shown for the difference plots. Total cloud radiative effect is shown because the CAM5.1 radiation scheme does not treat different cloud types individually, thus making it impossible to single out the effect of ice clouds. Table 3.2 summarizes the annual global averaged SW/LW/NET cloud radiative effect and the roughness effect. A difference of -1.46 Wm^{-2} is derived in the net cloud radiative effect due to the roughening of ice particles. This is a sizeable value that approaches the magnitude of forcing caused by various scenarios of increased CO_2 concentrations.

56
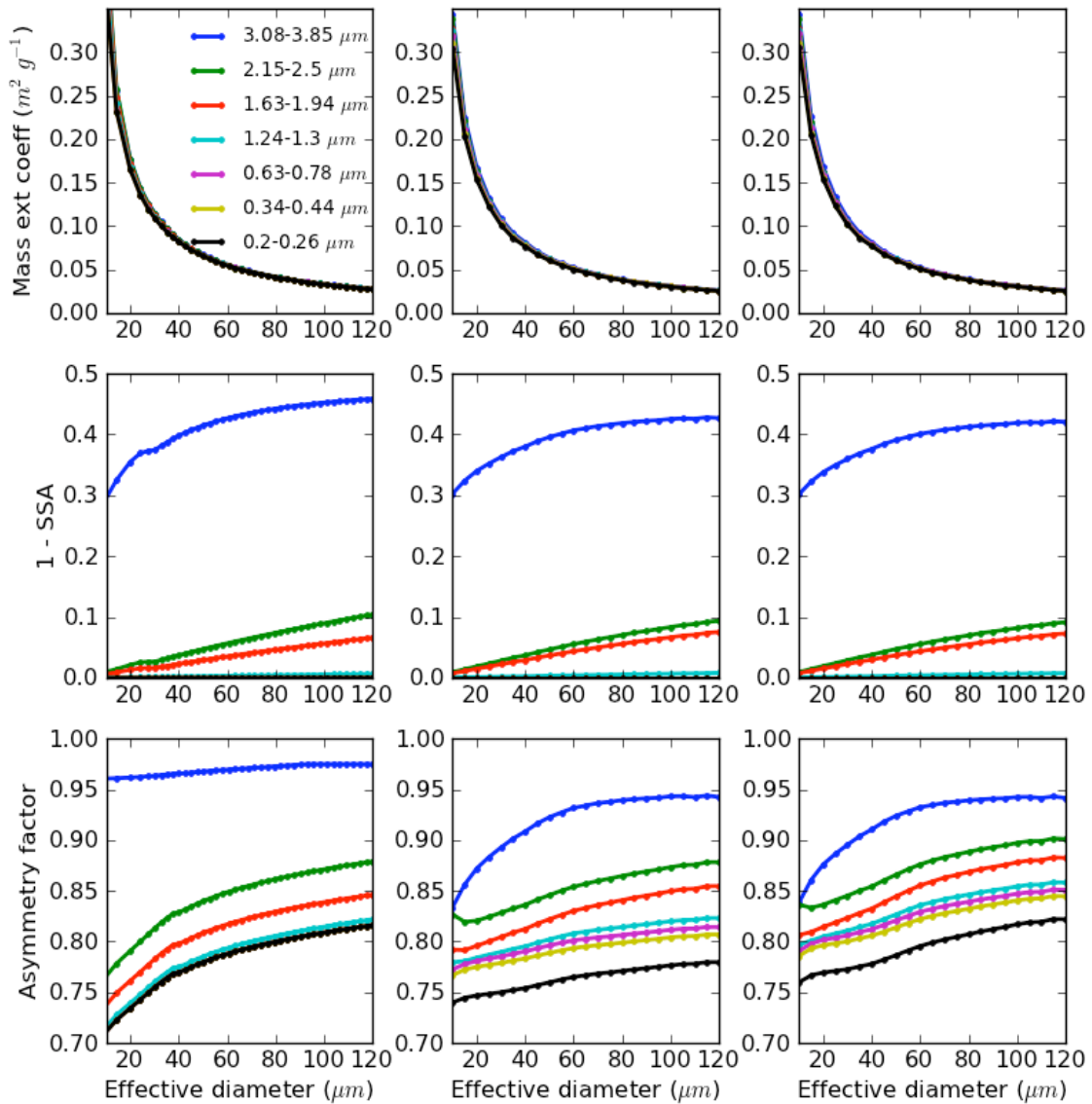
Fig. 3.5 Mass extinction coefficient (top panels), single-scattering albedo (middle panels), and asymmetry factor (bottom panels) as a function of ice particle effective diameter for selected bands in the RRTMG code for the default CAM5 option (left column), the severely roughened ice particle model (middle column) and the completely smooth ice particle model (right column).
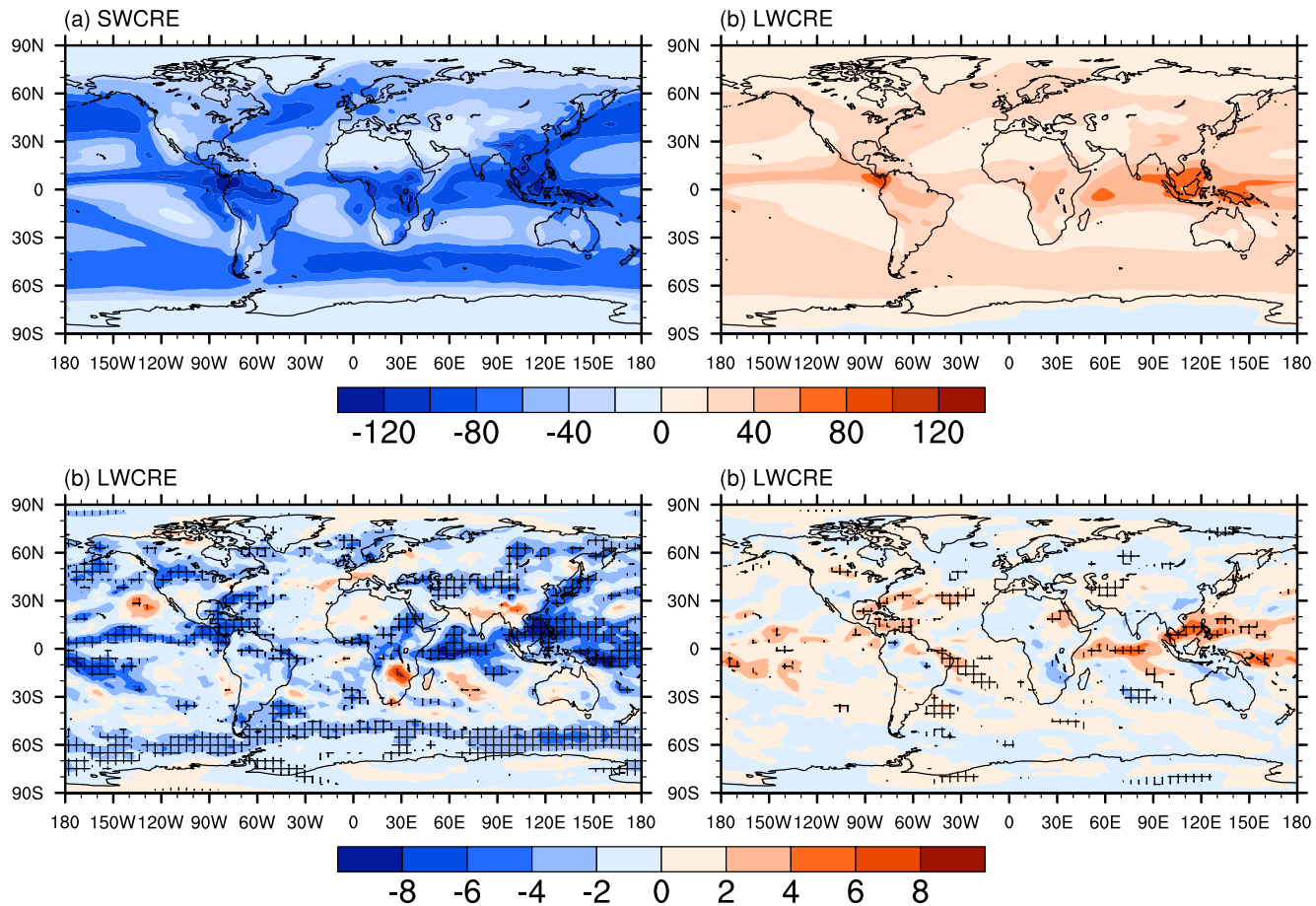
Fig. 3.6 CAM5.1 simulated ten-year mean annual total cloud radiative effect (units: W m^{-2}) and the roughening effects (CRE for the severely roughened case minus that of the smooth case) at the TOA: (a) Shortwave cloud radiative effect; (b) Longwave cloud radiative effect; (c) Ice roughening effect on shortwave cloud radiative effect; (d) Ice roughening effect on longwave cloud radiative effect. Only results with a 95% significance level are shown for the difference plots.

Results from the 10-year run also indicate that the spatial and seasonal variations of surface roughness induced SW cloud radiative effect are substantial. Zonal averages (Fig. 3.7) show that strong SW surface roughness effects are found in the tropics and in both hemisphere storm track regions (Fig. 3.6). The LW differences are limited mostly to the tropics. March has the largest SW (-2.35 Wm^{-2}) and LW (0.67 Wm^{-2}) particle roughness effects (Fig. 3.8). The simulated TOA LW CRE shows weaker seasonal variations, with a global averaged value of around 25 Wm^{-2} for all seasons.

Table 3.2 Global annual mean of the SR and CS total cloud radiative effect as well as the roughness effect (SR minus CS) (Unit: Wm^{-2}).

	SR	CS	SR-CS
SW CRE	-55.67	-53.84	-1.83
LW CRE	25.34	24.97	0.37
NET CRE	-30.33	-28.87	-1.46
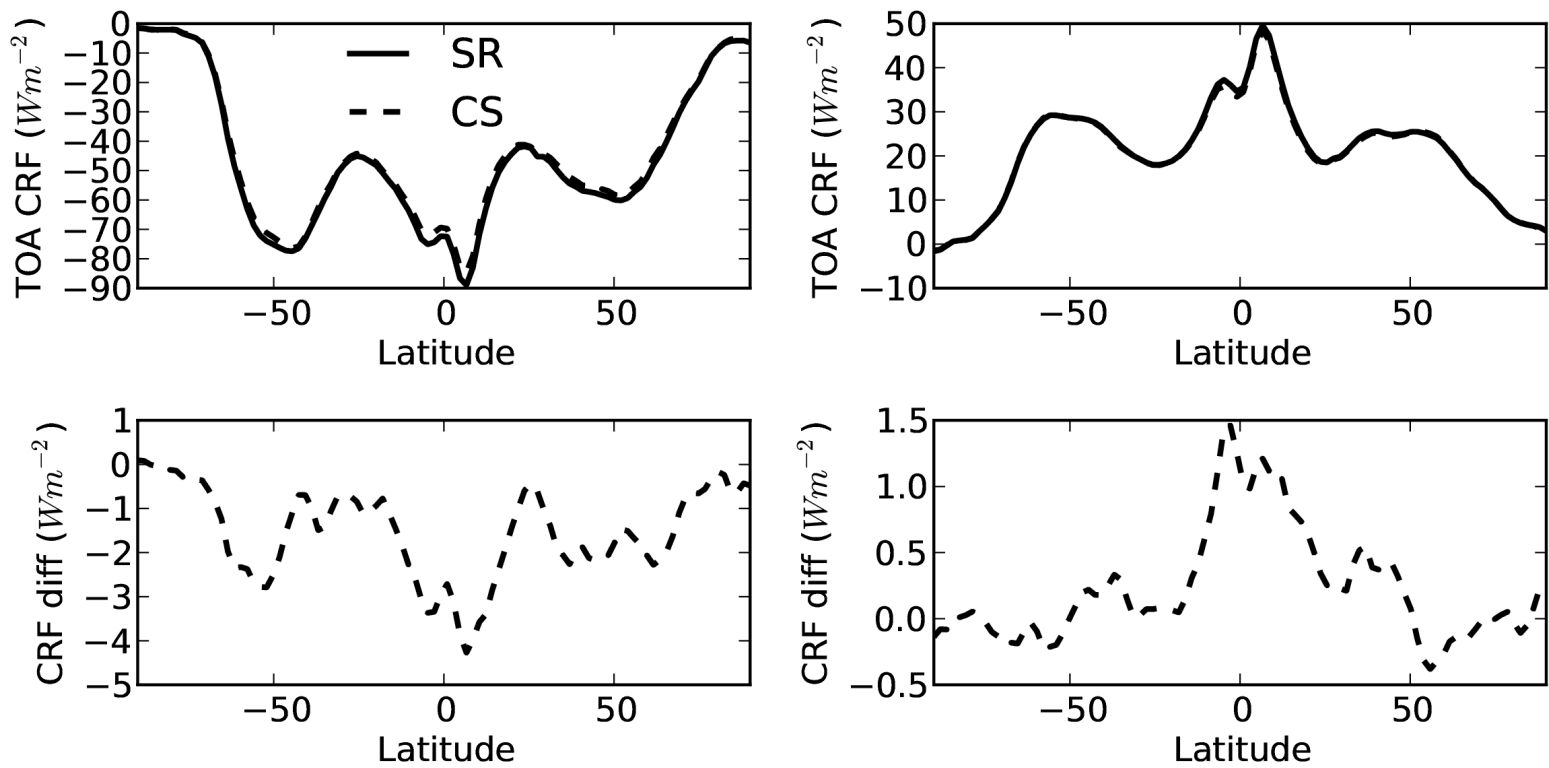
Fig. 3.7 The zonal averages of TOA SW and LW total CRE (upper left and right panels) and the ice particle surface roughness effects (lower left and right panels) (units: Wm^{-2}) as simulated by CAM 5.1.
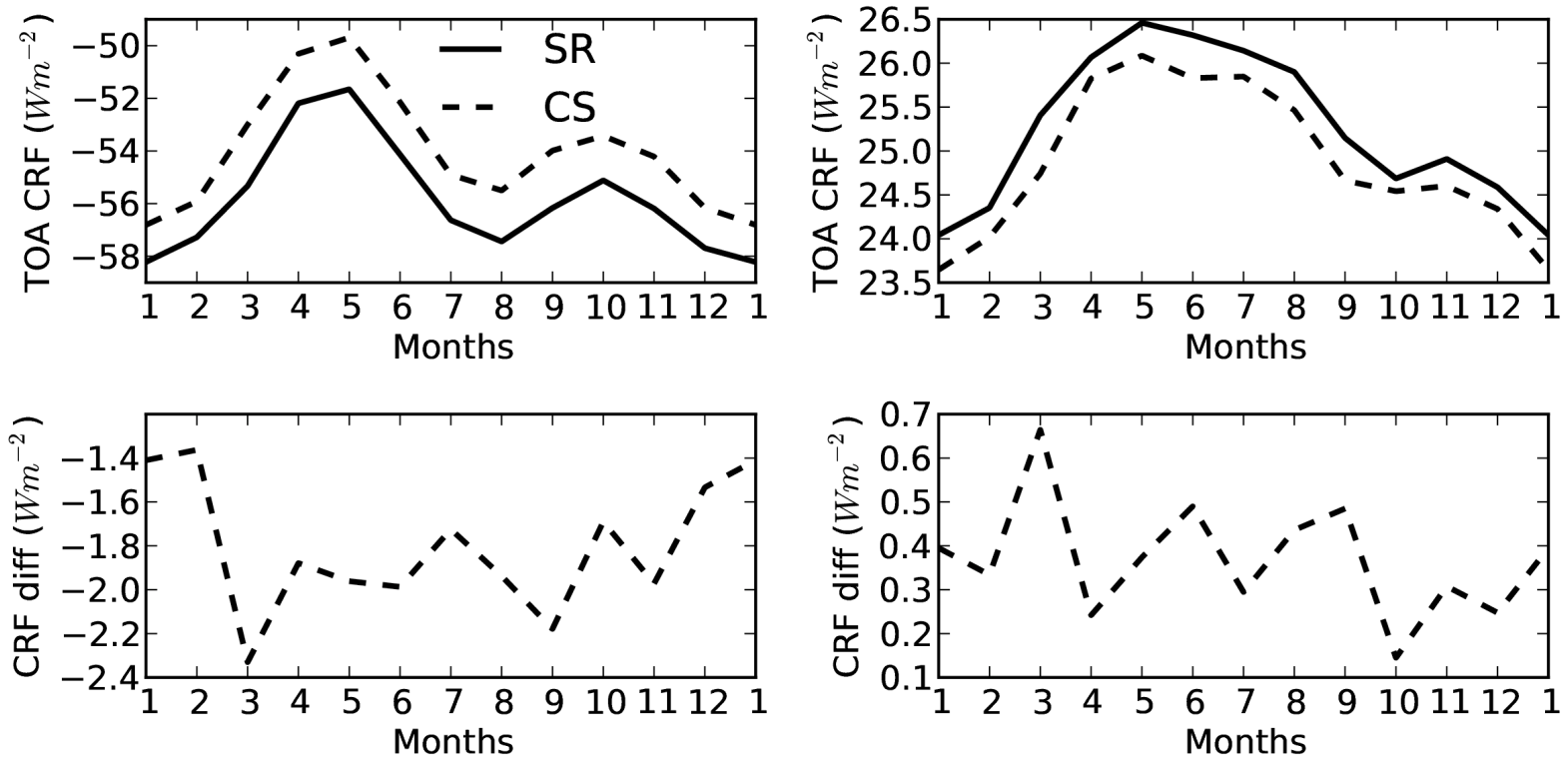
Fig. 3.8 The annual cycle of TOA SW and LW (upper left and right panels) total CRE and the ice particle surface roughness effects (lower left and right panels) (units: Wm^{-2}) as simulated by CAM 5.1.

The single column RTM simulations shown earlier suggest that roughness has a minimal effect on LW CRE. The CAM5.1 simulations however suggest some prominent LW effects in the tropics. This may be indicative of either feedback processes or internal variability in the AGCM that warrant further exploration. Perhaps the perturbation to the SW radiation by ice particle roughening induces changes in regional thermodynamic structure that subsequently lead to persistent local circulation anomalies. In turn, these circulation changes could lead to further changes in the ice cloud properties and thus, notable LW CRE changes. This suggestion is supported by the fact that surface roughness leads to both positive and negative anomalies in SW CRE in the model (Fig. 3.6) despite a prominence of SW CRE reduction in the single-column calculations (Fig. 3.3). On a global scale, the roughness effects are smaller but not negligible suggesting that these feedbacks retain some influence on global LW CRE.

In summary, the CAM5.1 AGCM simulation results seem to agree in general with the off-line RTM simulation results, but are more variable in both sign and magnitude and change with time and geographical locations, indicating potential feedback effects. The CAM5.1 results also provides a way of estimating the effects of ice particle surface roughening on CRE on a global scale, where the global annual average effects on SW and LW CRE are -1.83 Wm^{-2} and 0.37 Wm^{-2} (Table 3.2), respectively.

3.4 Conclusions

While there is an increasing awareness of the existence of ice particle surface roughness, few if any studies are available that provide an in-depth analysis of its influence on cloud radiative effect. This paper attempts to provide such a systematic analysis, with new band model parameterizations developed using a new database of ice particle single-scattering properties from the ultraviolet to the far infrared. The new parameterizations employ a set of comprehensive microphysical observations from field campaigns conducted around the world, and adopt ice cloud particle habits similar to those implemented in satellite remote sensing studies. The new band parameterizations are derived assuming that all ice particles are either severely roughened (SR) or completely smooth (CS). The CS and SR parameterizations are integrated into the Fu-Liou and RRTMG radiative transfer codes, and the NCAR Community Atmosphere Model (CAM, version 5.1) which uses a version of the latter algorithm.

The mass extinction coefficient and single-scattering albedo, are found to be quite similar between the CS and SR ice crystal models. The primary effect of ice particle surface roughness is in the reduction of the asymmetry factor for rough particles compared with smooth particles of the same size, a reduction that increases with increasing effective diameter D_{eff}. Thus, consideration of the particle surface roughness effect tends to result in decreasing the inferred particle size. Both the uncertainties associated with ice particle size distributions and surface roughness conditions should be considered.

The simulated cloud radiative effect (CRE) is highly sensitive to the variation of ice cloud optical thickness, whereas it is only weakly dependent on D_{eff}. The same is true for the effect of roughness on CRE. The effect of surface roughness in the shortwave (SW) spectrum dwarfs that for the longwave (LW) spectrum. Particle roughness has the most influence (more than 10 Wm^{-2} at SZA=60°) for cases with $D_{eff} \geq 80$ μm and where optical thickness ranges between 3 and 12. There are differences between the Fu-Liou and RRTMG RTM results at various D_{eff} and optical thicknesses that might be due to the different spectral bands used in each RTM code.

The AGCM simulations offer a more complete picture of the surface roughness effect on CRE than the RTM results because they provide spatial/seasonal variations and model feedbacks. For example, while the SW cloud radiative effect induced by particle roughness is still large and dominant, the LW forcing in the Tropics is larger than expected from the column RTM simulations. The apparent LW radiative effect by particle roughening in the AGCM simulation may be the outcome of thermodynamic feedbacks that modify cloud properties. This is supported by the fact both that positive and negative roughening effects on SW CRE occur in the model; we will investigate this more fully in future work. The global averaged response due to the adoption of severe particle roughening is estimated to be on the order of 1-2 Wm^{-2} for the SW spectrum, but much smaller in the LW. Since the global seasonal cloud radiative effect variation is no more than 7 Wm^{-2}, the contribution from the treatment of ice particle surface roughness is important. A difference of -1.46 Wm^{-2} in the net cloud radiative effect due to the roughening of ice particles is small but is similar in magnitude to the forcing of

greenhouse gases under various plausible scenarios. Additional observational and numerical studies (e.g., with other GCMs) are required to shed more light about the importance of crystal roughness on the global radiation budget.

CHAPTER IV

SIMULATION OF THE GLOBAL CONTRAIL RADIATIVE FORCING: A

SENSITIVITY ANALYSIS[*]

4.1 Introduction

Contrails are ice clouds produced by aircraft emissions under suitable atmospheric conditions and have optical and radiative properties similar to those of natural cirrus clouds (Penner et al. 1999). Young contrails are normally line-shaped and short-lived, but can persist for a longer amount of time and grow to transform into old contrail cirrus clouds indistinguishable from natural cirrus (Minnis et al. 1998). Contrails have drawn considerable attention in research studies on aviation-climate interactions, because contrail forcing has been found to outweigh the impact of direct aircraft CO_2 emissions and is regarded as the most significant effect of aviation on climate (Burkhardt and Karcher 2011; Sausen et al. 2005). Furthermore, the question arises whether the radiative effect of contrails may be responsible for considerable diurnal temperature variations in some regional areas where air traffic activities are significant (Hong et al. 2008; Travis et al. 2002).

Although contrail detection from satellite observations (Iwabuchi et al. 2012; Minnis et al. 2005) is possible, the direct assessment of contrail radiative forcing from a satellite observational perspective (Meyer et al. 2002) remains a challenge. Under these

---

[*] Part of this chapter is reprinted with permission from "Simulation of the global contrail radiative forcing: A sensitivity analysis" by Yi, B., P. Yang, K.-N. Liou, P. Minnis, and J. E. Penner, 2012. *Geophysical Research Letters*, 39, 24, Copyright 2012 by John Wiley and Sons.

circumstances, simulations based on numerical models of various complexities ranging from simple offline radiative transfer models to sophisticated online global climate models, have been employed for the estimation of contrail radiative forcing. For example, Minnis et al. (1999) used the Fu-Liou radiative transfer model together with prescribed contrail properties (coverage, optical depth, particle size, etc.) and computed the global mean radiative forcing for line-shaped contrails to be approximately 20 mW m^{-2} in 1992 and estimated to be 100 mW m^{-2} in 2050. However, many global climate model studies focus on parameterizing contrail formation, evolution, transformation, and dissipation processes by using aircraft emission inventory data. Ponater et al. (2002) developed the first line-shaped contrail parameterization for use in the ECHAM4 general circulation model and found substantially smaller contrail radiative forcing. Burkhardt and Karcher (2009) implemented a physical process-based prognostic contrail parameterization scheme and included the consideration of aged contrail cirrus in the GCM. Rap et al. (2010a, 2010b) adapted Ponater et al.'s (2002) contrail parameterization scheme, applied it to the UK Met Office climate model, and derived the 2002 annual global averaged contrail coverage and optical depth to be 0.11% and 0.2 with an estimated global mean annual contrail forcing of approximately 7.7 mW m^{-2} at the top of the atmosphere. Chen et al. (2012) incorporated 2006 aircraft emissions into the NCAR CESM model and compared the results with MODIS observations.

In the latest IPCC AR4 report (Forster et al. 2007), contrail radiative forcing is classified as one of the problems with low scientific understanding. The best estimate of 10 mW m^{-2} for persistent linear contrail radiative forcing in the year 2005 contains a

large uncertainty range. The large uncertainty comes from various aspects: model deficiencies; contrail spatial distribution (coverage, optical depth, and vertical distribution); contrail size and optical properties; cloud overlap assumptions; etc. While some of the factors have been explored by previous studies (Fromming et al. 2011; Marquart and Mayer 2002; Rap et al. 2010b), the uncertainties must be estimated within a comprehensive framework. This work aims to provide a consistent comparison of the potential factors influencing the forcing and to explore the largest uncertainties. The data, models and the simulation setup are presented in Section 4.2. Section 4.3 contains the results and discussion, and the main conclusions are summarized in Section 4.4.

4.2 Data, models and simulation

4.2.1 Offline simulation

We employ an offline simulation approach to calculate the contrail radiative forcing. Albeit great advances have been made in online approaches, the offline approach has the advantage of easier understanding of different sensitivity studies. For the year 2006, we use the Community Atmospheric Model version 5 (CAM5) (Neale et al. 2010) as the host model to provide daily atmospheric profiles and natural cloud spatial distributions in the all-sky case. The CAM5 model is driven by observed sea surface temperatures and is run at the default settings with 31 vertical levels at a 1.9°x2.5° horizontal resolution. The radiative transfer code used for the radiative flux and forcing calculation is the RRTM Model for GCMs (RRTMG) (Iacono et al. 2008) for shortwave and longwave spectral bands. The RRTMG model allows for multiple

choices in the various settings, such as different cloud overlap assumptions and ice cloud optical properties parameterization schemes. Furthermore, for the sensitivity tests, we implement two new parameterization schemes for natural cirrus clouds and contrails into the RRTMG. Both parameterizations are based on an ice particle scattering properties database developed by Yang et al. (2012). The database contains spectrally consistent scattering, absorption, and polarization properties of atmospheric ice crystals at wavelengths from 0.2 μm to 100 μm. Natural cirrus cloud parameterization scheme uses the general ice habit mixture (Baum et al. 2011) as is described in Chapter III in this dissertation, while the contrail scheme employs an ice habit mixture constrained by satellite observations (Xie et al. 2012). They used manually detected contrails from MODIS brightness temperature difference and MODIS contrail mask detected by an automatic contrail detection algorithm and collocated MODIS and CALIOP data to infer the physical and optical properties of contrails. An algorithm was developed to determine the most appropriate ice particle shape distribution within contrails that can minimize the difference between the computed contrail depolarization ratios and the satellite measurements in the year 2006 and 2007. Combining the contrail ice particle shape model and the spectral scattering property database (Yang et al. 2013), parameterization schemes can be developed to represent contrail optical properties within any broadband radiative transfer models following the method discussed in section 3.2.3.
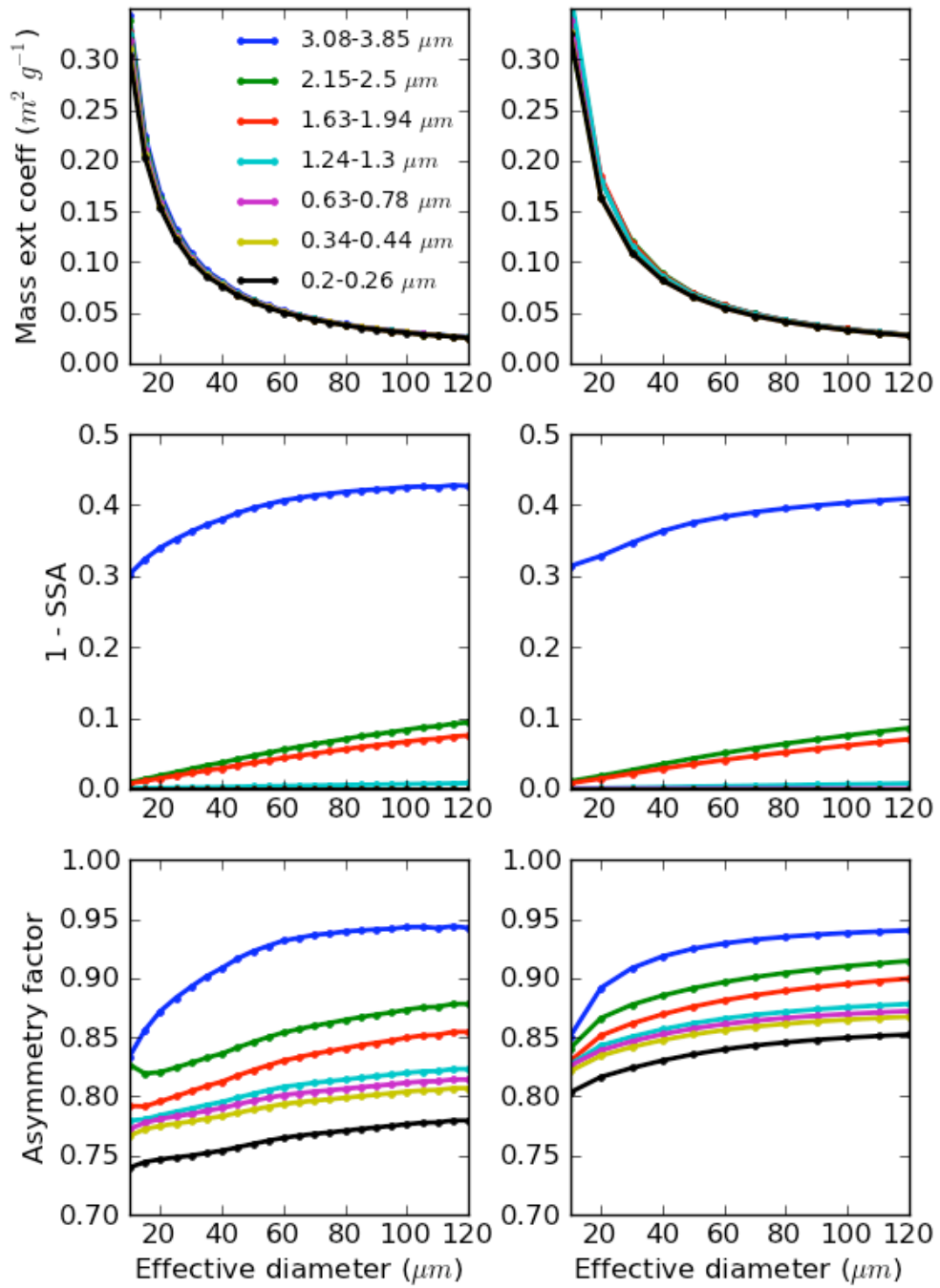
Fig. 4.1 Example of optical property parameterizations as functions of the effective diameter for natural cirrus (left column) and contrail (right column) in selected spectral bands of the RRTMG radiative transfer code.
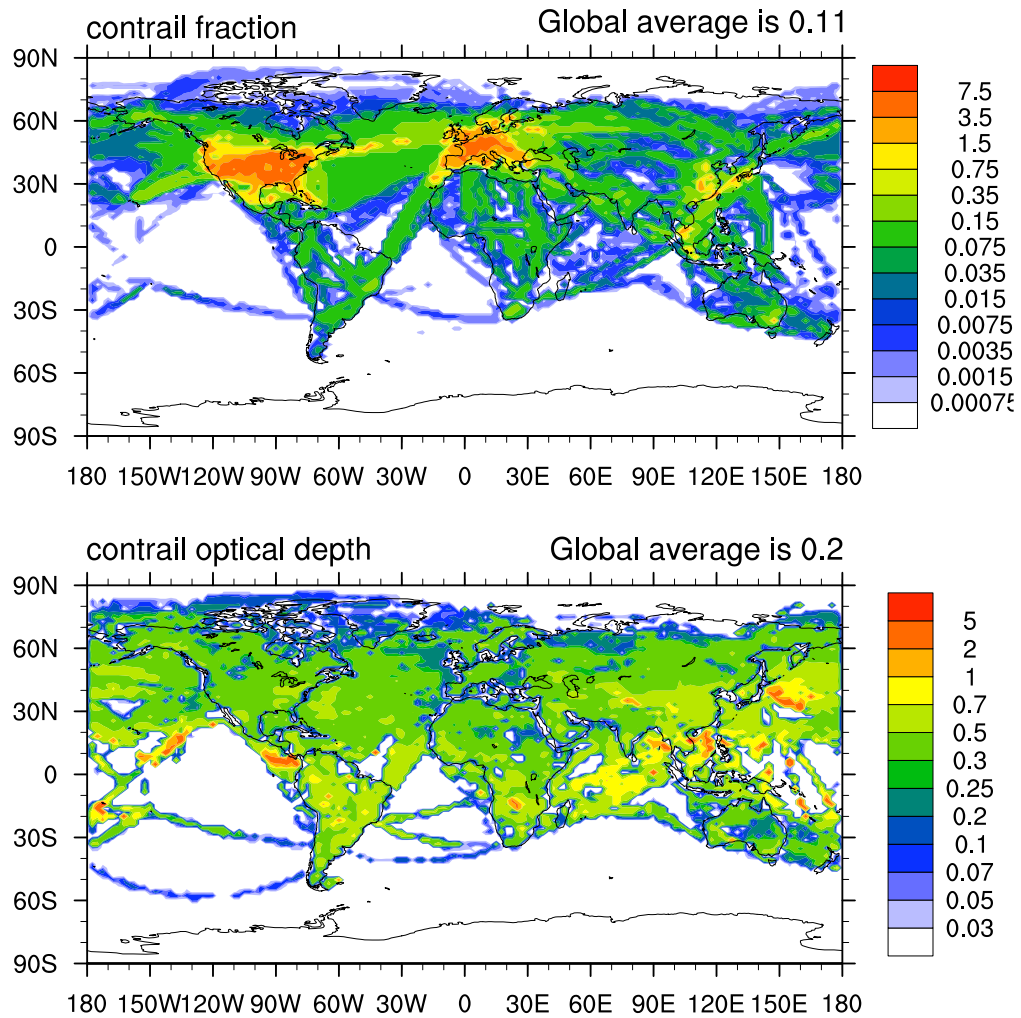
Fig. 4.2 Global annual averaged contrail coverage (upper panel, unit: percentage) and optical depth (lower panel, unit: 1) for 2002, following Rap et al. (2010b).

Fig. 4.1 is an example of natural cirrus and contrail optical property parameterization for selected spectral bands in the RRTMG model. The optical properties, including the mass extinction coefficient, single-scattering albedo, asymmetry factor, and mass absorption coefficient, are parameterized as functions of the particle effective diameter. The natural cirrus and contrail mass extinction coefficients and single-scattering albedos are quite similar, while the largest differences are seen in the asymmetry factors. Contrails tend to have larger asymmetry factors than natural cirrus in the solar to near IR bands. Both parameterizations yield optical properties that are more sensitive to particle sizes with effective diameters smaller than ~ 60 μm.

The contrail radiative forcing strongly depends on contrail coverage and optical depth. We prescribe the same spatial distribution used by Rap et al. (2010b) for the 2002 annual mean global linear contrail coverage and optical depth with respective values of 0.11% and 0.2 (Fig. 4.2). In the control run, we assume the contrail layer is located on the 17th vertical layer (approximately 9 km in height). In the contrail optical property parameterization, an assumed particle effective diameter of 23 μm together with the random cloud layer overlap assumption is used. We design and implement model runs to examine the sensitivity of contrail forcing to various factors and assumptions. Detailed descriptions of the sensitivity tests are illustrated in Table 4.1. In each case, one specific factor is varied while the other factors are kept constant. In the all-sky case, natural clouds are assumed to accompany the contrail layer in the same column, with the fraction of natural clouds determined by CAM5 model simulations.

Table 4.1 Description of the sensitivity test cases.

Case	Description
RNCO23	Using the random vertical cloud overlap assumption and contrail optical properties with a contrail effective diameter of 23 μm.
RNCO35	The same as RNCO23 case, except that a contrail effective diameter of 35 μm is used.
RNCI23	The same as RNCO23 case, except that new natural cirrus optical properties are used.
RNFU23	The same as RNCO23 case, except that the Fu parameterization scheme is used.
MRCO23	The same as RNCO23 case, except that the maximum-random vertical cloud overlap assumption is used.
RNCO23H	The same as RNCO23 case, except that the contrail layer is lifted 2 KM higher.
RNCO23OD	The same as RNCO23 case, except that 25% lower global averaged contrail optical depth is assumed.
RNCO23F	The same as RNCO23 case, except that 25% lower global averaged contrail coverage is assumed.
CRCO23	The same as RNCO23 case, except that clear-sky condition is used.

4.2.2 Online simulations

Online simulations refer to the kind of numerical simulations where contrails are completely included in the physical processes within GCM simulation. The major difference between offline and online simulations is that in the former radiative impacts induced by the contrails have no influences from the other model components, and have no feedbacks to the model simulation in the future time steps while the latter have. Since contrails are included in the simulation along with the other clouds, we don't need to run the radiation module separately again in the online modeling framework. Except for the above differences, the input information, such as contrail fraction, optical depth, height, effective size, etc, is prescribed and kept the same as those for the offline model.

4.3 Results and discussion

4.3.1 Results of offline simulation and sensitivity study

We define contrail radiative forcing as the difference in the SW/LW/NET radiative fluxes with and without contrails at the top of the atmosphere (TOA). In the control case shown in Fig. 4.3, the simulated 2006 global annual averaged shortwave, longwave, and net contrail radiative forcing values are -6.24 mW m^{-2}, 17.56 mW m^{-2}, and 11.32 mW m^{-2}, respectively. The net positive radiative forcing is in reasonable agreement with the best estimates from previous studies. The geographical distributions of SW, LW, and net contrail radiative forcings are most significant over continental North America, Europe, and East Asia, where the most intensive aviation activities
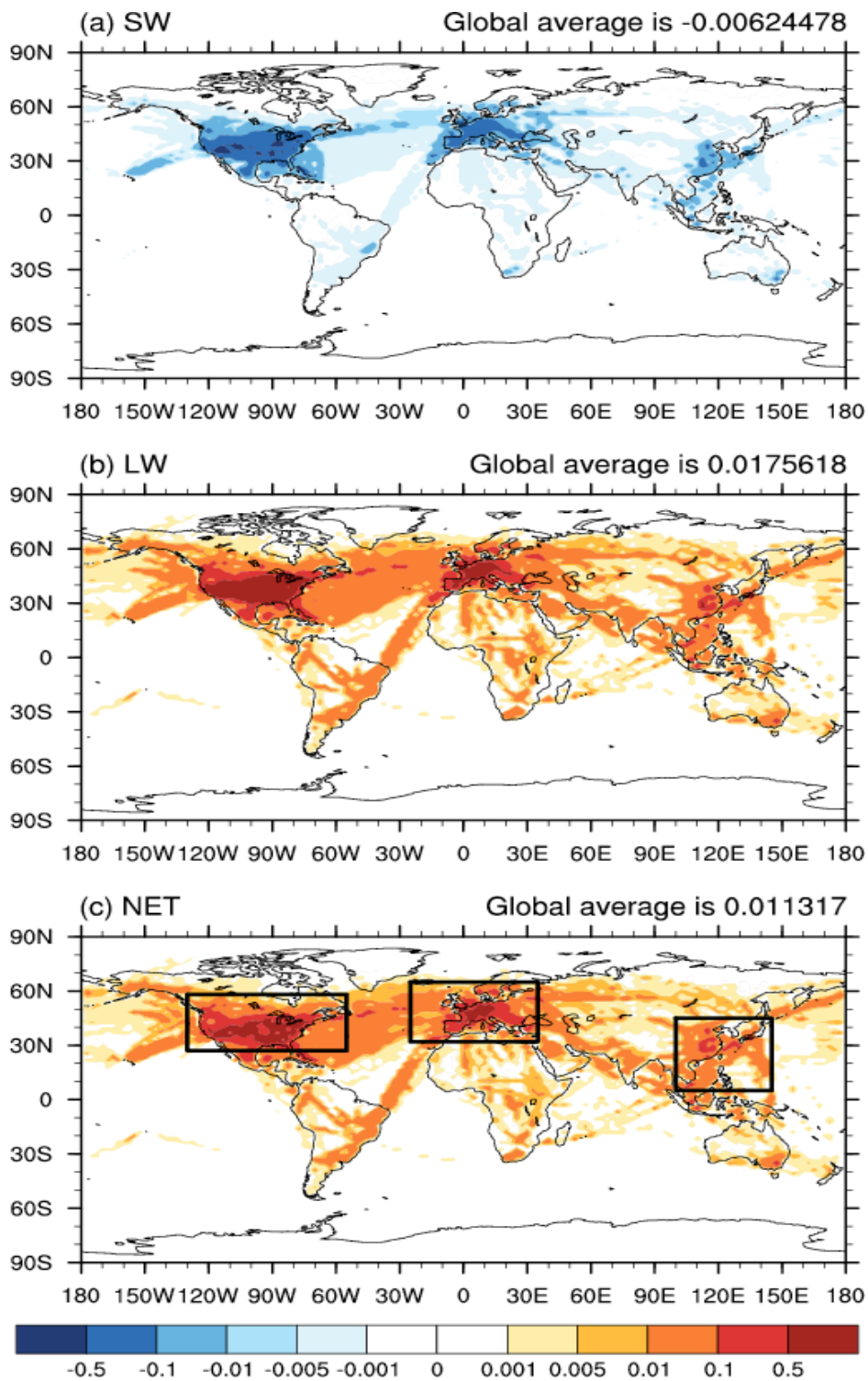
Fig. 4.3 Simulated 2006 global annual averaged shortwave (a), longwave (b), and net (c) contrail radiative forcing (W m^{-2}) in the control case.

occur. Dense inter-continental flight corridors contribute significantly to global contrail forcing. The resulting net radiative forcing generally follows the longwave distribution, which outweighs its shortwave counterpart by a factor of three. The zonal averaged contrail forcing (Fig. 4.4) indicates that contrail-induced radiative forcing peaks around 40° N latitude in the northern hemisphere where human aviation activities most frequently occur. Fig. 4.3c highlights three regional areas, and Table 4.2 summarizes the geographical areas and the SW, LW, and net averaged regional contrail forcing values within the three regions. The North American region is subjected to the largest averaged contrail forcing, more than ten times the global average. The regional average over Europe is slightly more than half of that over North America, whereas the East Asia region contribution is far smaller.

The primary results from the sensitivity test cases are summarized in Table 4.3, where the simulated global annual mean contrail radiative forcing for each case is compared with the control case (RNCO23). The percentages in parentheses indicate relative differences between perturbation and control cases. Contrail particle size, which varies with contrail age, background meteorology, and the specific aircraft emission, is the most uncertain variable. Moreover, the contrail particle size is a difficult parameter to be retrieved on the basis of remote sensing. The RNCO35 case tests the effect on contrail radiative forcing by assuming a contrail particle to have an effective diameter 1.5 times larger than the control case. The results indicate the net forcing to increase by nearly 46% due to the combined effect of a significant decrease in shortwave forcing (-54%) and an increase in longwave forcing (10%). The results not only show the

important role of contrail particle size information in the determination of contrail radiative effects, but also reveal the need for development of an accurate and reliable retrieval algorithm to determine contrail particle size by means of airborne and/or ground-based remote sensing.
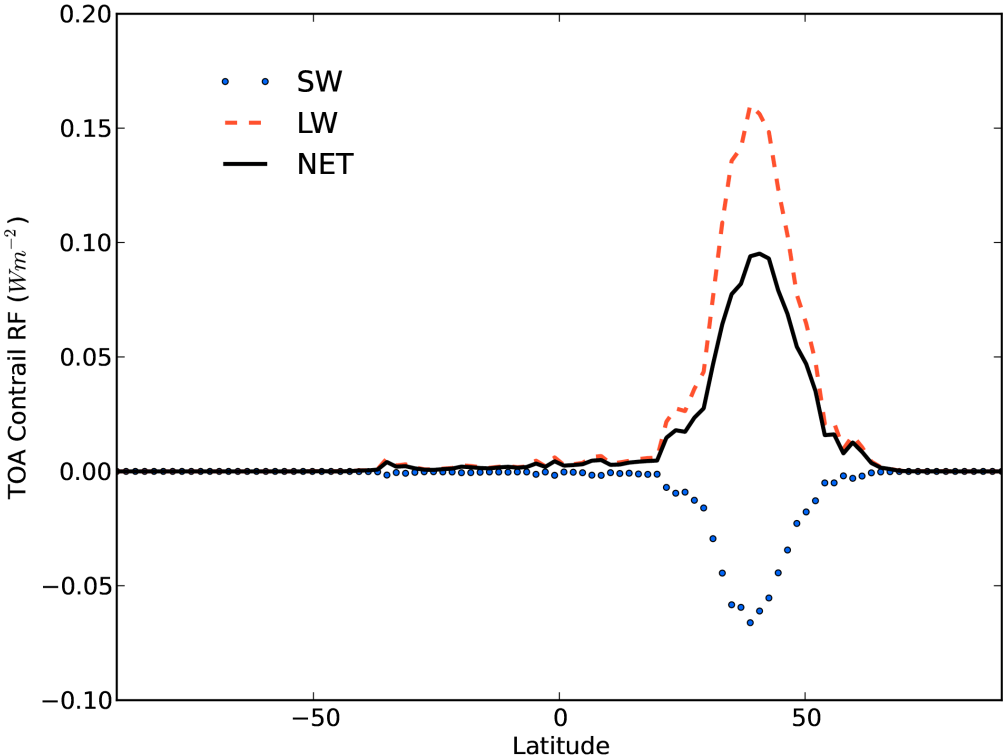
Fig. 4.4 Zonal averages of the 2006 annual averaged contrail SW, LW, and NET radiative forcing at the TOA.

Table 4.2 Regional contrail radiative forcing over air traffic intensive areas.

Region	North America	Europe	East Asia
Geographical area	27° – 58° N, -130° – -55° E	32° – 65° N, -25° – 35° E	5° – 45° N, 100° – 145° E
SW forcing (m Wm^{-2})	-105.9	-40.4	-10.7
LW forcing (m Wm^{-2})	260.8	126.2	35.7
NET forcing (m Wm^{-2})	154.9	85.8	25.0

Table 4.3 Global annual mean contrail radiative forcing for test cases.

Case	Radiative forcing (mW m^{-2})		
	SW	LW	NET
RNCO23	-6.24	17.56	11.32
RNCO35	-2.87 (-54.0%)	19.39 (10.4%)	16.52 (45.9%)
RNCI23	-7.52 (20.5%)	18.23 (3.8%)	10.71 (-5.4%)
RNFU23	-4.00 (-35.9%)	16.78 (-4.4%)	12.78 (12.9%)
MRCO23	-5.58 (-10.6%)	15.33 (-12.7%)	9.75 (-13.9%)
RNCO23H	-5.97 (-4.3%)	19.06 (8.5%)	13.09 (15.6%)
RNCO23OD	-2.42 (-61.2%)	13.57 (-22.7%)	11.15 (-1.5%)
RNCO23F	-2.30 (-63.1%)	13.03 (-25.8%)	10.73 (-5.2%)
CRCO23	-10.57 (69.4%)	22.72 (29.4%)	12.15 (7.3%)

Two cases are selected to test sensitivity to the optical property parameterization schemes: the current natural cirrus parameterization (RNCI23) and the natural ice cloud parameterization developed by Fu (1996) (RNFU23). We find the Fu parameterization scheme, which only considers smooth hexagonal ice crystals, to significantly affect shortwave radiative forcing and to contribute a 13% increase in net forcing in comparison to the control case. The RNCI23 case yields much closer results to the control case because both the natural cirrus and contrail cloud radiative property parameterizations take into consideration a mixture of various ice crystal habits. The schemes accounting for multi-habit mixtures and roughened ice particles (RNCO23 and RNCI23) should act to decrease the asymmetry factor compared with the Fu scheme case (RNFU23).

Marquart and Mayer (2002) emphasized an important discrepancy in contrail longwave radiative forcing caused by the effective emissivity approach combined with the maximum/random cloud overlap assumption. The MRCO23 case shows that a change in the cloud overlap assumption reduces both the shortwave and longwave contrail radiative forcings by 10-12%, resulting in a 14% decrease of net forcing. The vertical position of the contrail layer is equally important. If the contrail layer is placed 2 km higher, we find the net forcing can increase to 13.09 mW m^{-2} or 15.6% larger than the control case.

Contrail radiative forcing sensitivity to coverage and optical depth are tested in RNCO23OD and RNCO23F, where each parameter is reduced by 25%. The shortwave and longwave forcing components are greatly reduced in both cases, while the net

79

forcings vary little from the control case. Compared with the RNCO23OD case, the RNCO23F case shows the effect to be stronger from contrail coverage than from optical depth. Lastly, we compare the contrail radiative forcing simulated under the clear-sky condition (CRCO23) with the all-sky condition (RNCO23). Without the masking effects of natural clouds, the shortwave and longwave radiative forcings are significantly increased. However, the net radiative forcing increases by approximately 7.3%, which is close to that reported by Rap et al. (2010b).

Fig. 4.5 shows the monthly variation in the net contrail radiative forcing for all the cases. We use a prescribed global contrail coverage and optical depth, which does not reflect the monthly contrail variation, and is the primary reason for the difference between the present results and those reported by Rap et al. (2010b). However, the apparent monthly variation shown in Fig. 4.5 can also be attributed to influences from other factors, for example, natural cloud masking effects. All cases show stronger contrail forcing in December and January and weaker forcing in July, except for the CRCO23 case for clear-sky contrail forcing. The RNCO35 case has the largest contrail radiative forcing, indicative of the significant effect of contrail particle effective size. The MRCO23 case is distinctive from the other cases in that it uses the maximum/random cloud overlap approximation. This case represents the largest influence from natural cloud cover, which leads to the lowest forcing and the strongest variability. The contrail height level (RNCO23H) also affects the annual variability of contrail forcing.
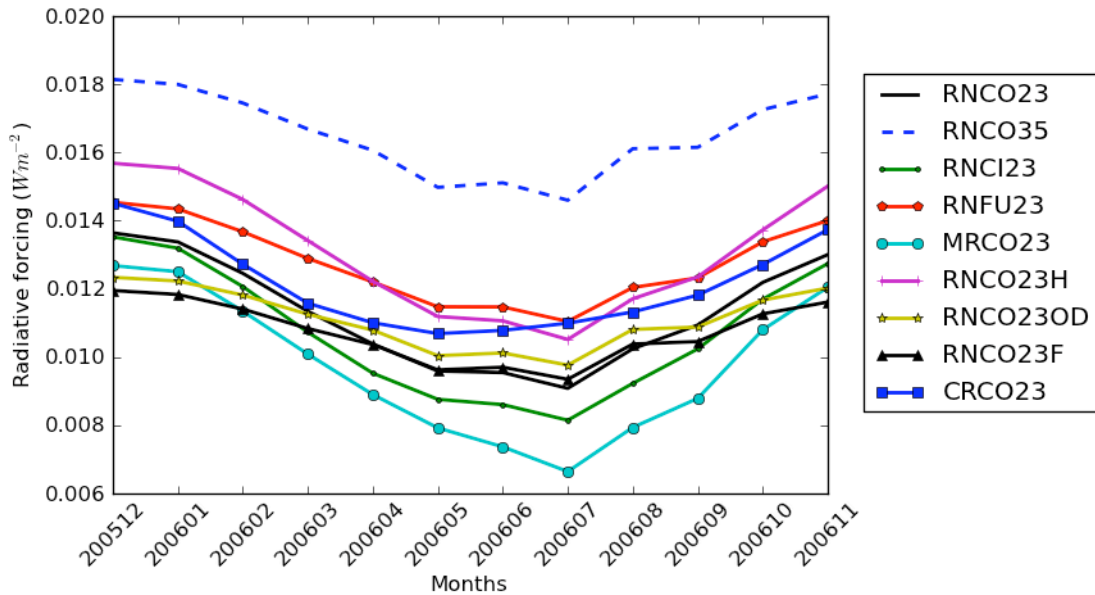
Fig. 4.5 Monthly variation in the net contrail radiative forcing for the control case and sensitivity test cases.

4.3.2 Results of online simulations

As have been mentioned above (section 4.2.2), although the contrail information is directly prescribed in the GCM simulation (with CAM5/CESM model) in the online modeling approach, the other physical processes within the model could induce changes to the contrail radiation fields. As a result, differences in the contrail radiative forcing between offline and online cases are expected. Fig. 4.6 reveals the online model simulated 2006 global annual averaged shortwave, longwave, and net contrail radiative forcing, similar to Fig. 4.3, with the corresponding values of -8.98 mW m^{-2}, 14.42 mW m^{-2}, and 5.44 mW m^{-2}, respectively. Comparing Fig. 4.6 and Fig. 4.3, it is apparent that

online model tends to give stronger SW contrail radiative forcing and weaker LW forcing, thus resulting in the lower NET contrail forcing than that of the offline model.

The three focal regions (North America, Europe, and East Asia) all have reduced contrail net radiative forcing by about 60% compared with the offline case. Reduced contrail radiative forcing within online model is also reported by Rap et al. (2010). However, the reason for the reduction in contrail forcing is complicated and is not easy to explain. Although there may be ample differences between the models used in Rap et al.'s study and this study, such contrail forcing reduction is partially attributed to the difference in cloud overlap assumptions used in offline and online models in this study. The control case in offline model uses Random overlap approximation, while the online model employs Maximum-Random overlap approximation (CAM5 default). Note that our sensitivity study with offline model has shown that using Maximum-Random approximation results in the lowest contrail forcing. As a result, we conclude that the cloud overlap assumption at least contributes to the reduction of contrail forcing to some extent.
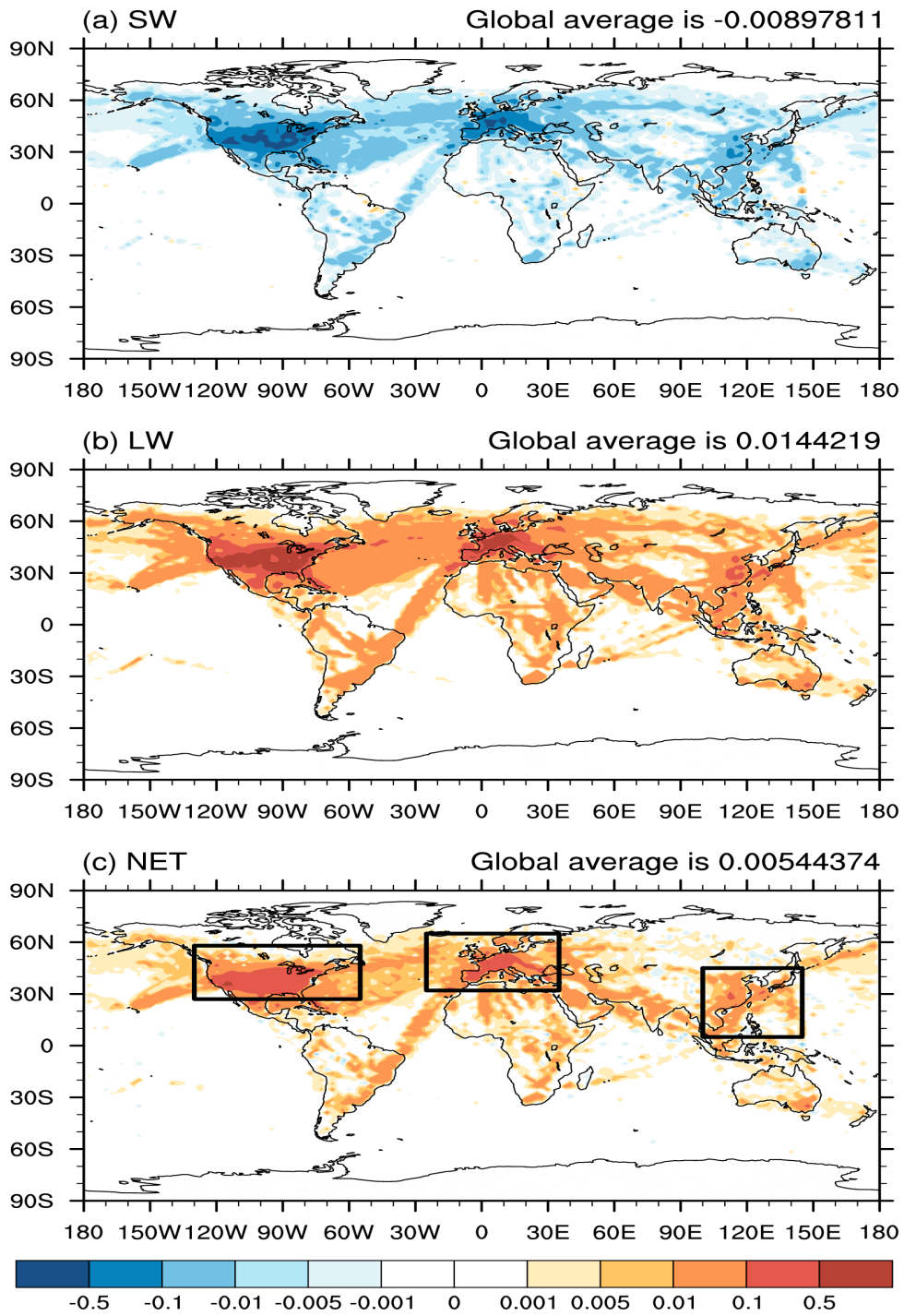
Fig. 4.6 Simulated 2006 global annual averaged shortwave (a), longwave (b), and net (c) contrail radiative forcing (W m^{-2}) in the online contrail forcing simulation.

4.3.3 Analysis of CoCIP data

From the above simulations and the sensitivity studies, the contrail particle effective size and contrail layer height are found to be among the major factors influencing the contrail radiative forcing. However, these factors are assumed to be spatially constant due to the lack of observations or simulations of contrail size and height information. What's more, all contrail information, including the contrail coverage and optical depth, are assumed to be invariant with time, which is also limited by the lack of data. The spatial and temporal variations of the contrail information are important for an accurate contrail forcing estimation.

Fortunately, updated and comprehensive contrail information can be made available by the Contrail Cirrus Prediction Tool (CoCiP, Schumann 2012). CoCiP is a compact model using physical parameterizations to simulate the contrail life-cycle under real meteorological conditions. More information about the CoCiP model can be found in Schumann et al. (2012). The new dataset is generated by running CoCiP model with the ECMWF reanalysis and covers a whole year from January to December in 2006. The temporal resolution is hourly, and the spatial resolution is 1x1 degree globally. The major variables include: contrail coverage, optical depth of contrails, ice water path of contrails, effective radius of contrails, mean pressure altitude of contrails, and temperature of contrails. The dataset undergoes various averaging in time and space to derive the annual, seasonal, monthly, and global or regional results shown below. In addition, they would finally be implemented in the offline and online contrail forcing simulations.
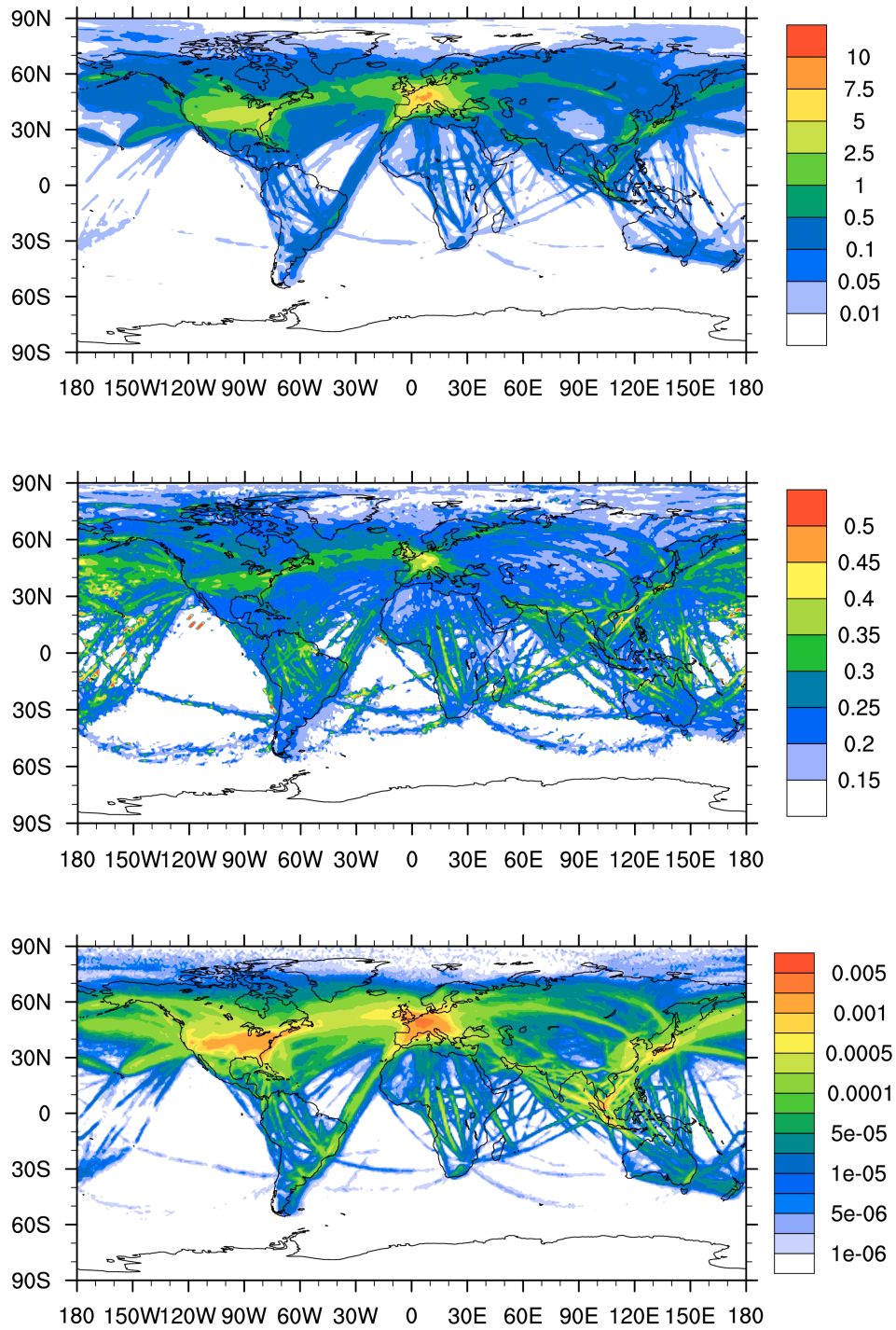
Fig. 4.7 Global annual averaged contrail coverage (upper panel, unit: percentage), optical depth (middle panel, unit: 1), and ice water path (lower panel, unit: kg m^{-2}) for 2006 simulated by CoCiP.

In Fig. 4.7, the annual averaged contrail coverage, optical depth and ice water path over the global are shown. The global annual averaged values are 0.187%, 0.181, and 0.0664 g m^{-2}, respectively. Compared with Rap et al. (2010) contrail distributions, the global annual averaged contrail coverage increases while the contrail optical depth is reduced. Another striking difference in the distribution of contrail between CoCiP results and Rap et al. (2010) is that Europe surpasses North America and becomes the region with the largest contribution to the global contrails. But generally, the contrail spatial distribution patterns do not change significantly from the year 2002 to 2006.

Not only the spatial distribution of contrail is inhomogeneous, the temporal variations of contrail are also not constant. Fig. 4.8 shows the monthly variations of contrail coverage and optical depth in 2006 over the globe and three major regions with intense air traffic (North America, Europe and East Asia). The same division of regions is followed with Table 4.2. The global averaged contrail fraction is almost constant within the year 2006. The regional averaged contrail fraction over East Asia is higher than the global average from March to November, while displays a global mean value in the remaining months. However, the regional averages in North America and Europe are persistently five times larger than the global average. Peak values of contrail coverage in Europe can reach 3.3% in October and 2.3% in May. Again, the global averaged contrail optical depth doesn't show much variation with time, while the regional averages range from about 0.2 to 0.3. All regions agree that the peak of contrail optical depth appears in boreal summer months (June to September) and the lowest in boreal winter months.
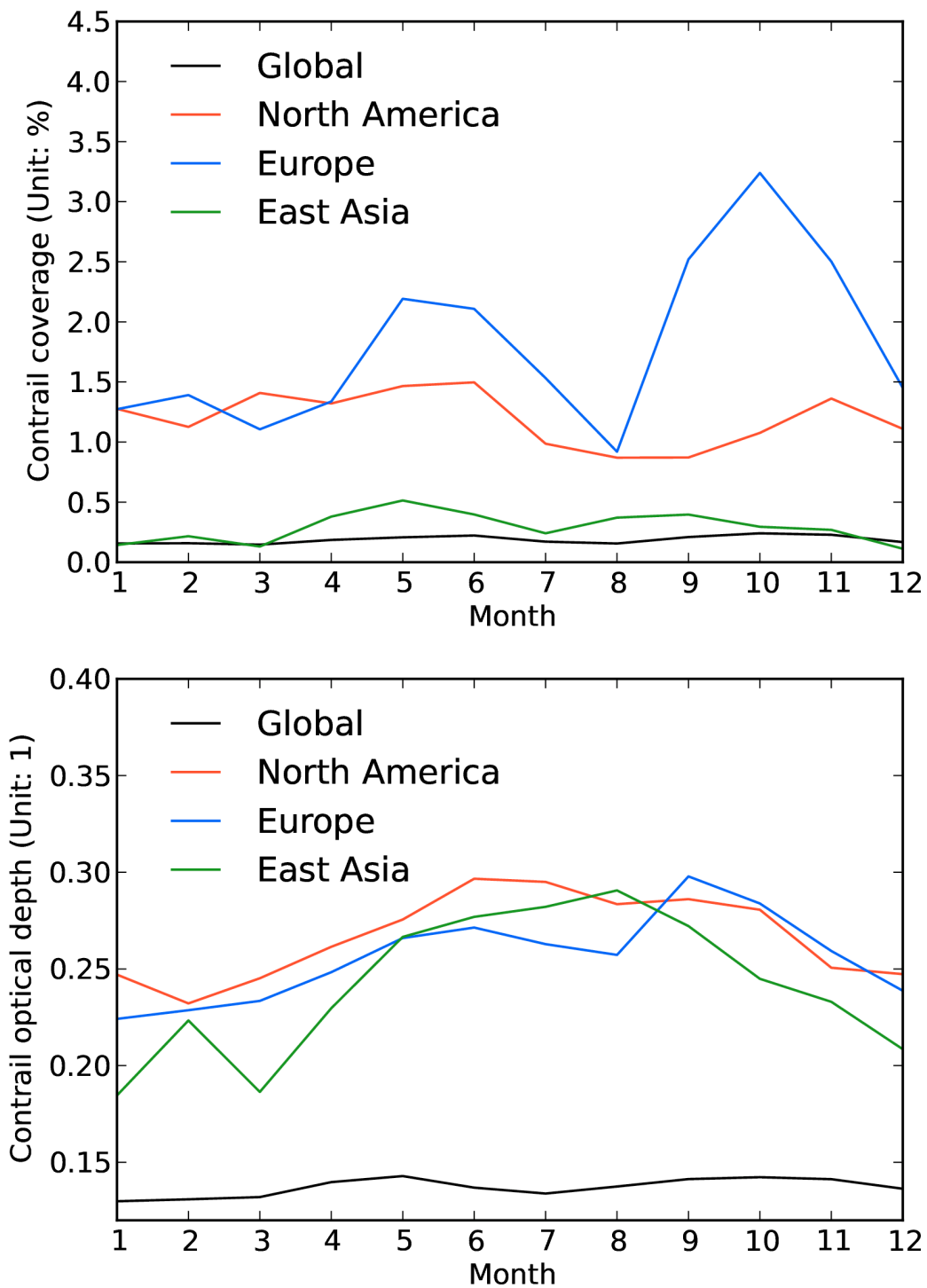
Fig. 4.8 Monthly variations of contrail coverage (upper panel) and optical depth (lower panel) in 2006.
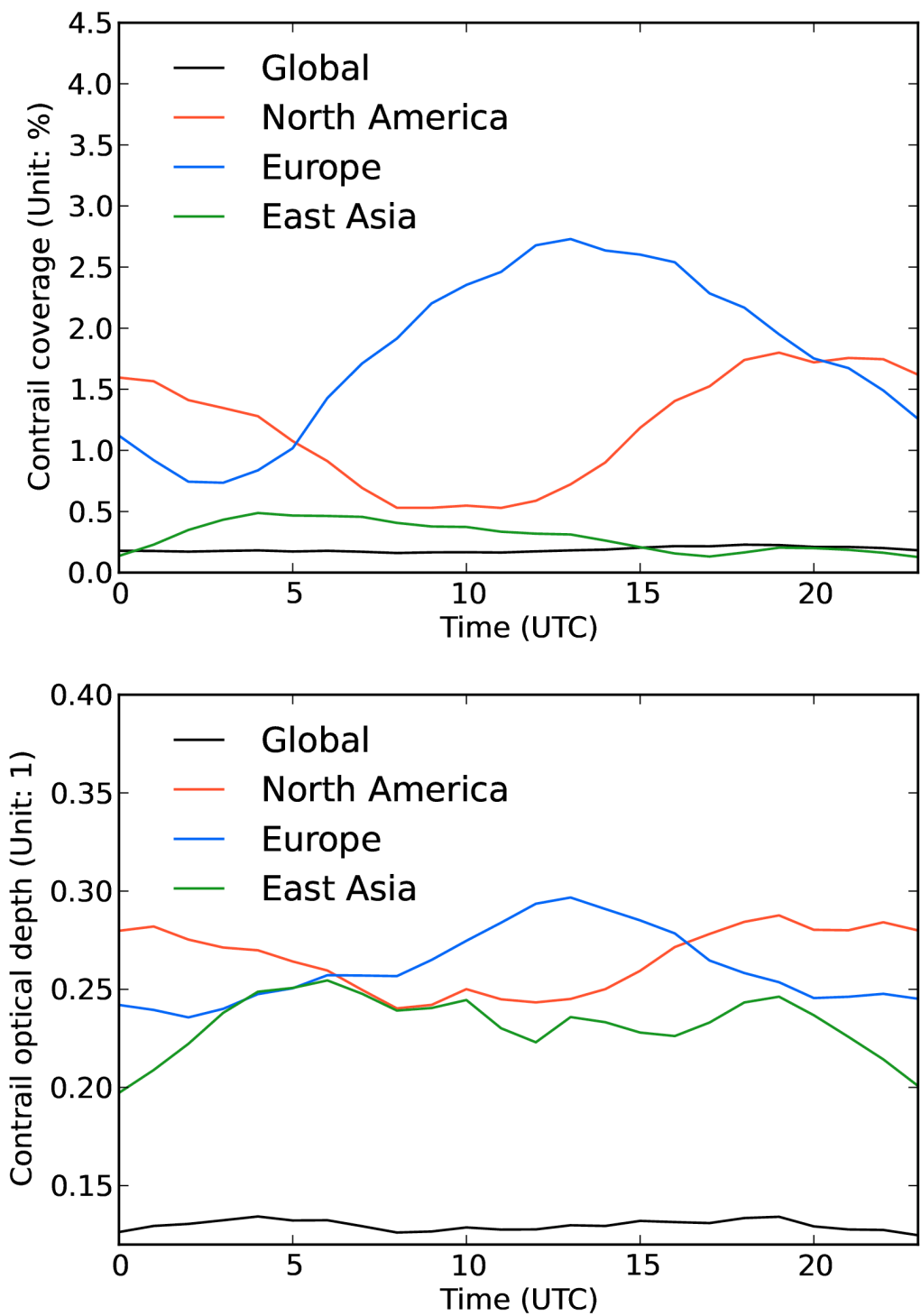
Fig. 4.9 Diurnal variations of contrail coverage (upper panel) and optical depth (lower panel).

Diurnal variation of contrails is another important temporal feature at hourly time scale. From Fig. 4.9, we find that although the global averaged contrail coverage shows little variation with time, all three regional averages have sinusoidal variation with local time. Notice that all three regions show peak contrail coverage and optical depth at noon locally. For example, in Europe, the peak time is at 12:00 UTC; in North America, at 18:00 UTC; in East Asia, at 4:00 UTC. This temporal distribution is highly related to the aviation activities carried out by human being which peak at day-time and low at night-time. The maximum contrail fraction can be more than four times larger than the minimum during a one-day variation. The diurnal variation of contrail optical depth is not so strong as the contrail fraction, but still shows a value change of about 0.05 which amounts to 10-25% changes in the regional averages. This finding indicates that diurnal variation of contrails is an important feature that shouldn't be neglected when estimating the contrail radiative forcing. Due to the large differences in shortwave and longwave radiation in the day-time and night-time, the contrail radiative forcing can be significant changed within a day. Unfortunately, except for a few online models that have prognostic contrail information to resolve the diurnal feature, most models fails to take this important factor into account.

The other important information about contrail is the effective size and the vertical height level of contrails. Fig. 4.10 shows the spatial distribution of the contrail effective radius in four respective months (April, July, October, and January) in 2006 provided by CoCiP. Fig. 4.11 is the same as Fig. 4.10, except for showing the pressure altitudes of contrail.
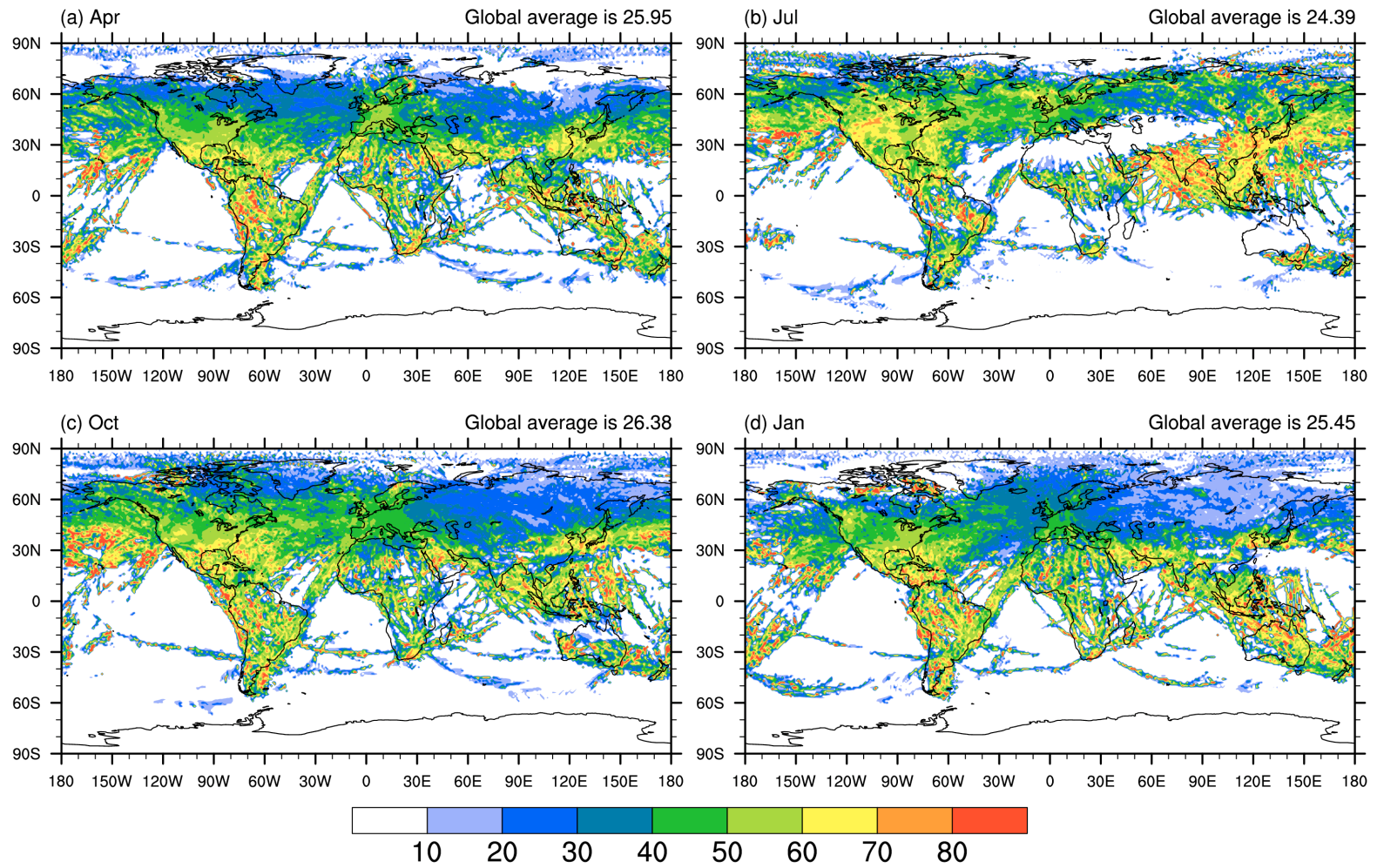
Fig. 4.10 Spatial variations of effective radius of contrails (unit: μm) in (a) April; (b) July; (c) October; (d) January in 2006.
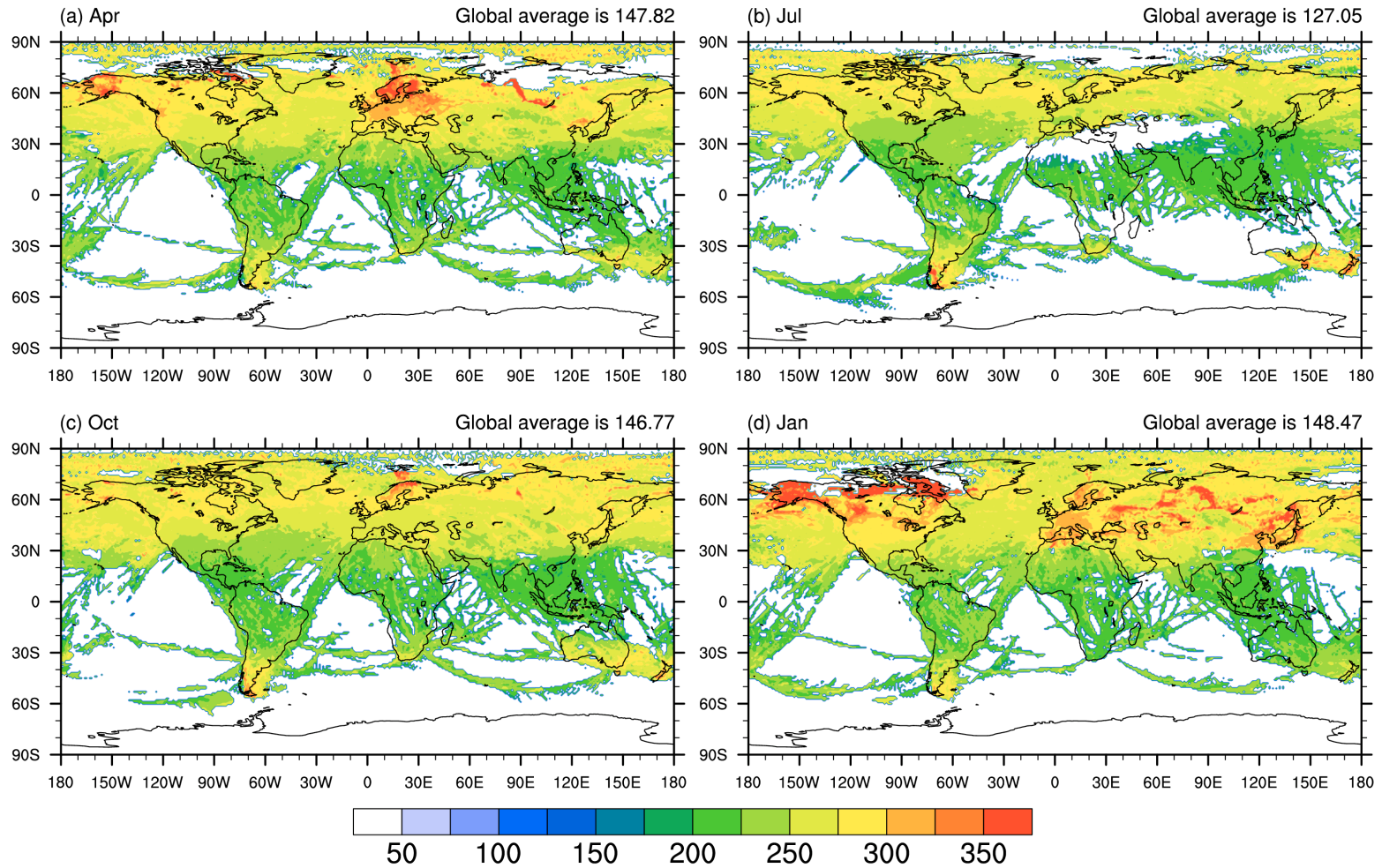
Fig. 4.11 Spatial variations of pressure altitude of contrails (unit: hPa) in (a) April; (b) July; (c) October; (d) January in 2006.

From a global averaged perspective, both the contrail effective radius and pressure altitude do not show much difference in each month. Instead, regional differences are evident. Generally, contrails in the tropical regions have larger effective sizes and occur at higher altitudes. The mid-latitude contrails locate at around 270 hPa on average, which is consistent with results from satellite observations by Iwabuchi et al. (2012) that contrail-top altitude is around 10.9 km. Contrail effective sizes do not show noticeable difference over land and ocean in July and October, while contrail particles over land are found to be larger in size in January and April. It should be noticed that contrail particle effective size from CoCiP is much larger than previously estimated results (about 50 μm versus 23 μm in effective diameter).

4.3.4 Preliminary online modeling result using CoCiP data

Although it is important and beneficial to incorporate the temporal variation of contrails into the model to derive a more accurate estimation of contrail radiative forcing, technical implementation is not easy. Here we show a preliminary result similar to the above online simulations where contrail fields are kept constant in time while the new contrail particle size and pressure altitude are added. Fig. 4.12 shows the simulated 2006 global annual averaged contrail radiative forcing in the online contrail forcing simulation using the CoCiP data. We notice that the shortwave, longwave and net contrail forcing are all strengthened. The reason is attributed to the newly added contrail size and pressure height information. More simulation results and anlysis are underway and will be available in the near future.
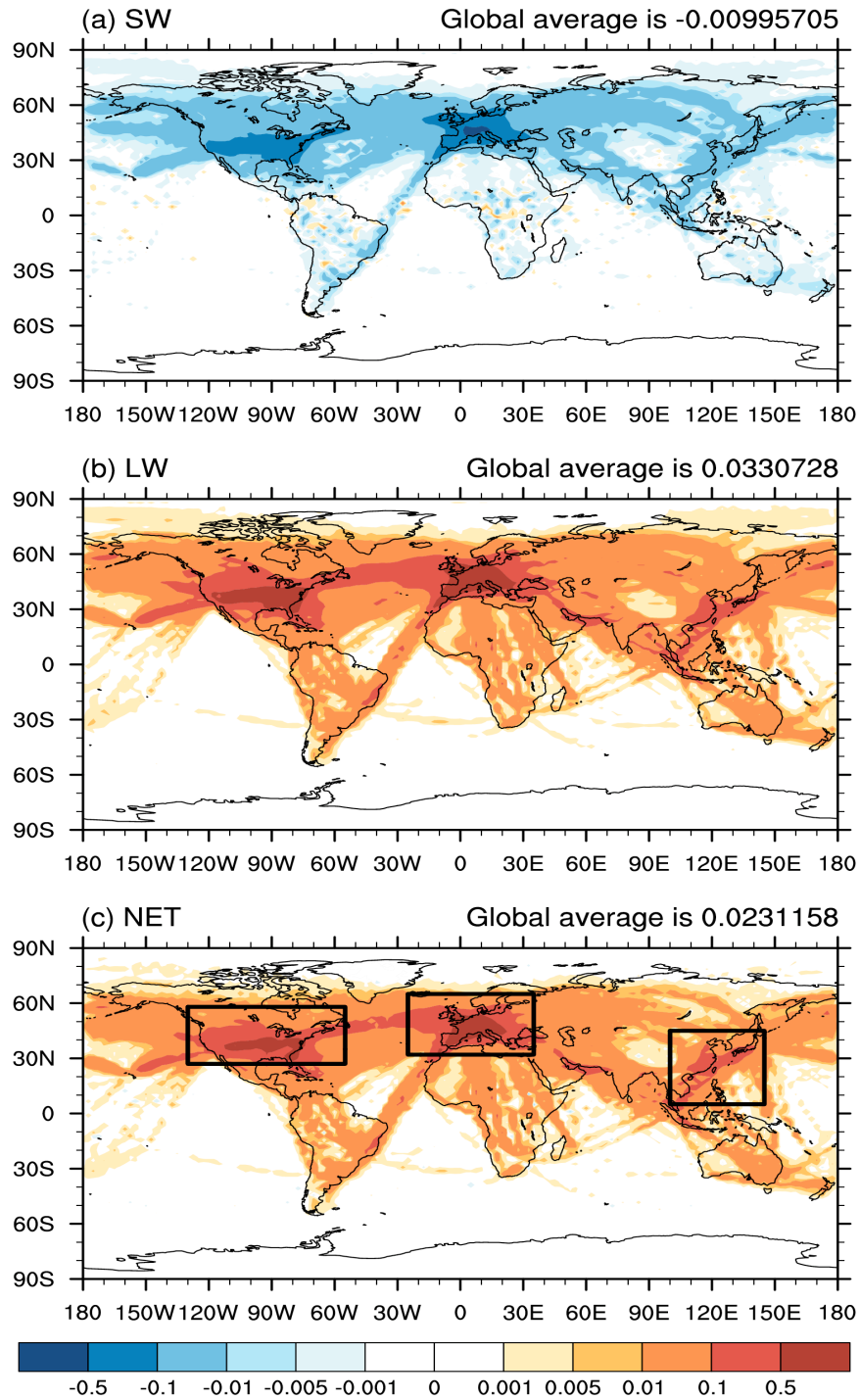
Fig. 4.12 Simulated 2006 global annual averaged shortwave (a), longwave (b), and net (c) contrail radiative forcing (W m^{-2}) in the online contrail forcing simulation using the CoCiP data.

4.4 Conclusions

Although great advances have been achieved in simulating global contrail radiative forcing by sophisticated GCM models, various uncertainties remain and prevent a more precise forcing determination. We employ an offline simulation approach using the CAM5 modeled atmospheric profile and cloud information as inputs and the RRTMG radiative transfer code to simulate the contrail radiative forcing. The annual mean global contrail coverage and optical depth for the year 2002 are adapted from Rap et al. (2010b). Persistent contrails are not included. We use a new contrail optical properties parameterization scheme to derive the annual 2006 mean shortwave, longwave, and net contrail radiative forcings, respectively, -6.24, 17.56, and 11.32 mW m^{-2}. Regional contrail radiative forcing can be more than ten times higher than the global averages (e.g., North America).

Sensitivity test cases are implemented to determine the effect of various factors on contrail radiative forcing. Results show that contrail particle effective size, contrail layer height, the model cloud overlap assumption, and contrail optical properties are among the most important factors. Thus, retrieving accurate information about the contrail particle size and vertical height are imperative to determining the correct contrail forcing. In addition to determining the contrail forcing, a more model-consistent treatment of cloud overlap and parameterizations of the contrail optical properties are vitally needed.

Online model results show stronger SW contrail radiative forcing and weaker LW forcing, thus resulting in a lower NET contrail forcing than that of the offline model.

This reduction in NET radiative forcing is attributed partially to the different cloud overlap assumption used in the offline and online models.

The CoCiP data provides additional temporal and spatial variations of contrail for analytical and modeling purposes. The monthly and diurnal variations of contrail fraction and optical depth are clearly identified. The variations of contrail effective size and contrail layer pressure altitude with space are also depicted. Preliminary online simulation of contrail radiative forcing using the CoCiP data shows stronger global contrail forcing. More simulations are to be carried out in the future.

CHAPTER V

SUMMARY

5.1 Summary

Focusing on the central question of resolving uncertainties and improving representations of dust aerosol and ice cloud optical properties and their radiative effects in the numerical model simulations, this dissertation explores three important objects, namely, dust aerosols, natural cirrus clouds, and contrails. Uncertainties associated with their optical properties and radiative effects are fully tested and analyzed.

In Chapter II, the uncertainties from dust particle shape and refractive index on radiative transfer simulation were discussed. The composition, particle shape, number concentration, size distribution, and spatial and temporal distributions of dust aerosols cause significant uncertainties in relevant radiative transfer simulations. The spherical particle approximation has been generally recognized to introduce errors in radiative transfer calculations involving dust aerosols. Although previous studies have attempted to quantify the effect of non-spherical particles, no consensus has been reached as to the significance of the dust aerosols non-spherical effect on flux calculations. For this study, we utilize a newly developed ultra-violet-to-far-infrared spectral database of the single-scattering properties of tri-axial ellipsoidal, mineral dust-like aerosols to study the non-spherical effect on radiative forcing. The radiance and flux differences between the spherical and ellipsoidal models are obtained for various refractive indices and particle size distributions. The errors originating from using the spherical model and the

uncertainties in the refractive indices are quantified at both the top and bottom of the atmosphere. The dust non-spherical effect on the net flux and heating rate profile is obtained over the entire range of the solar spectrum. The particle shape effect is found to be related to the dust optical depth and the surface albedo and can be an important uncertainty source in radiative transfer simulation. The particle shape effect is largest over water surfaces and can cause up to a 30% difference in dust forcing at the top of the atmosphere.

In Chapter III, we explored how the ice particle surface roughening influences on the global cloud radiative effect. Ice clouds influence the climate system by changing the radiation budget and large-scale circulation. Therefore, climate models need to have an accurate representation of ice clouds and their radiative effects. In this paper, new broadband parameterizations for ice cloud bulk scattering properties are developed for severely roughened ice particles. The parameterizations are based on a general habit mixture that includes nine habits (droxtals, hollow/solid columns, plates, solid/hollow bullet rosettes, aggregate of solid columns, and small/large aggregates of plates). The scattering properties for these individual habits incorporate recent advances in light scattering computations. The influence of ice particle surface roughness on ice cloud radiative effect is determined through simulations with the Fu-Liou and RRTMG radiative transfer codes, and the National Center for Atmospheric Research Community Atmosphere Model (CAM, version 5.1). The differences in shortwave (SW) and longwave (LW) radiative effect at both the top of the atmosphere and the surface are determined for smooth and severely roughened ice particles. While the influence of

particle roughening on the single-scattering properties is negligible in the LW, the results indicate that ice crystal roughness can change the SW forcing locally by more than 10 Wm^{-2} over a range of effective diameters. The global averaged SW cloud radiative effect due to ice particle surface roughness is estimated to be roughly 1-2 Wm^{-2}. The CAM results indicate that ice particle roughening can result in large regional SW radiative effect and a small but non-negligible increase in global LW cloud radiative effect.

In Chapter IV, contrail optical properties and radiative effects were studied using modeling techniques. The contrail radiative forcing induced by human aviation activity is one of the most uncertain contributions to climate forcing. An accurate estimation of global contrail radiative forcing is imperative, and the modeling approach is an effective and prominent method to investigate the sensitivity of contrail forcing to various potential factors. We use a simple offline model framework that is particularly useful for sensitivity studies. The most-up-to-date Community Atmospheric Model version 5 (CAM5) is employed to simulate the atmosphere and cloud conditions during the year 2006. With updated natural cirrus and additional contrail optical property parameterizations, the RRTMG Model (RRTM-GCM application) is used to simulate the global contrail radiative forcing. Global contrail coverage and optical depth derived from the literature for the year 2002 is used. The 2006 global annual averaged contrail net (shortwave + longwave) radiative forcing is estimated to be 11.3 mW m^{-2}. Regional contrail radiative forcing over dense air traffic areas can be more than ten times stronger than the global average. A series of sensitivity tests are implemented and show that contrail particle effective size, contrail layer height, the model cloud overlap assumption,

and contrail optical properties are among the most important factors. The difference between the contrail forcing under all and clear skies is also shown. New online modeling framework and new CoCiP contrail distribution data show promising results and could be used in future analysis.

5.2 Future work and directions

Further intensive studies in the three aspects discussed in this dissertation are greatly needed to validate and to implement the present results in broader applications.

For the exploration of uncertain factors from dust particle shape and refractive index in Chapter II, we have derived the best-fit particle shape distribution with the nonspherical ellipsoidal particle model. This can be potentially used in the future dust optical property parameterization within GCMs. Colarco et al. (2013) take the first initiative to implement the particle shape distribution found in this study into NASA GEOS-5 AGCM, compare the results with satellite (MODIS, MISR and CALIOP) and ground-based (AERONET) observations, and discuss the radiative effect and atmospheric heating due to the choice of particle shapes. Similar studies should be carried out to compare model results with real observations (such as at ARM SGP site) to help improve the particle shape model.

In the study of ice particle surface roughening on cloud radiative effect, we developed a new ice cloud optical property parameterization scheme which takes ice particle roughening into account. In order to promote the application of this new parameterization in other models, more validation studies are needed where comparisons

with real observational results are to be carried out. We would work towards the use of a unified ice cloud optical properties in both remote sensing and numerical modeling communities for a more consistent comparison between the two.

The present contrail radiative forcing studies are limited to using a constant global contrail distribution map without considering diurnal and seasonal variations. We have shown in the analysis of the new CoCiP data that diurnal and seasonal variations of contrails are significant and should not be ignored. Including these variations of contrails in future modeling studies can help derive a better estimate of the radiative effect induced by the human aviation activities. More efforts may be directed to the study of contrail contaminated by black carbon emitted from aircraft exhaust. Liou et al. (2013) pioneer in the calculation of the optical properties of soot-contaminated contrails by proposing a geometric-optics surface-wave approach, and conclude that soot mixing associated with the contrail particle formation is critical for estimation of contrail radiative forcing. The incorporation and better representation of contrail and contrail optical properties in GCMs precisely still remain a question to be addressed.

REFERENCES

Albrecht, B. A. 1989. "Aerosols, cloud microphysics, and fractional cloudiness." Science no. 245 (4923):1227-1230. doi: 10.1126/science.245.4923.1227.

d'Almeida, G. A., P. Koepke, and E. P. Shettle. 1991. "Atmospheric Aerosols: Global Climatology and Radiative Characteristics." Hampton: A.Deepak Publishing.

Anderson, G. P., S. A. Clough, F. X. Kneizys, J. H. Chetwynd, and E. P. Shettle. 1986. "AFGL atmospheric constituent profiles (0–120 km)", Tech. Rep. AFGL-TR-86-0110, Air Force Geophys. Lab., Hanscom Air Force Base, Mass.

Baldridge, A. M., S. J. Hook, C. I. Grove, and G. Rivera. 2009. "The ASTER spectral library version 2.0." Remote Sensing of Environment no. 113 (4):711-715. doi: 10.1016/j.rse.2008.11.007.

Baran, A. J. 2009. "A review of the light scattering properties of cirrus." Journal of Quantitative Spectroscopy & Radiative Transfer no. 110 (14-16):1239-1260. doi: 10.1016/j.jqsrt.2009.02.026.

Baran, A. J. 2012. "From the single-scattering properties of ice crystals to climate prediction: A way forward." Atmospheric Research no. 112:45-69. doi: 10.1016/j.atmosres.2012.04.010.

Baum, B. A., P. Yang, A. J. Heymsfield, S. Platnick, M. D. King, Y. X. Hu, and S. T. Bedka. 2005. "Bulk scattering properties for the remote sensing of ice clouds. Part II: Narrowband models." Journal of Applied Meteorology no. 44 (12):1896-1911. doi: 10.1175/jam2309.1.

Baum, B. A., P. Yang, A. J. Heymsfield, C. G. Schmitt, Y. Xie, A. Bansemer, Y. X. Hu, and Z. B. Zhang. 2011. "Improvements in shortwave bulk scattering and absorption models for the remote sensing of ice clouds." Journal of Applied Meteorology and Climatology no. 50 (5):1037-1056. doi: 10.1175/2010jamc2608.1.

Bi, L., P. Yang, G. W. Kattawar, B. A. Baum, Y. X. Hu, D. M. Winker, R. S. Brock, and J. Q. Lu. 2009. "Simulation of the color ratio associated with the backscattering of radiation by ice particles at the wavelengths of 0.532 and 1.064 mu m." Journal of Geophysical Research-Atmospheres no. 114. D00h08. doi: 10.1029/2009jd011759.

Bi, L., P. Yang, G. W. Kattawar, and R. Kahn. 2009. "Single-scattering properties of triaxial ellipsoidal particles for a size parameter range from the Rayleigh to geometric-optics regimes." Applied Optics no. 48 (1):114-126.

Bohren, C.F., and D.R. Huffman, 1983. "Absorption and scattering of light by small particles." New York: Wiley-Interscience.

Burkhardt, U., and B. Karcher. 2009. "Process-based simulation of contrail cirrus in a global climate model." Journal of Geophysical Research-Atmospheres no. 114. D16201. doi: 10.1029/2008jd011491.

Burkhardt, U., and B. Karcher. 2011. "Global radiative forcing from contrail cirrus." Nature Climate Change no. 1 (1):54-58. doi: 10.1038/nclimate1068.

Chance, K., and R. L. Kurucz. 2010. "An improved high-resolution solar reference spectrum for earth's atmosphere measurements in the ultraviolet, visible, and near infrared." Journal of Quantitative Spectroscopy & Radiative Transfer no. 111 (9):1289-1295. doi: 10.1016/j.jqsrt.2010.01.036.

Chen, C. C., A. Gettelman, C. Craig, P. Minnis, and D. P. Duda. 2012. "Global contrail coverage simulated by CAM5 with the inventory of 2006 global aircraft emissions." Journal of Advances in Modeling Earth Systems no. 4. M04003. doi: 10.1029/2011ms000105.

Cole, B. H., P. Yang, B. A. Baum, J. Riedi, L. C. Labonnote, F. Thieuleux, and S. Platnick. 2013. "Comparison of PARASOL observations with polarized reflectances simulated using different ice habit mixtures." Journal of Applied Meteorology and Climatology no. 52 (1):186-196. doi: 10.1175/jamc-d-12-097.1.

Comstock, J. M., T. P. Ackerman, and G. G. Mace. 2002. "Ground-based lidar and radar remote sensing of tropical cirrus clouds at Nauru Island: Cloud statistics and radiative impacts." Journal of Geophysical Research-Atmospheres no. 107 (D23). 4714. doi: 10.1029/2002jd002203.

Colarco, P., E. Nowottnick, C. Randles, B. Yi, P. Yang, J. Smith, C. Bardeen. 2013. "Impact of radiatively interactive dust aerosols in the NASA GEOS-5 climate model: Sensitivity to dust particle shape and refractive index." Journal of Geophysical Research-Atmospheres, submitted.

Cross, J. D. 1969. "Scanning electron microscopy of evaporating ice." Science no. 164 (3876):174-&. doi: 10.1126/science.164.3876.174.

Davy, J. G., and D. Branton. 1970. "Subliming ice surfaces: freeze-etch electron microscopy." Science no. 168 (3936):1216-&. doi: 10.1126/science.168.3936.1216.

Dubovik, O., A. Sinyuk, T. Lapyonok, B. N. Holben, M. Mishchenko, P. Yang, T. F. Eck, H. Volten, O. Munoz, B. Veihelmann, W. J. van der Zande, J.-F. Leon, M. Sorokin, and I. Slutsker. 2006. "Application of spheroid models to account for aerosol particle nonsphericity in remote sensing of desert dust." Journal of Geophysical Research-Atmospheres no. 111 (D11). doi: 10.1029/2005jd006619.

Ebert, E. E., and J. A. Curry. 1992. "A parameterization of ice-cloud optical properties for climate models." Journal of Geophysical Research-Atmospheres no. 97 (D4):3831-3836.

Edwards, J. M., S. Havemann, J. C. Thelen, and A. J. Baran. 2007. "A new parameterization for the radiative properties of ice crystals: Comparison with existing schemes and impact in a GCM." Atmospheric Research no. 83 (1):19-35. doi: 10.1016/j.atmosres.2006.03.002.

Feng, Q., P. Yang, G. W. Kattawar, C. N. Hsu, S.-C. Tsay, and I. Laszlo. 2009. "Effects of particle nonsphericity and radiation polarization on retrieving dust properties from MODIS observations." Journal of Aerosol Science no. 40 (9):776-789. doi: 10.1016/j.jaerosci.2009.05.001.

Foot, J. S. 1988. "Some observations of the optical-properties of clouds: 2. Cirrus." Quarterly Journal of the Royal Meteorological Society no. 114 (479):145-164. doi: 10.1002/qj.49711447908.

Forster, P., V. Ramaswamy, P. Artaxo, T. Berntsen, R. Betts, et al. 2007. "Changes in atmospheric constituents and in radiative forcing." in "Climate Change 2007: The Physical Science Basis. Contribution of Working Group I to the Fourth Assessment Report of the Intergovernmental Panel on Climate Change." edited by S. Solomon et al., 131–234, Cambridge: Cambridge Univ. Press.

Fromming, C., M. Ponater, U. Burkhardt, A. Stenke, S. Pechtl, and R. Sausen. 2011. "Sensitivity of contrail coverage and contrail radiative forcing to selected key parameters." Atmospheric Environment no. 45 (7):1483-1490. doi: 10.1016/j.atmosenv.2010.11.033.

Fu, Q. 2007. "A new parameterization of an asymmetry factor of cirrus clouds for climate models." Journal of the Atmospheric Sciences no. 64 (11):4140-4150. doi: 10.1175/2007jas2289.1.

Fu, Q. 1996. "An accurate parameterization of the solar radiative properties of cirrus clouds for climate models." Journal of Climate no. 9 (9):2058-2082. doi: 10.1175/1520-0442(1996)009<2058:aapots>2.0.co;2.

Fu, Q., and K. N. Liou. 1993. "Parameterization of the radiative properties of cirrus clouds." Journal of the Atmospheric Sciences no. 50 (13):2008-2025. doi: 10.1175/1520-0469(1993)050<2008:potrpo>2.0.co;2.

Fu, Q., T. J. Thorsen, J. Su, J. M. Ge, and J. P. Huang. 2009. "Test of Mie-based single-scattering properties of non-spherical dust aerosols in radiative flux calculations." Journal of Quantitative Spectroscopy & Radiative Transfer no. 110 (14-16):1640-1653. doi: 10.1016/j.jqsrt.2009.03.010.

Fu, Q., P. Yang, and W. B. Sun. 1998. "An accurate parameterization of the infrared radiative properties of cirrus clouds for climate models." Journal of Climate no. 11 (9):2223-2237. doi: 10.1175/1520-0442(1998)011<2223:aapoti>2.0.co;2.

Hartmann, D. L., M. E. Ockertbell, and M. L. Michelsen. 1992. "The effect of cloud type on earth's energy balance: Global analysis." Journal of Climate no. 5 (11):1281-1304. doi: 10.1175/1520-0442(1992)005<1281:teocto>2.0.co;2.

Haywood, J., and O. Boucher. 2000. "Estimates of the direct and indirect radiative forcing due to tropospheric aerosols: A review." Reviews of Geophysics no. 38 (4):513-543. doi: 10.1029/1999rg000078.

Heymsfield, A. J., C. Schmitt, A. Bansemer, and C. H. Twohy. 2010. "Improved representation of ice particle masses based on observations in natural clouds." Journal of the Atmospheric Sciences no. 67 (10):3303-3318. doi: 10.1175/2010jas3507.1.

Heymsfield, A. J., C. Schmitt, and A. Bansemer, 2013. "Ice cloud particle size distributions and pressure dependent terminal velocities from in situ observations at temperatures from 0° to -86°C." Journal of the Atmospheric Sciences. In press, doi: 10.1175/JAS-D-12-0124.1.

Hong, G., P. Yang, B. A. Baum, A. J. Heymsfield, and K. M. Xu. 2009. "Parameterization of shortwave and longwave radiative properties of ice clouds for use in climate models." Journal of Climate no. 22 (23):6287-6312. doi: 10.1175/2009jcli2844.1.

Hong, G., P. Yang, P. Minnis, Y. X. Hu, and G. North. 2008. "Do contrails significantly reduce daily temperature range?" Geophysical Research Letters no. 35 (23). L23815. doi: 10.1029/2008gl036108.

Iacono, M. J., J. S. Delamere, E. J. Mlawer, M. W. Shephard, S. A. Clough, and W. D. Collins. 2008. "Radiative forcing by long-lived greenhouse gases: Calculations with the AER radiative transfer models." Journal of Geophysical Research-Atmospheres no. 113 (D13). doi: 10.1029/2008jd009944.

Iwabuchi, H., P. Yang, K. N. Liou, and P. Minnis. 2012. "Physical and optical properties of persistent contrails: Climatology and interpretation." Journal of Geophysical Research-Atmospheres no. 117. D06215. doi: 10.1029/2011jd017020.

Kahnert, M. 2004. "Reproducing the optical properties of fine desert dust aerosols using ensembles of simple model particles." Journal of Quantitative Spectroscopy & Radiative Transfer no. 85 (3-4):231-249. doi: 10.1016/s0022-4073(03)00227-9.

Kahnert, M., and A. Kylling. 2004. "Radiance and flux simulations for mineral dust aerosols: Assessing the error due to using spherical or spheroidal model particles." Journal of Geophysical Research-Atmospheres no. 109 (D9). doi: 10.1029/2003jd004318.

Kahnert, M., T. Nousiainen, and P. Raisanen. 2007. "Mie simulations as an error source in mineral aerosol radiative forcing calculations." Quarterly Journal of the Royal Meteorological Society no. 133 (623):299-307. doi: 10.1002/qj.40.

Kahnert, M., T. Nousiainen, and B. Veihelmann. 2005. "Spherical and spheroidal model particles as an error source in aerosol climate forcing and radiance computations: A case study for feldspar aerosols." Journal of Geophysical Research-Atmospheres no. 110 (D18). doi: 10.1029/2004jd005558.

Kalashnikova, O. V., and I. N. Sokolik. 2002. "Importance of shapes and compositions of wind-blown dust particles for remote sensing at solar wavelengths." Geophysical Research Letters no. 29 (10). doi: 10.1029/2002gl014947.

Kalashnikova, O. V., and I. N. Sokolik. 2004. "Modeling the radiative properties of nonspherical soil-derived mineral aerosols." Journal of Quantitative Spectroscopy & Radiative Transfer no. 87 (2):137-166. doi: 10.1016/j.jqsrt.2003.12.026.

Labonnote, L. C., G. Brogniez, J. C. Buriez, M. Doutriaux-Boucher, J. F. Gayet, and A. Macke. 2001. "Polarized light scattering by inhomogeneous hexagonal monocrystals: Validation with ADEOS-POLDER measurements." Journal of Geophysical Research-Atmospheres no. 106 (D11):12139-12153.

Lee, J., P. Yang, A. E. Dessler, B. C. Gao, and S. Platnick. 2009. "Distribution and radiative forcing of tropical thin cirrus clouds." Journal of the Atmospheric Sciences no. 66 (12):3721-3731. doi: 10.1175/2009jas3183.1.

Levoni, C., M. Cervino, R. Guzzi, and F. Torricella. 1997. "Atmospheric aerosol optical properties: a database of radiative characteristics for different components and classes." Applied Optics no. 36 (30):8031-8041. doi: 10.1364/ao.36.008031.

Liou, K. N. 1986. "Influence of cirrus clouds on weather and climate processes - A global perspective." Monthly Weather Review no. 114 (6):1167-1199. doi: 10.1175/1520-0493(1986)114<1167:ioccow>2.0.co;2.

Liou, K. N., Y. Takano, Q. Yue, and P. Yang. 2013. "On the radiative forcing of contrail cirrus contaminated by black carbon.", Geophysical Research Letters 40:1-7. doi:10.1002/grl.50110.

Lynch, D. K., K. Sassen, D. O. Starr, and G. Stephens. 2002. "Cirrus." New York: Oxford University Press.

Macke, A. 1993. "Scattering of light by polyhedral ice crystals." Applied Optics no. 32 (15):2780-2788.

Marquart, S., and B. Mayer. 2002. "Towards a reliable GCM estimation of contrail radiative forcing." Geophysical Research Letters no. 29 (8). doi: 10.1029/2001gl014075.

Marquart, S., M. Ponater, F. Mager, and R. Sausen. 2003. "Future development of contrail cover, optical depth, and radiative forcing: Impacts of increasing air traffic and climate change." Journal of Climate no. 16 (17):2890-2904. doi: 10.1175/1520-0442(2003)016<2890:FDOCCO>2.0.CO;2

Mayer, B., and A. Kylling. 2005. "Technical note: The libRadtran software package for radiative transfer calculations - description and examples of use." Atmospheric Chemistry and Physics no. 5:1855-1877.

McConnell, C. L., P. Formenti, E. J. Highwood, and M. A. J. Harrison. 2010. "Using aircraft measurements to determine the refractive index of Saharan dust during

the DODO Experiments." Atmospheric Chemistry and Physics no. 10 (6):3081-3098. doi: 10.5194/acp-10-3081-2010.

Meng, Z., P. Yang, G. W. Kattawar, L. Bi, K. N. Liou, and I. Laszlo. 2010. "Single-scattering properties of tri-axial ellipsoidal mineral dust aerosols: A database for application to radiative transfer calculations." Journal of Aerosol Science no. 41 (5):501-512. doi: 10.1016/j.jaerosci.2010.02.008.

Meyer, R., H. Mannstein, R. Meerkotter, U. Schumann, and P. Wendling. 2002. "Regional radiative forcing by line-shaped contrails derived from satellite data." Journal of Geophysical Research-Atmospheres no. 107 (D10):17. doi: 10.1029/2001jd000426.

Minnis, P., R. Palikonda, B. J. Walter, J. K. Ayers, and H. Mannstein. 2005. "Contrail properties over the eastern North Pacific from AVHRR data." Meteorologische Zeitschrift no. 14 (4):515-523. doi: 10.1127/0941-2948/2005/0056.

Minnis, P., U. Schumann, D. R. Doelling, K. M. Gierens, and D. W. Fahey. 1999. "Global distribution of contrail radiative forcing." Geophysical Research Letters no. 26 (13):1853-1856. doi: 10.1029/1999gl900358.

Minnis, P., D. F. Young, D. P. Garber, L. Nguyen, W. L. Smith, and R. Palikonda. 1998. "Transformation of contrails into cirrus during SUCCESS." Geophysical Research Letters no. 25 (8):1157-1160. doi: 10.1029/97gl03314.

Mishchenko, M. I., I. V. Geogdzhayev, L. Liu, J. A. Ogren, A. A. Lacis, W. B. Rossow, J. W. Hovenier, H. Volten, and O. Munoz. 2003. "Aerosol retrievals from AVHRR radiances: effects of particle nonsphericity and absorption and an updated long-term global climatology of aerosol properties." Journal of Quantitative Spectroscopy & Radiative Transfer no. 79:953-972. doi: 10.1016/s0022-4073(02)00331-x.

Mishchenko, M. I., A. A. Lacis, B. E. Carlson, and L. D. Travis. 1995. "Nonsphericity of dust-like tropospheric aerosols: Implications for aerosol remote-sensing and climate modeling." Geophysical Research Letters no. 22 (9):1077-1080. doi: 10.1029/95gl00798.

Mishchenko, M. I., and L. D. Travis. 1998. "Capabilities and limitations of a current FORTRAN implementation of the T-matrix method for randomly oriented, rotationally symmetric scatterers." Journal of Quantitative Spectroscopy & Radiative Transfer no. 60 (3):309-324. doi: 10.1016/s0022-4073(98)00008-9.

Mishchenko, M. I., L. D. Travis, R. A. Kahn, and R. A. West. 1997. "Modeling phase functions for dustlike tropospheric aerosols using a shape mixture of randomly oriented polydisperse spheroids." Journal of Geophysical Research-Atmospheres no. 102 (D14):16831-16847. doi: 10.1029/96jd02110.

Mitchell, D. L. 2002. "Effective diameter in radiation transfer: General definition, applications, and limitations." Journal of the Atmospheric Sciences no. 59 (15):2330-2346. doi: 10.1175/1520-0469(2002)059<2330:edirtg>2.0.co;2.

Mitchell, D. L., A. J. Baran, W. P. Arnott, and C. Schmitt. 2006. "Testing and comparing the modified anomalous diffraction approximation." Journal of the Atmospheric Sciences no. 63 (11):2948-2962. doi: 10.1175/jas3775.1.

Mitchell, D. L., A. Macke, and Y. G. Liu. 1996. "Modeling cirrus clouds .2. Treatment of radiative properties." Journal of the Atmospheric Sciences no. 53 (20):2967-2988. doi: 10.1175/1520-0469(1996)053<2967:mccpit>2.0.co;2.

Munoz, O., H. Volten, J. F. de Haan, W. Vassen, and J. W. Hovenier. 2001. "Experimental determination of scattering matrices of randomly oriented fly ash and clay particles at 442 and 633 nm." Journal of Geophysical Research-Atmospheres no. 106 (D19):22833-22844. doi: 10.1029/2000jd000164.

Myhre, G., and F. Stordal. 2001. "Global sensitivity experiments of the radiative forcing due to mineral aerosols." Journal of Geophysical Research-Atmospheres no. 106 (D16):18193-18204. doi: 10.1029/2000jd900536.

Neale, R. B., C.-C. Chen, A. Gettelman, P. H. Lauritzen, S. Park, et al. 2010. "Description of the NCAR Community Atmosphere Model (CAM 5.0).", NCAR Tech. Note NCAR/TN-486+STR, Natl. Cent. for Atmos. Res., Boulder, Colo. http://www.cesm.ucar.edu/models/cesm1.0/cam/docs/description/cam5_desc.pdf.

Nousiainen, T., M. Kahnert, and B. Veihelmann. 2006. "Light scattering modeling of small feldspar aerosol particles using polyhedral prisms and spheroids." Journal of Quantitative Spectroscopy & Radiative Transfer no. 101 (3):471-487. doi: 10.1016/j.jqsrt.2006.02.038.

Nousiainen, T., and K. Vermeulen. 2003. "Comparison of measured single-scattering matrix of feldspar particles with T-matrix simulations using spheroids." Journal of Quantitative Spectroscopy & Radiative Transfer no. 79:1031-1042. doi: 10.1016/s0022-4073(02)00337-0.

Ono, A. 1969. "Shape and riming properties of ice crystals in natural clouds." Journal of the Atmospheric Sciences no. 26 (1):138-&. doi: 10.1175/1520-0469(1969)026<0138:tsarpo>2.0.co;2.

Penner, J. E., D. H. Lister, D. J. Griggs, D. J. Dokken, and M. McFarland (Eds.) 1999, "Aviation and the Global Atmosphere." Cambridge: Cambridge Univ. Press.

Platt, C. M. R., and Harshvardhan. 1988. "Temperature dependence of cirrus extinction: Implications for climate feedback." Journal of Geophysical Research-Atmospheres no. 93 (D9):11051-11058.

Platt, C. M. R., S. A. Young, P. J. Manson, G. R. Patterson, S. C. Marsden, R. T. Austin, and J. H. Churnside. 1998. "The optical properties of equatorial cirrus from observations in the ARM Pilot Radiation Observation Experiment." Journal of the Atmospheric Sciences no. 55 (11):1977-1996. doi: 10.1175/1520-0469(1998)055<1977:topoec>2.0.co;2.

Ponater, M., S. Marquart, and R. Sausen. 2002. "Contrails in a comprehensive global climate model: Parameterization and radiative forcing results." Journal of Geophysical Research-Atmospheres no. 107 (D13). doi: 10.1029/2001jd000429.

Rap, A., P. M. Forster, J. M. Haywood, A. Jones, and O. Boucher. 2010a. "Estimating the climate impact of linear contrails using the UK Met Office climate model." Geophysical Research Letters no. 37. L20703. doi: 10.1029/2010gl045161.

Rap, A., P. M. Forster, A. Jones, O. Boucher, J. M. Haywood, N. Bellouin, and R. R. De Leon. 2010b. "Parameterization of contrails in the UK Met Office Climate Model." Journal of Geophysical Research-Atmospheres no. 115. D10205. doi: 10.1029/2009jd012443.

Sausen, R., I. Isaksen, V. Grewe, D. Hauglustaine, D. S. Lee, G. Myhre, M. O. Kohler, G. Pitari, U. Schumann, F. Stordal, and C. Zerefos. 2005. "Aviation radiative forcing in 2000: An update on IPCC (1999)." Meteorologische Zeitschrift no. 14 (4):555-561. doi: 10.1127/0941-2948/2005/0049.

Schumann, U. 2012. "A contrail cirrus prediction model." Geoscientific Model Development no. 5(3) : 543-580. doi: 10.5194/gmd-5-543-2012

Schumann, U., B. Mayer, K. Graf, and H. Mannstein. 2012. "A parametric radiative forcing model for contrail cirrus." Journal of Applied Meteorology and Climatology no. 51(7):1391-1406. doi: 10.1175/JAMC-D-11-0242.1

Slingo, A. 1989. "A GCM parameterization for the shortwave radiative properties of water clouds." Journal of the Atmospheric Sciences no. 46 (10):1419-1427. doi: 10.1175/1520-0469(1989)046<1419:agpfts>2.0.co;2.

Slingo, A., T. P. Ackerman, R. P. Allan, E. I. Kassianov, S. A. McFarlane, G. J. Robinson, J. C. Barnard, M. A. Miller, J. E. Harries, J. E. Russell, and S. Dewitte. 2006. "Observations of the impact of a major Saharan dust storm on the atmospheric radiation balance." Geophysical Research Letters no. 33 (24). doi: 10.1029/2006gl027869.

Slingo, A., and J. M. Slingo. 1988. "The response of a general circulation model to cloud longwave radiative forcing: 1. Introduction and initial experiments." Quarterly Journal of the Royal Meteorological Society no. 114 (482):1027-1062. doi: 10.1002/qj.49711448209.

Slingo, J. M., and A. Slingo. 1991. "The response of a general circulation model to cloud longwave radiative forcing: 2. Further studies." Quarterly Journal of the Royal Meteorological Society no. 117 (498):333-364. doi: 10.1002/qj.49711749805.

Sokolik, I. N., D. M. Winker, G. Bergametti, D. A. Gillette, G. Carmichael, Y. J. Kaufman, L. Gomes, L. Schuetz, and J. E. Penner. 2001. "Introduction to special section: Outstanding problems in quantifying the radiative impacts of mineral dust." Journal of Geophysical Research-Atmospheres no. 106 (D16):18015-18027. doi: 10.1029/2000jd900498.

Stamnes, K., S. C. Tsay, W. Wiscombe, and K. Jayaweera. 1988. "Numerically stable algorithm for discrete-ordinate-method radiative transfer in multiple-scattering and emitting layered media." Applied Optics no. 27 (12):2502-2509.

Takano, Y., and K. N. Liou. 1989. "Solar radiative-transfer in cirrus clouds: 1. Single-scattering and optical properties of hexagonal ice crystals." Journal of the Atmospheric Sciences no. 46 (1):3-19. doi: 10.1175/1520-0469(1989)046<0003:srticc>2.0.co;2.

Twomey, S. 1977. "Atmospheric Aerosols." New York: Elsevier.

Travis, D. J., A. M. Carleton, and R. G. Lauritsen. 2002. "Climatology: Contrails reduce daily temperature range - A brief interval when the skies were clear of jets unmasked an effect on climate." Nature no. 418 (6898):601-601. doi: 10.1038/418601a.

Ulanowski, Z., E. Hesse, P. H. Kaye, and A. J. Baran. 2006. "Light scattering by complex ice-analogue crystals." Journal of Quantitative Spectroscopy & Radiative Transfer no. 100 (1-3):382-392. doi: 10.1016/j.jqsrt.2005.11.052.

Ulanowski, Z., E. Hirst, P. H. Kaye, and R. Greenaway. 2012. "Retrieving the size of particles with rough and complex surfaces from two-dimensional scattering patterns." Journal of Quantitative Spectroscopy & Radiative Transfer no. 113 (18):187-194. doi: 10.1016/j.jqsrt.2012.06.019.

Volten, H., O. Munoz, E. Rol, J. F. de Haan, W. Vassen, J. W. Hovenier, K. Muinonen, and T. Nousiainen. 2001. "Scattering matrices of mineral aerosol particles at 441.6 nm and 632.8 nm." Journal of Geophysical Research-Atmospheres no. 106 (D15):17375-17401. doi: 10.1029/2001jd900068.

Warren, S. G., and R. E. Brandt. 2008. "Optical constants of ice from the ultraviolet to the microwave: A revised compilation." Journal of Geophysical Research-Atmospheres no. 113 (D14). D14220. doi: 10.1029/2007jd009744.

West, R. A., L. R. Doose, A. M. Eibl, M. G. Tomasko, and M. I. Mishchenko. 1997. "Laboratory measurements of mineral dust scattering phase function and linear polarization." Journal of Geophysical Research-Atmospheres no. 102 (D14):16871-16881. doi: 10.1029/96jd02584.

Xie, Y., P. Yang, K.-N. Liou, P. Minnis, and D. P. Duda. 2012. "Parameterization of contrail radiative properties for climate studies." Geophysical Research Letters no. 39. doi: 10.1029/2012gl054043.

Yang, H. Y., S. Dobbie, R. Herbert, P. Connolly, M. Gallagher, S. Ghosh, Smrk Al-Jumur, and J. Clayton. 2012. "The effect of observed vertical structure, habits, and size distributions on the solar radiative properties and cloud evolution of cirrus clouds." Quarterly Journal of the Royal Meteorological Society no. 138 (666):1221-1232. doi: 10.1002/qj.973.

Yang, P., B. A. Baum, A. J. Heymsfield, Y. X. Hu, H. L. Huang, S. C. Tsay, and S. Ackerman. 2003. "Single-scattering properties of droxtals." Journal of Quantitative Spectroscopy & Radiative Transfer no. 79:1159-1169. doi: 10.1016/s0022-4073(02)00347-3.

Yang, P., G. W. Kattawar, G. Hong, P. Minnis, and Y. X. Hu. 2008. "Uncertainties associated with the surface texture of ice particles in satellite-based retrieval of cirrus clouds - Part I: Single-scattering properties of ice crystals with surface roughness." Ieee Transactions on Geoscience and Remote Sensing no. 46 (7):1940-1947. doi: 10.1109/tgrs.2008.916471.

Yang, P., and K. N. Liou. 1996. "Geometric-optics-integral-equation method for light scattering by nonspherical ice crystals." Applied Optics no. 35 (33):6568-6584. doi: 10.1364/ao.35.006568.

Yang, P., and K. N. Liou. 1998. "Single-scattering properties of complex ice crystals in terrestrial atmosphere." Contributions to Atmospheric Physics no. 71:223-248.

Yang, P., K. N. Liou, K. Wyser, and D. Mitchell. 2000. "Parameterization of the scattering and absorption properties of individual ice crystals." Journal of Geophysical Research-Atmospheres no. 105 (D4):4699-4718. doi: 10.1029/1999jd900755.

Yang, P., L. Zhang, G. Hong, S. L. Nasiri, B. A. Baum, H. L. Huang, M. D. King, and S. Platnick. 2007. "Differences between collection 4 and 5 MODIS ice cloud optical/microphysical products and their impact on radiative forcing simulations." Ieee Transactions on Geoscience and Remote Sensing no. 45 (9):2886-2899. doi: 10.1109/tgrs.2007.898276.

Yang, P., L. Bi, B. A. Baum, K.-N. Liou, G. W. Kattawar, M. I. Mishchenko, and B. Cole. 2013. "Spectrally consistent scattering, absorption, and polarization properties of atmospheric ice crystals at wavelengths from 0.2 to 100 mu m." Journal of the Atmospheric Sciences no. 70 (1):330-347. doi: 10.1175/jas-d-12-039.1.

Yurkin, M.A., and A.G. Hoekstra. 2009. "User Manual for the Discrete Dipole Approximation Code ADDA v.0.79." http://a-dda.googlecode.com/svn/tags/rel_0_79/doc/manual.pdf.

Zhang, Z. B., P. Yang, G. W. Kattawar, S. C. Tsay, B. A. Baum, Y. X. Hu, A. J. Heymsfield, and J. Reichardt. 2004. "Geometrical-optics solution to light scattering by droxtal ice crystals." Applied Optics no. 43 (12):2490-2499. doi: 10.1364/ao.43.002490.

Zhang, Z., P. Yang, G. Kattawar, J. Riedi, L. C. Labonnote, B. A. Baum, S. Platnick, and H. L. Huang. 2009. "Influence of ice particle model on satellite ice cloud retrieval: lessons learned from MODIS and POLDER cloud product comparison." Atmospheric Chemistry and Physics no. 9 (18):7115-7129.

BRIEF INTRODUCTION OF THE DATABASE OF SINGLE-SCATTERING

PROPERTIES OF MINERAL DUST-LIKE AEROSOLS

The single-scattering database constructed by Meng et al. (2010) uses the tri-axial ellipsoid as the typical shape of dust-like particle, in which two aspect ratios defined as $\varepsilon_{a/c} = a/c$ and $\varepsilon_{b/c} = b/c$, are employed to characterize the shapes, where a, b and c are the semi-minor, semi-major and polar radius ($c \geq b \geq a$). Thus, $\varepsilon_{a/c}$ and $\varepsilon_{b/c}$ will be within the range of 0 and 1, and they form a combination of 42 shapes in this database. The database is organized with respect to the size parameter (x), which is defined as $x = 2\pi c / \lambda$, instead of the wavelength (λ) and the size. And, the size parameters are selected in a logarithmic scale in the range from 0.025 to 1000. The volume-equivalent size parameter is further defined as $x_{eff} = \sqrt[3]{x(\varepsilon_{a/c} \cdot \varepsilon_{b/c})}$. The ranges of the real and imaginary parts of the refractive indices are determined based on the data of Levoni et al. (1997) as $1.10 \leq mr \leq 2.10$ and $0.0005 \leq mi \leq 0.5$ from 0.2 μm to 40 μm. In summary, this database has a total of five independent dimensions, namely the two aspect ratios, the size parameter, and the real and imaginary parts of the complex refractive indices.

The database is created using a combination of four methods to deal with the calculation of the single-scattering properties of ellipsoids with various shapes (aspect ratios) and size parameters from Rayleigh to the geometric optics, because no single method can cope with the entire size parameter range. The four scattering methods are

the DDA (Discrete Dipole Approximation) method (Yurkin and Hoekstra 2009), the T-matrix method (Mishchenko and Travis 1998), the Lorenz-Mie theory (Bohren and Hoffman 1983), and the IGOM (Improved Geometric Optics) method (Bi et al. 2009; Yang and Liou 1996). Generally, the DDA method is used for the ellipsoidal case with aspect ratio and size parameter that is relatively small ($x_{eff} < 17$), while the T-matrix and the Lorenz-Mie theory are used for spheroids ($x_{eff} < 30$) and spheres (all size parameters), respectively. The other cases are calculated through IGOM.

Once provided with the necessary inputs, such as refractive indices, aspect ratios, and size parameters, the database can supply the single-scattering properties, including the phase matrix, extinction efficiency, single-scattering albedo and asymmetry factor, etc. The bulk optical properties can be derived if additional information about the size and shape distribution is known. This database is well suited for various applications in aerosol remote sensing and light scattering problems, and it is publicly available upon request. For further details about the database, its comparison and validation with measurements, and more references, please refer to the paper by Meng et al. (2010).

APPENDIX B

REPRESENTATION OF ICE PARTICLE SURFACE ROUGHNESS

The single-scattering database constructed by Meng et al. (2010) uses the tri-axial ellipsoid as the typical shape of dust-like particle

The ice particle surface roughness is considered in the Improved Geometric Optics Method (IGOM, Yang and Liou 1998) used for the calculation of the ice optical property database (Yang et al. 2013). The surface slope of ice particles is represented by a normal distribution following Cox and Munk (1954) who studied the optical effect of sea surface roughness:

$$P(Z_x, Z_y) = \frac{1}{\sigma^2 \pi} \exp\left[-\frac{Z_x^2 + Z_y^2}{\sigma^2}\right], \tag{B1}$$

where Z_x and Z_y are the slope variations at the particle surface in the x and y directions. By randomly distorting the particle surface slope, the degree of roughness is controlled by the σ parameter. In this study, we select three values of σ with the value of 0.5 denoting the severely roughened particle case, 0.03 denoting the moderately roughened particle case, and 0 for the completely smooth case. Ice particle surface roughness effect is not included for particle size parameters smaller than about 20 where the single-scattering properties are calculated by the discrete dipole approximation method. More discussion about particle surface roughness can be found in Yang et al. (1998; 2008).